Charge Transport Phenomena in Cryogenic SiGe Heterojunction Bipolar Transistors

Thesis by
Nachiket R. Naik

In Partial Fulfillment of the Requirements for the
Degree of
Doctor of Philosophy

CALIFORNIA INSTITUTE OF TECHNOLOGY
Pasadena, California

2024
Defended August 22, 2023

Nachiket R. Naik
ORCID: 0000-0001-8271-643X

ACKNOWLEDGEMENTS

This work was supported by NSF Award Number 1911926 and by JPL PDRDF Project Number 107978.

I would like to begin by thanking my PhD advisor, Prof. Austin Minnich, not only for the consistent support towards my work and development as a researcher, but also for his mentorship. The decision to pivot the group's research focus was a bold one, and while it was difficult to sustain at times, I thank Austin for maintaining the courage to persist and for showing us that it can be done. Of course, it also helps to be surrounded by some of the most gifted researchers I've had the privilege to work with and learn from. Drs. Jacob Kooi, Kieran Cleary, Sander Weinreb, Anthony Ardizzi, and everyone else from the CRAL team; I'm grateful for all the little (sometimes massive) nuggets of wisdom you were kind enough to impart during my PhD work.

I would also like to thank my thesis committee – Profs. Melany Hunt, Stevan Nadj-Perge, and Kieran Cleary. Your diverse fields of expertise have enriched this dissertation and your feedback has been invaluable. I'd also like to thank the MCE administrative staff; I'm grateful to you all for making it easy for us to focus on work and for creating a relaxed and supportive environment in our department.

To the Minnich group, past and present – what a ride it has been! Thank you all for being dependable labmates and making the ride that much easier to navigate as a group. I'm thankful for all your feedback and ideas on my work and presentations, and of course for the endless basement-office discussions on various topics of the world. A special mention to Beka, Tomi, Hirsh, and Adrian for being friends who knew when to provide words of encouragement, but more importantly for keenly identifying days when it wasn't worth staying in lab past 4.30pm!

Outside of my research environment, I owe a big thank you to the members and friends in the Caltech Cricket Club for being a much needed weekly respite from work. A PhD can be quite isolating at times, but being part of this cricket team provided the perfect antidote of collective goal-seeking and the opportunity to contribute something larger than myself. The camaraderie and passion for the sport that we've been able to develop in these past 5-6

years is remarkable, and I wish nothing but the best for this group. A special shoutout to Jag, Akshay, Subhojit, Siddharth, Sumit, and many others whom I consider friends and mentors; some of the best memories of grad school will be the practice sessions, dinner discussions and strategy talks that we would so enthusiastically engage in... I tell myself the outcome will follow some day!

To my extended family and friends in Hyderabad – Pratham, Vidushi, Siddharth kaka & Keya kaki, and all my honorary chachas and chachis; thank you for grounding me and being such a large net of support and positivity. Every time I've been back home, you have provided a welcome reminder to enjoy life beyond work and I've left feeling energized knowing you all have my best wishes at heart. Thank you for being my tribe.

To the Poodipeddi and Naik clans; I am fortunate enough to have a family that is scattered around various parts of the globe, but who have still managed to maintain a close bond with me and with each other. Thank you all for investing so much into our family and treating me as your own son. I'm especially grateful to Suri mama and Rekha attha for continually being champions of my education and career here in the US, and of course for being the best crash-pad a nephew could ask for. I'm also grateful to now have the privilege of calling the Bheri and Marrey clans family; thank you all for your kindness and support, and for welcoming me into your life.

To my friends at Caltech – Cai, Irene, Jag, Gunho, Widi, Lena, Anushri, and everyone else; thank you Cai, for the almost too frequent coffee-and-other-drinks breaks you always were available for, and for being the fun-loving soul that you are. Irene, it's been amazing being around you and a privilege to see you open up and have our friendship grow in the process. Jag, it's been a treat working on cricket club stuff with you, but also to see your journey in the process. I couldn't have asked for better brothers-in-arms than Gunho and Widi to survive the MCE rigor alongside; thank you both for being willing participants in our post-study food explorations. Special mention to Widi for being such a great friend and enabler of good times. Anushri, thank you for being one of the few constants during an ever-changing grad school life, and really just for being around; it's the little things like the regular coffee chats and Thai food takeouts that kept days sane. And finally, to my roommates at 689, thank you Widi, Lena and Anushri, for making this place feel as close to home as it gets.

Finally, to the inner sanctum - Amma, Papa and Sruti. I cannot do justice to the thanks I owe you, but a few specific things come to mind. Sruti, I'm truly grateful to have you as my partner, both in my PhD and in life. You have inspired me to persevere and be just a little bit better each day, and this thesis could not have been done without your support. Amma and Papa, thank you both for your unending belief in me. At times when I didn't know whether things were going my way, you provided the perspective to show me when they were, and the confidence to fight back when they weren't. Lastly, to my grandfather - thank you for being the champion of the entire family's education for being the giant upon whose shoulders we stand.

ABSTRACT

Silicon-germanium heterojunction bipolar transistors (HBTs) are widely used for high-speed communications and radar systems owing to the their low-cost and competitive performance relative to III-V compound semiconductor devices. Due to the higher cost and lower yield of III-V high electron mobility transistors (HEMTs) based on InGaAs quantum wells, SiGe HBTs operating at cryogenic temperatures are of significant interest for radio astronomy and quantum computing. However, their microwave noise performance has long been observed to be poorer than those of HEMTs. As a result, the physical mechanisms governing the cryogenic DC, microwave and noise performance of SiGe HBTS have been a topic of investigation for many years. Improved understanding of these mechanisms may ultimately allow for the realization of HBTs with noise performance rivaling those of HEMTs yet with lower cost, improved compatibility and integration with CMOS processes, and high yield.

This thesis uses theoretical and experimental methods to examine cryogenic charge transport phenomena in SiGe HBTs which affect the microwave noise performance. A particular focus is on the anomalous electrical characteristics at cryogenic temperatures, in which pronounced deviations from the ideal drift-diffusion theory are observed. Various explanations for the observed anomalous cryogenic I-V behavior have been postulated, such as quasi-ballistic transport and electron tunneling, among others. Despite a number of works on this topic over the past three decades, none of the explanations has been unambiguously confirmed or excluded.

The first contribution from this thesis is a study of the quasiballistic transport hypothesis using an exact, semi-analytic solution of the Boltzmann equation. Several prior studies have claimed quasiballistic electron transport across the base as the origin of cryogenic non-ideal current-voltage characteristics. Specifically, the observation of temperature independent DC performance below ~ 80 K has been attributed partly to quasiballistic transport resulting in a presumed increase in electron temperature, but this hypothesis has been examined only using empirical models which leave ambiguity. We overcome this limitation by adapting an exact, semi-analytic solution to the Boltzmann equation based on an asymptotic expansion approach to describe electron transport across the base region of an HBT. With this exact solution, we computed

macroscopic electrical properties such as collector current and transconductance which could be directly compared with experiments. We find that the computed transport characteristics are inconsistent with experiment, with the calculated transconductance following the ideal drift-diffusion inverse temperature dependence. This finding implies that quasiballistic electron transport is unlikely to be the origin of cryogenic non-ideal I-V characteristics.

Next, we study a previously unexplored explanation, the presence of lateral spatial inhomogeneities in the base-emitter junction potential height, as the origin for the observed non-ideal cryogenic current-voltage anomalies in SiGe HBTs. While this phenomenon has been established as the origin for similar cryogenic I-V anomalies observed in Schottky diodes, this possibility has not yet been considered for SiGe HBTs. We experimentally investigate this hypothesis by characterizing the base-emitter built-in potential and its temperature dependence using both capacitance-voltage and current-voltage characteristics. We observe a marked discrepancy in the built-in potential obtained using these two methods at cryogenic temperatures, a signature consistent with the presence of lateral inhomogeneities in the junction potential. We hypothesize that these inhomogeneities arise from clustering of Ge as a result of aggressive doping of modern devices, and propose future directions that allow direct probing of these inhomogeneities.

Finally, we explore the potential improvements in the minimum achievable noise temperature of HBT amplifiers by considering the effects of shot-noise correlation. We first model the expected reduction in cryogenic noise temperature of a state-of-the-art transistor as a result of shot-noise correlation. We then quantify the accuracy of the present noise measurement techniques that allow us to exploit the benefits of shot-noise correlation, and propose modifications to the noise measurement setup that will permit an unambiguous experimental determination of the magnitude of the effect.

PUBLISHED CONTENT AND CONTRIBUTIONS

[1] Nachiket R. Naik et al. "Investigation of Cryogenic Current-Voltage Anomalies in SiGe HBTs: Role of Base-Emitter Junction Inhomogeneities". In: *arXiv preprint arXiv:2302.14210* (2023). DOI: arXiv:2302.14210.

Contributions: N.R.N designed and assembled the modifications to the experimental setup, wrote the Python scripts for data acquisition, analyzed and fit the resulting data, and wrote the mansuscript.

[2] Nachiket R. Naik and Austin J. Minnich. "Quasiballistic Electron Transport in Cryogenic SiGe HBTs Studied Using an Exact, Semi-analytic Solution to the Boltzmann Equation". In: *Journal of Applied Physics* 130.17 (2021), p. 174504. DOI: 10.1063/5.0063178.

Contributions: N.R.N adapted and developed an asymptotic solution for the relevant problem, implemented the calculations in Python, generated the results for observables from the developed solution, and wrote the manuscript.

TABLE OF CONTENTS

LIST OF ILLUSTRATIONS

LIST OF TABLES

Number *Page*

Chapter 1

INTRODUCTION

This chapter was adapted in part from:

[1] Nachiket R. Naik and Austin J. Minnich. "Quasiballistic Electron Transport in Cryogenic SiGe HBTs Studied Using an Exact, Semi-analytic Solution to the Boltzmann Equation". In: *Journal of Applied Physics* 130.17 (2021), p. 174504. DOI: 10.1063/5.0063178.

[2] Nachiket R. Naik et al. "Investigation of Cryogenic Current-Voltage Anomalies in SiGe HBTs: Role of Base-Emitter Junction Inhomogeneities". In: *arXiv preprint arXiv:2302.14210* (2023). DOI: arXiv:2302.14210.

Silicon-germanium (SiGe) heterojunction bipolar transistors (HBTs) are a type of bipolar transistor that are ubiquitous in microwave applications such as radar technology, wireless communications and analog circuits [1]. This widespread usage is largely due to their practical advantages such as high yield, low cost, and ease of integration into multi-component chips through the established BiCMOS process relative to alternatives like III-V technology devices. Besides these practical and economical advantages, SiGe HBTs offer competitive performance in radio frequency (RF) applications due to low phase noise and high cutoff frequencies, making them the preferred choice across a wide range of frequency bands. However, one of the more exciting benefits of this technology occurs when these devices are cooled to cryogenic temperatures. Right from their earliest development stages, SiGe HBTs have been studied for their cryogenic DC, RF and noise performance capabilities. The predicted and subsequently realized improvements in gain, transconductance, cutoff frequency and minimum noise figure with decreasing temperature, have made SiGe HBTs contenders for use as low-noise amplifiers, particularly in applications such as radio astronomy and quantum computing. [2–5]

However, the improvements in cryogenic performance of SiGe HBTs have long been observed to saturate at operating temperatures below $\sim$ 100 K, deviating abruptly from the predictions of the drift-diffusion framework used to describe charge transport in bipolar transistors. This anomalous cryogenic

behavior has limited the performance of SiGe HBTs, and therefore the underlying physical mechanisms have been the topic of some investigation. [2, 6–8] Various hypotheses concerning the origin of this anomalous cryogenic behavior have been put forth in the literature; however, discrepancies associated with some of these hypotheses have not been analytically tested, and other plausible origins for anomalous cryogenic behavior have not been studied in SiGe HBTs. This thesis aims to analytically and experimentally study the origins of cryogenic non-ideal DC behavior using Boltzmann transport theory and electronic measurements that probe the Si:SiGe junction from room to cryogenic temperatures. Our work advances efforts to improve the cryogenic electrical characteristics and hence microwave noise performance of SiGe HBTs.

1.1 Cryogenic low-noise amplification

Signal receiving and amplification systems in the millimeter-wave regime are integral components that drive a wide range of scientific and commercial endeavors - radio astronomy,[5, 9] radar communications, [8, 10, 11] deep space communication, [12–14] and quantum computing readout circuitry [3, 4, 7] among many others. The backbone many such receiving systems for weak signals is a low-noise amplifier (LNA). In fields such as radio astronomy, the signal amplification stage is cryogenically cooled due to the stringent noise requirements on the LNA. Signal detection in radio astronomy must contend with cosmic microwave background radiation, on the order of 2.7 K, plus additional noise contributions from Earth's atmosphere.[14] Therefore, the receiver systems must have an overall system noise temperature of this order, leading to an even more enhanced noise requirement for the low-noise amplifiers that make up these systems. In quantum computing applications, the strength of qubit readout signals is on the order of -135 dBm, i.e. $\sim$ 13 orders of magnitude smaller than 1 mW, thus requiring a quantum limited first stage amplifier followed by a second-stage LNA with $\sim$ 1 K noise temperature. [15] While direct cooling of the LNAs significantly subdues the thermal noise component of the amplifiers and enhances their electronic performance, transistor amplifiers still remain a factor of $\sim 5 - 10$ or more above the quantum noise limit. [16, 17]

Among transistor amplifiers, there are two primary types of transistors that are contenders for cryogenic low-noise amplifiers - the silicon-germanium (SiGe) heterojunction bipolar transistor (HBT), and the high electron-mobility tran-

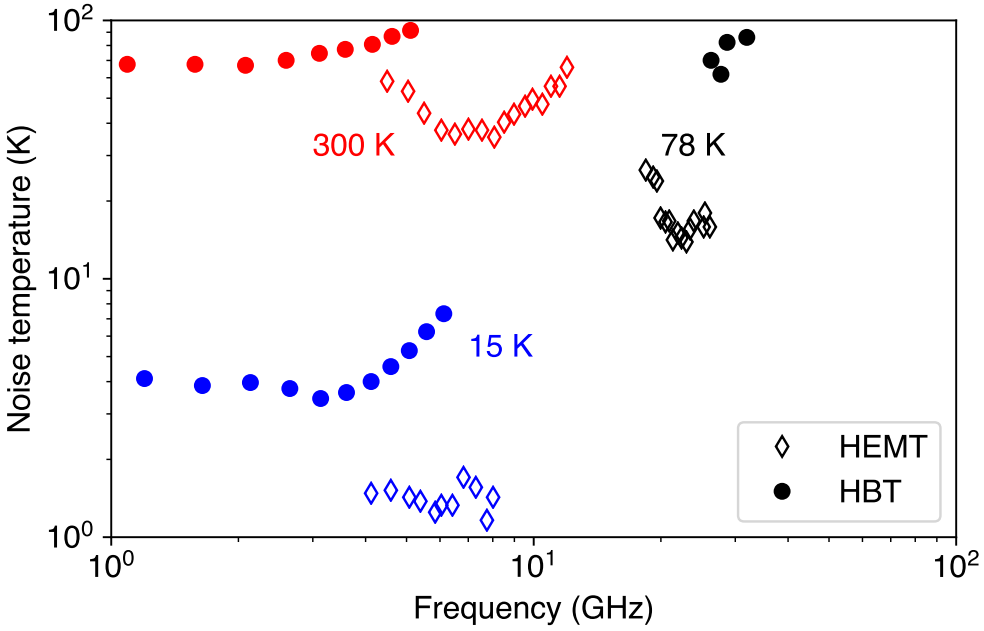

Figure 1.1: Effective noise temperature data versus frequency for InP HEMTs and SiGe HBTs from room to cryogenic temperatures. Data obtained from [3] and references within. Across all temperatures and frequencies ranges, HEMTs demonstrate noise temperatures that are 3× or more better than HBTs. Image credit: Iretomiwa Esho.

sistor (HEMT), usually fabricated on III-V compound semiconductors such as InP. Both of these technologies have their respective advantages in practice; however, strictly from a noise temperature standpoint, InP HEMT LNAs still outperform SiGe HBTs up to the tens of GHz frequency range. [3, 18] Figure 1.1 plots various noise temperatures for SiGe HBTs and InP HEMTs with data from Ref. [3] and associated references. We see that the noise performance of the HEMTs is consistently better than those of HBTs across the 1 – 20 GHz range and between 15 – 300 K by a factor of 3 or more. For this reason, HEMTs are currently the prevailing transistor of choice for second-stage cryogenic LNAs in quantum computing, and first-stage cooled LNAs in conjunction with mixers and receivers in radio astronomy applications. [16]

While HEMTs are currently the superior transistor for noise performance, recent advancements in SiGe HBTs have made them strong contenders for cryogenic LNAs. Cryogenic SiGe HBTs have demonstrated linear DC gain values of 80,000 ($\sim$ 50 dB) and cutoff frequencies close to 800 GHz. [2, 11] Further, optimized SiGe HBT architectures have been developed with noise tempera-

tures 3 K in the 4 – 8 GHz bandwidth, with power consumption on the order of hundreds of microwatts. [18] This ability of SiGe HBTs to provide competitive RF and noise performance with reduced power consumption provides a significant advantage over HEMT devices, which typically consume a few milliwatts of power. [3, 19] The cooling power available at the cryogenic stages of many of these application systems is on the order of a few watts, making the power consumption of LNAs a key parameter for scaling these systems. [15] SiGe HBTs also hold another type of practical advantage over III-V HEMTs, in that they are easier to fabricate, provide higher yield, integrate well with other Si BiCMOS process technologies, and are ultimately less expensive. [1, 20] With these advantages, developing a low-noise amplifier using SiGe HBT technology will contribute to advances in low-noise microwave systems such as radio telescopes and quantum computers. [15, 21]

1.2 Background: An overview of developments in SiGe HBT technology

We begin this by describing qualitatively the timeline and evolution of bipolar junction devices, followed by a quantitative understanding of the operating principles of SiGe HBTs.The first bipolar junction transistor (BJT) was developed between 1947–49 by Shockley and colleagues [22, 23] who described the theory and principles of a simple p-n-p junction device. This kicked off a flurry of research towards developing and modeling the physics of p-n junction transistors. [24] Following this development, the 1950s – 1960s involved rapid efforts to improve the performance of bipolar transistors, as well as developing accurate models to predict their DC, microwave and noise performance. [24–26] However, by the 1970s it was believed that the silicon bipolar field had matured and become commercially relevant. [27] The bulk of the research studies in the mid-1970s focused on advancing the performance of state-of-the-art BJTs by optimizing the fabrication and doping techniques. [27–29] By this, the limitations of further scaling Si BJT technology were identified. [30–32]

In 1957, Kroemer had first proposed the theory to develop a transistor with a heterogeneous junction using a SiGe alloy that would allow customized bandgap tuning through Ge content to enhance device gain beyond Si BJT levels. [33] The proposed heterojunction bipolar transistor (HBT) would circumvent the material limitations that governed Si BJT performance, primarily the tradeoff between base resistance and DC current gain. Kroemer also de-

scribed the physics that would allow for enhanced performance of these SiGe HBTs when cooled to cryogenic temperatures.

However, the ability to grow device-quality SiGe hererojunctions with minimal defects was not achieved until the advent of molecular beam epitaxy (MBE) in the mid-1980s, when Patton et al. developed the first SiGe base transistor, [34] and later by the demonstration of SiGe HBTs grown using ultra-high vacuum chemical vapor deposition (UHV/CVD). [35] Right from these early realizations of SiGe HBTs, their performance at cryogenic temperatures has been of interest. Patton et al. observed a marked increase in collector current, as predicted by the theory laid out by Kroemer, near liquid nitrogen temperatures. [34, 35] This enhancement in performance led to renewed excitement surrounding the development of SiGe HBTs.

In the early 1990s, pioneering work led by Cressler and colleagues demonstrated a slew of transistors optimized for cryogenic performance. [36–38] The doping profiles of these devices were primarily optimized to improve their switching speeds, [39] but key DC and RF performance metrics such as gain, transconductance and cutoff frequency were shown to improve from 300 K to $\sim$ 80 K. [40] At the same time, analytical models based on drift-diffusion theory for electronic transport in SiGe HBTs were being tested against simulations and experimental observations [41–44]. The predictions of drift-diffusion promised further improvements in DC and RF performance at temperatures approaching liquid helium temperatures (4 K). However, significant deviations from drift-diffusion theory in measured DC quantities were observed when operating these devices at 4 K. Specifically, an increased collector current relative to drift-diffusion predictions, along with anomalous temperature independent current-voltage curves below 80 K were observed. [6, 45] This anomalous, non-ideal excess collector current resulted in a saturation of related performance metrics such as DC gain and transconductance, which still persist in modern HBT technology. [2]

In years following the observations of these cryogenic anomalies, the bulk of the efforts in SiGe HBTs focused on modeling and optimizing their RF and noise performance. Majority of the research efforts were focused on optimizing the architectures and profiles of these devices to improve high-speed performance metrics such as cutoff frequency and maximum operating frequency. [37, 39, 46, 47] Developments in fabrication processes, such as reducing key

feature sizes and resistances, have therefore also been directed towards the same goal. [11, 48–50] Once the potential for SiGe HBTs to be used as a cryogenic low-noise amplifier (LNA) was realized by Weinreb and colleagues, some efforts have focused on understanding and improving the lower limits of their noise performance [5, 13, 51, 52]. These works enabled the development and verification of small-signal and noise models across a wide range of temperatures and biases that has aided device engineers in building SiGe HBTs based cryo-LNAs. More recently, with the advent of quantum computing and a thrust to develop low-noise hardware to enable practical realizations of quantum computers, the interest in SiGe HBT amplifiers has re-emerged. The reason for this interest is largely due to the development of cryo-LNAs developed by Bardin and colleagues that demonstrated competitive noise and RF performance with power consumption on the order of a few hundred microwatts. [3, 18] The low power requirement is especially important to enable scaling quantum computers to thousands of qubits, since the thermal budget to cool these devices is limited.

The steady improvements in these macroscopic performance metrics through years of optimization and engineering has undoubtedly led to HBTs becoming strong contenders in cryogenic applications like quantum computing and radio astronomy; however, the questions surrounding the physical mechanisms responsible for the non-ideal cryogenic behavior remained unanswered. In this work, we look at the cryogenic performance of SiGe HBTs from the perspective of device physicists, to motive future device iterations that push the envelope of their fundamental performance limits.

1.3 The drift-diffusion theory of electronic transport in SiGe HBTs

This section aims to provide a primer on the theoretical concepts surrounding charge transport in SiGe HBTs relevant to understanding the topics in the rest of thesis. A more detailed account of the models and physics surrounding SiGe HBT device physics is available in Refs. [1, 12, 53]. Here, we provide a more concise overview of the prevailing drift-diffusion theory that analytically models and predicts electronic behavior in these devices.

Overview of bipolar device operation

Here, we provide an overview of bipolar transistor architecture and operating principles, starting from a qualitative description and later detailing the

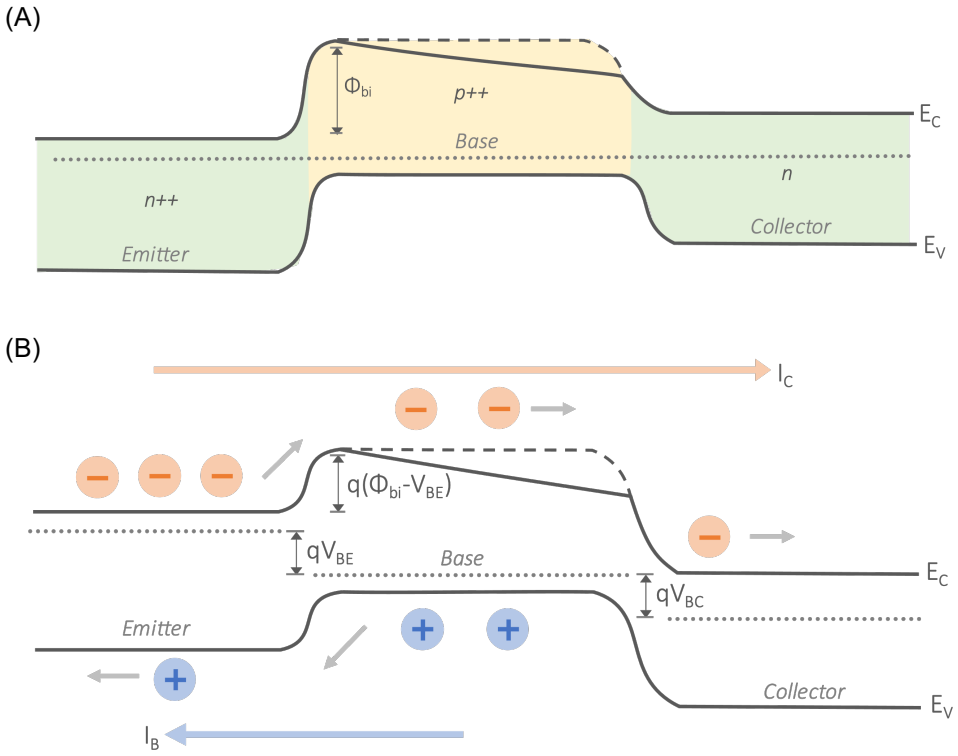

Figure 1.2: Schematic band diagrams of a typical SiGe HBT device. (A) At equilibrium, with no bias provided, the Fermi level (dotted line) is flat across the emitter, base and collector regions. The dashed line denotes a base structure for a Si BJT with no Ge content, whereas the solid line indicates a SiGe base with Ge grading. The potential barrier Φ_{bi} is a result of carrier depletion in the space-charge region (SCR). (B) Under forward active regime (FAR), two terminal currents I_C and I_B are generated. I_C results from thermally-activated electron emission from emitter to base, with the barrier Φ_{bi} reduced by the application of V_{BE}. These electrons diffuse across the narrow base and drift across the reverse-bias V_{BC} into the collector, i.e. drift-diffusive transport. I_B is a hole current from thermally-activated holes overcoming the reduced barrier from base to emitter.

quantitative advantages of SiGe HBTs over Si BJTs as a result of Ge-induced bandgap modifications. An understanding of the physics of semiconductor devices must begin with an energy band diagram. Fig. 1.2 provides a schematic of the nominal valence and conduction band structure across the different spatial regions of a typical bipolar transistor. The representative structures for Si bipolar junction transistors (BJTs) as well as SiGe heterjunction bipolar transistors (HBTs). The typical band diagram of a Si bipolar junction transistor (BJT) is also depicted to facilitate a comparison of two technologies. In this thesis, we will consider the n-p-n variant of bipolar transistors as they are more common.

A bipolar transistor can be simply viewed as two p-n junctions placed back-to-back against each other, creating either a p-n-p type transistor, or an n-p-n type transistor. These n- and p-doped regions can be engineered to have distinct charge carrier concentrations through the introduction of dopants that either raise or lower the electrons available for conduction. The concentration of electrons (negative charge carriers) in an n-type region is usually assumed to be the same as the donor concentration, N_D; likewise, the concentration of holes (positive charge carriers) in a p-type semiconductor is equal to the acceptor concentration N_A. When these differently doped n- and p- semiconductor regions are fused to create the n-p-n strucuture, the valence E_V and conduction E_C band energies of each region are restructured (also referred to as band-bending) to maintain a continuous, flat Fermi level E_F at equilibrium, resulting in energy bands as shown in Fig. 1.2. The resulting three distinct regions are referred to as the emitter, base and collector.

A typical BJT has three terminal currents: the emitter current I_E, base current I_B and collector current I_C, related to each other as $I_E = I_C + I_B$. When operated in common-emitter mode, meaning that the emitter terminal is held at ground voltage while bias is provided to the base and collector, two terminal currents I_C and I_B remain. The directions of these current flows are shown in Fig. 1.2. The biases provided to these terminals can be appropriately selected such that the collector current I_C is greater than the base current I_B by a few orders of magnitude, resulting in a DC current gain $\beta = I_C/I_B$. In a Si BJT, the doping concentrations are the primary variable used to control the terminal currents, and consequently the gain and other performance metrics. By doping the emitter much higher than the base, the electrons constituting

the collector current are higher in concentration relative to holes constituting the base current for a given base-emitter bias, resulting in a current gain. This doping scheme usually involves a heavily doped n++ region as the emitter, an intermediately doped p+ region as the base, and a moderately doped n or n- region as the collector, which facilitates charge transport from emitter to collector over that from base to emitter while limiting base resistance. The inherent tradeoff within this doping scheme is that by reducing the base doping relative to the emitter, the resistance of the base region is increased, which results in a degradation of noise performance. The ideal solution requires a technique to increase gain without resorting to tuning the relative doping concentrations of the emitter and base. More details on the tradeoffs and optimization of doping concentrations for Si BJTs can be found in Refs. [12, 53].

A heterojunction bipolar transistor (HBT) is simply a modified BJT with the base-emitter junction made up two different materials. The key difference between the Si BJT and a SiGe HBT is the presence of Ge in the base region, resulting in two Si:SiGe heterojunctions. The use of a $Si_{1-\chi}Ge_{\chi}$ alloy in the p-doped base region provides a new variable, the Ge content ratio χ, to control the terminal currents in the HBT, thus creating another avenue for tailoring device characteristics to suit various applications. Specifically, inclusion of Ge in the Si base reduces the bandgap of the resulting alloyed semiconductor due to the difference in bandgaps of Silicon (1.12 eV) and Germanium (0.66 eV), which can be continuously varied as function of Ge concentration. The SiGe alloy base region will consequently have a bandgap $E_{G,SiGe}(\chi)$ lower than that of the Si emitter. The reduction in bandgap $\Delta E_{G,Ge}$ due to the presence of Ge fraction χ in a strained SiGe film at room temperature is given by the following approximation [12]:

$$\Delta E_{G,Ge} \approx 0.96\chi - 0.43\chi^2 \tag{1.1}$$

The key advantage of this reduction in bandgap lies in the fact that the shift in valence and conduction band energies is not equal. The majority of the offset occurs in the valence band, raising its energy in the base region relative to pure-Si and therefore creating a larger barrier for hole transport in the base current. This can equivalently be viewed as a shift down in the conduction band energy,

creating a reduced energy barrier for the electron flow constituting the collector current, the relation of which can be tuned using χ. [1]

The discontinuous valence and conduction band offset has a profound effect on currents through relation between the bandgap and the intrinsic carrier concentration. The intrinsic carrier concentration n_i in the valence and conduction bands of a semiconductor depends exponentially on the the bandgap as shown below [53]

$$n_{i,SiGe}^2(T) = N_C N_V e^{-E_{G,SiGe}/kT} = N_C N_V e^{-(E_{G,Si} - \Delta E_{G,Ge}(\chi))/kT} = n_{i,Si}^2 e^{\Delta E_{G,Ge}(\chi)} \tag{1.2}$$

where, N_C and N_V are the conduction and valence band effective density-of-states, respectively, $E_{G,Si}$ is the bandgap energy of Si and T is the physical temperature. As bipolar transistors are minority carrier devices, this intrinsic carrier concentration directly affects the concentration of injected charge carriers across the emitter-base region. Therefore, the Ge content provides a parameter to tune the charge carrier concentration on either end of the Si:SiGe heterojunction. [1, 53]

An added advantage of using a SiGe alloy in the base is the ability to tailor the profile of the energy band in the bulk of the region. By grading the Ge profile along the base, a quasi-electrical field can be created for the electrons as evidenced by the sloped conduction band in Fig. 1.2. This allows the electrons from the emitter to be accelerated to the collector terminal. In this way, engineering the spatial profile of the Ge concentration to alter the bandgap of the base SiGe alloy can be used to develop bipolar transistors where the gain is no longer limited by the ratio of emitter and base doping levels, opening up the door for high-performance SiGe HBTs. Next, we will quantitatively build up the equations that describe Si BJT perform and modify them based on the discussion above for a SiGe HBT.

Drift-diffusion theory for collector and base currents

As mentioned in the earlier, there are two terminal currents, I_C and I_B, in the common-emitter mode of operation. The formulation for these currents can be developed by considering the equations for the same currents in a Si BJT, and then accounting for the modifications due to the presence of Ge in

the base. The equations for these currents are provided for device operation in the forward-active regime (FAR) that provides a large DC gain β, where the base-emitter voltage V_{BE} provides a forward bias, and the base-collector V_{BC} provides a reverse bias.

The collector current in a simple Si BJT operated in FAR is given by [12, 53]:

$$I_C(T) = qA_E \frac{D_{e,B}}{W_B} \frac{n_i^2}{N_{A,B}} \exp \frac{qV_{BE}}{kT} = qA_E \frac{D_{e,B}}{W_B} N_{D,E} \exp \frac{-q(\Phi_{bi} - V_{BE})}{kT} \quad (1.3)$$

where, q is the charge of an electron, A_E is the emitter area, $D_{e,B}$ is the electron diffusivity in the base, W_B is the width of the of the bulk base region, $N_{A,B}$ is the acceptor concentration in the base, $N_{D,E}$ is the donor concentration in the emitter, V_{BE} is the applied base-emitter voltage, Φ_{bi} is the built-in potential barrier of the base-emitter junction and T is the physical temperature. The second part of Eq. 1.3 shows the version of the relation that assumes that the carrier distribution across the emitter and base regions follow a Maxwell-Boltzmann distribution in energy, giving the following relationship between the built-in potential across the junction and the carrier concentrations:

$$\frac{n_i^2}{N_{A,B}} = N_{D,E} \exp \frac{-q\Phi_{bi}}{kT} \quad (1.4)$$

Recall, that the carrier concentrations are assumed to be equal to the doping concentrations of each region, an assumption that is valid as long as the dopants are completely ionized. [53] I_C is also commonly reported as the collector current density $J_C = I_C/A_E$ normalized to the emitter area A_E.

Equation 1.3 can be broken down to understand the basic principles of collector current in a bipolar transistor. The main mechanism of collector current is through the thermally activated injection of electrons from the emitter into the base across the barrier potential $\Phi_{bi} - V_{BE}$, where they are the minority carrier. The concentration of electrons from the emitter that possess the thermal energy can be written as $N_D e^{-q(\Phi_{bi} - V_{BE})/kT}$, helped by the reduction in barrier potential due to the applied forward bias V_{BE}. Simultaneously, the base-collector junction is reverse-biased through V_{BC}, resulting in a negligible concentration of electrons at the collector edge of the base (n=0). This results in a sharp electron concentration gradient along the base that creates a diffusive flux of electrons from the base edge to the collector edge. This diffusive

flux scales as the diffusivity of electrons the bulk base material, $D_{e,B}$, and upto first order the gradient of electrons along the base $\frac{\partial n(x)}{\partial x}$ can be written as:

$$\frac{\partial n(x)}{\partial x} = \frac{N_D e^{-q(\Phi_{bi}-V_{BE})/kT} - 0}{W_B} \tag{1.5}$$

where $n(x)$ is the spatially dependent electron concentration. If the base width W_B is narrow and on the order of the electron diffusion length, recombination currents in the base can be neglected, and the electrons diffusing across the base are drawn into the collector region through drift due to the built-in electric field, making up a collector current. This theory of electron transport for bipolar devices is known as the drift-diffusion theory.

A similar logical sequence is followed to arrive at the equation for the base current I_B [12, 53]:

$$I_B \approx qA_E \frac{D_{h,E}}{L_E} N_{A,B} exp \frac{-q(\Phi_{bi} - V_{BE})}{kT} \tag{1.6}$$

where $D_{h,E}$ is the hole diffusivity and L_E is the hole diffusion length in the emitter material. More details on the derivation of these currents can be found in Refs. [12, 53].

Since the primary purpose of a Si:SiGe heterojunction in HBTs is to enable further increases in I_C relative to I_B, we will now focus on the modifications to the collector current due to the presence of Ge in the base. As mentioned earlier, the use of a SiGe alloy results in a selectively reduced barrier potential for electrons to overcome while being injected from the emitter to the base. This bandgap reduction due to Ge content results in a change in intrinsic carrier concentration captured by Eq. 1.2. To account for the presence of Ge, we simply substitute the value of $n_i^2(T)$ from Eq. 1.2 that accounts for the bandgap reduction due to Ge, $\Delta E_{G,Ge}(\chi)$ into Eq. 1.3, giving us the modified collector current as

$$\begin{aligned} I_{C,Ge}(T) &= qA_E \frac{D_{e,B}}{W_B} \frac{n_{i,Si}^2}{N_{A,B}} exp \frac{\Delta E_{G,Ge}(\chi)}{kT} exp \frac{qV_{BE}}{kT} \\ &= qA_E \frac{D_{e,B}}{W_B} N_{D,E} exp \frac{\Delta E_{G,Ge}(\chi)}{kT} exp \frac{-q(\Phi_{bi} - V_{BE})}{kT} \end{aligned} \tag{1.7}$$

where the effects on the collector current due to Ge grading have been neglected for simplicity. It is clear from Eq. 1.7 above that small changes in bandgap due to Ge, and therefore the barrier potential, will result in large increases in collector current due to exponential term. More importantly, due to the exponential dependence on temperature in the Boltzmann distribution, the collector current is expected to increase sharply as temperature decreases, leading to an exponential increase in DC gain

$$\beta_{SiGe} = \frac{I_{C,Ge}(T)}{I_B(T)} = \beta_{Si} exp \frac{\Delta E_{G,Ge}(\chi)}{kT} \tag{1.8}$$

Moving forward, we drop the subscripts denoting the difference between Si BJTs and SiGe HBTs and any device related quantities are specified for SiGe HBTs. Another impotant device characteristic besides gain is the incremental change in collector current I_C as a result of change in the base-emitter voltage V_{BE}. This quantity known as the transconductance $g_m(T)$ is given by:

$$g_m(T) \equiv \frac{\partial I_C(T)}{\partial V_{BE}} = \frac{qI_C(T)}{kT} \tag{1.9}$$

where we have substituted Eq. 1.7 for the numerator. Due the logarithmic dependence of I_C with V_{BE} the transconductance g_m can be viewed as the slope of the log-linear I_C vs. V_{BE} plot, also know as a Gummel plot. The transconductance is an important quantity in the small-signal model of an HBT as it captures the voltage sensitivity of the device, and it directly affects the noise performance of the device. [5] From Eq. 1.9 above, in the ideal case the slope of the Gummel curves is expected to get steeper with decreasing temperatures due to the T^{-1} dependence of g_m. However, when SiGe HBTs are operated below $\sim$ 100 K physical temperature, the transconductance has been observed to be consistently deviate from the expected T^{-1} trend. This non-ideal temperature dependence is commonly captured using an empirical fitting parameter known as the collector current ideality factor, $n(T)$, defined as

$$n(T) \equiv \frac{g_{m,ideal}(T)}{g_{m,measured}(T)} = \frac{qI_c(T)}{g_{m,meas}(T)kT} \tag{1.10}$$

where the measured transconductance at cryogenic temperatures is lower than the predicted value, resulting in $n(T) > 1$. The same ideality factor is used to

capture the observed non-ideal excess collector current at cryogenic temperature as

$$I_C(T) = I_{C,0} \exp\left(\frac{qV_{BE}}{n(T)kT}\right) \tag{1.11}$$

where $I_{C,0}$ is the collector saturation current that lumps all terms independent of V_{BE}.

1.4 Prior explanations for cryogenic non-idealities

As mentioned earlier in this chapter, non-ideal current-voltage behavior has long been observed in SiGe HBTs operated at cryogenic temperatures. Specifically, the slope of the I-V curves, g_m starts to become temperature independent below around 100 K, and the absolute value of collector currents is observed to be higher than the predictions of drift-diffusion theory. Many theories have been proposed to explain the origin of this non-ideal collector current-voltage behavior, starting from the 1990s. Early proposed theories included trap-assisted tunneling current, [45] and non-equilibrium electron temperatures greater than that of the lattice caused by heating due to quasiballistic transport. [6] Later, work done by Bardin et al. at Caltech captured the same non-ideal cryogenic behavior and also attributed it to elevated electron temperatures originating from quasiballistic transport, and incorporated a model for this phenomenon into the noise model for cryogenic SiGe HBTs. This empirical model described the elevated effective electron temperature, T_{eff}, as a function of physical lattice temperature, T_{phys} and the ideality factor $n(T)$ as defined in Eq. 1.11, as shown below. [12]

$$T_{eff} \equiv n(T_{phys})T_{phys} \tag{1.12}$$

This effective electron temperature is often used in place of the physical temperature governing the electron concentration at the base-emitter junction [2, 6, 8], and therefore governing the collector current and DC observables. It is important to note here though that this effective electron temperature is not analytically derived from quasiballistic transport.

More recently, another physical mechanism proposed to explain anomalous cryogenic collector current behavior was direct tunneling of electrons through the base-emitter junction barrier in SiGe HBTs with base widths on the order

of 10 nm. [4] It was shown that simulations of tunneling current density model that depends on barrier potential and base-width agree relatively well with experimentally observed I-V curves for devices with base-widths on the order of tens of nanometers. However, tunneling is only expected to be the dominant current mechanism at low to moderate carrier injection levels, away from bias values close to the built-in potential. A recent paper by Ying et al. attempts to reconcile the different transport theories by proposing a transition in electron transport mechanisms as a function of base-emitter bias V_{BE}. [8] It is hypothesized that at voltages well below the base-emitter potential barrier Φ_{bi}, as V_{BE} is increased from 0, trap-assisted tunneling dominates electron transport at first, and as V_{BE} approaches few 100 mV from the barrier potential, electron transport switches to direct tunneling. Finally, at voltages comparable or greater to the Φ_{bi}, it is claimed that quasiballistic transport dominates electron transport, and that all of these distinct mechanisms combined result in an excess collector current and ideality factor greater than 1. Figure 1.3 from Ref. [8] is displayed below to provide a schematic representation of the bias-dependence of these phenomena.

While this bias-dependent picture of transitions between non-ideal electron transport mechanisms may be phenomenologically true, various discrepancies exist in the different theories. For example, the theory that quasiballistic transport in narrow-base SiGe HBTs results in heating of carriers does not present evidence directly linking the temperature increase to the effects of quasiballistic transport. Further, while electrons may be heated as they traverse the base by the built-in field, the collector current and transconductance are governed by the electronic temperature and concentration prior to the base-emitter junction as is evidenced from Eq. 1.11, and should not be affected by the transport mechanism of the electrons once they are injected into the base. While a simulation of electron transport using Monte Carlo methods has been cited as evidence for quasiballistic transport in cryogenic SiGe HBTs, the justification relies on observations of elevated minority carrier velocity in the neutral base. [6, 54] However, the transport mechanism for minority carriers in the base region is in fact through a diffusion gradient, and a reduced carrier velocity would imply a shallower gradient of carriers driving this diffusion flux.

Similarly, while direct tunneling may explain excess cryogenic collector current at low to moderate injection levels, it is unlikely to be the origin of non-ideal

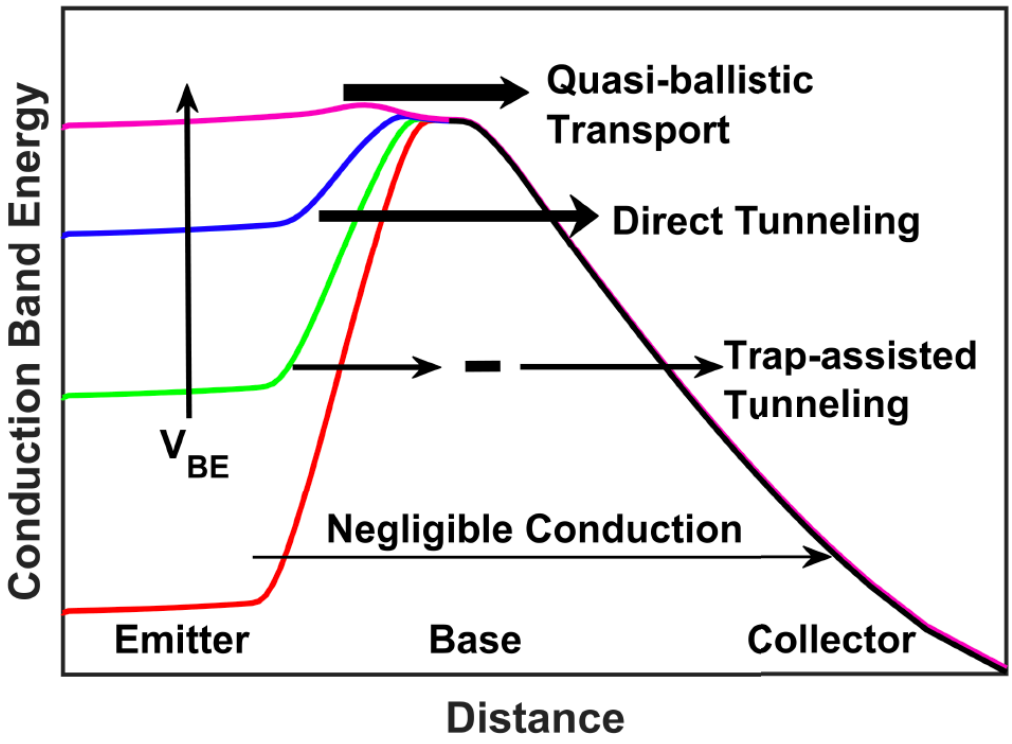

Figure 1.3: Schematic representation of the transition between different electron transport mechanisms in cryogenic SiGe HBTs, taken from [8]. This picture aims to explain the origin of the non-ideal cryogenic I-V characteristics in SiGe HBTs by combining three different bias dependent transport theories: trap-assisted well at biases well below the barrier, direct tunneling at low-to-moderate biases, and quasiballistic transport at biases close to the built-in potential.

currents at biases comparable to the built-in potential where quasiballistic transport dominates. [4] Further, the tunneling current probability decreases exponentially with increase in base width, making it more likely to be the dominant in narrow base devices. However, non-ideal collector currents have been reported in first generation devices with base widths on the order of 100 nm,[8] for which direct tunneling is unlikely.

Finally, and most importantly, an analytical study of quasiballistic transport using the Boltzmann equation and its effect on macroscopic electronic observables in cryogenic SiGe HBTs has not yet been used to confirm whether it is the origin of the non-ideal I-V behavior. Parallels to the steady particle transport problem in a narrow semiconductor region exist in various fields such as rareified gas dynamics, [55] phonon transport, [56–58] and neutron

transport. [59] Among these approaches, simulation based method run into issue due to the computational inefficiency associated with denser scattering matrices which must be discretized in both real-space and reciprocal lattice space. [60–62] On the other hand, exact, analytical solutions to the BTE are limited to approximations that do not make the use of energy-dependent relaxation times. [63] However, advances in Boltzmann transport theory such as semi-analytical asymptotic solutions [55, 57, 64] may provide an efficient and robust solution if adapted to electronic transport problems.

While the origin of cryogenic anomalies in SiGe HBTs remains inconclusive, it is interesting to note that similar cryogenic anomalies have been observed in Schottky diodes in the 1980s-90s, and have been explained by spatial inhomogeneities in the potential barrier. The slopes of the I-V characteristics of Schottky diodes were observed to become temperature independent below ~ 100 K, and various temperature dependent ideality factors $n(T)$ were reported. [65–67] It was shown that a distribution of spatial inhomogeneities spaced on the order of a few nanometers is able to predict temperature-dependent ideality factor $n(T)$ behavior closely resembling that seen in SiGe HBTs [68]. This was later confirmed through direct probing of the Schottky junction through capacitance-voltage (C-V) techniques [69], as well as direct spectroscopy methods such as ballistic electron emission spectroscopy [69, 70]. Specifically, the depletion capacitance of these Schottky diodes provides information on the mean barrier potential, while comparison with the current-voltage characteristics provides sensitivity to non-uniform regions of the barrier. Fundamentally, the depletion regions, and therefore the potential barriers, of both Schottky diodes and the base-emitter n++ - p+ junction of Si:SiGe HBTs result from the same electrostatic behavior of charge carriers. However, the possibility of spatial inhomogeneities at the base-emitter barrier in SiGe HBTs has not been explored so far.

1.5 Outline of thesis

In this thesis, we aim to understand the physical origins for the anomalous cryogenic current-voltage behavior in SiGe HBTs using analytical and experimental techniques.

In Chapter 2, we study the effects of quasiballistic transport in cryogenic SiGe HBTs using a semi-analytical, asymptotic solution to the Boltzmann transport equation. This method is adapted from studies of phonon transport that use efficient exact solutions to the Boltzmann equation with energy dependent relaxation times. We expand this method to compute the energy-dependent spatial electronic distribution under an applied bias in a narrow SiGe HBT base without linearizing the distribution. We then calculate observables such as collector current and transconductance, and by showing that they contradict experimental trends versus temperature, we demonstrate that quasiballistic transport is likely not the origin of the observed cryogenic anomalies. We conclude this chapter by hypothesizing spatial inhomogeneities in the base-emitter junction potential as a possible origin for the observed anomalies.

In Chapter 3, we experimentally study the possible presence of inhomogeneous barrier potential at the base-emitter junction in modern SiGe HBTs. We do this by comparing barrier potential extractions using two distinct electronic methods; current-voltage (I-V) characteristics and capacitance-voltage (C-V) characteristics. In prior literature, large discrepancies in the temperature-dependence of I-V and C-V extracted barrier potentials were shown to be a signature of non-uniform barrier potentials in Schottky diodes. We demonstrate a similar discrepancy in the barrier potential at temperatures below 100 K, strongly supporting the presence of an inhomogeneous base-emitter junction potential. Finally, we hypothesize phenomena associated with aggressive doping of modern HBTs as the likely cause for barrier inhomogeneities and suggest techniques to further verify their presence.

In Chapter 4, we delve into understanding a mechanism, shot noise correlation, that may allow for a reduction in the cryogenic noise performance of SiGe HBTs. We first briefly introduce the theory of noise modeling in SiGe HBTs and then focus on cryogenic modeling the shot noise correlation phenomenon using this theory. We then describe the methods used to measure the effects of this phenomenon in state-of-the-art discrete devices. Finally, we characterize the uncertainty of the primary source of error in our measurement and pro-

pose future modifications to the measurement approach which will permit the accurate characterization of shot noise correlation.

Finally, in Chapter 5, we summarize the key results of our work and highlight areas of potential future interest related to this field.

Chapter 2

QUASIBALLISTIC TRANSPORT IN CRYOGENIC SIGE HBTS

This chapter was adapted in part from:

[1] Nachiket R. Naik and Austin J. Minnich. "Quasiballistic Electron Transport in Cryogenic SiGe HBTs Studied Using an Exact, Semi-analytic Solution to the Boltzmann Equation". In: *Journal of Applied Physics* 130.17 (2021), p. 174504. DOI: 10.1063/5.0063178.

In the previous chapter, we introduced the anomalous cryogenic behavior of SiGe HBT devices and highlighted how this behavior has long been attributed to mechanisms such as quasiballistic transport through empirical models of electron temperature. However, this conclusion has not been rigorously tested against theoretical predictions of quasiballistic transport. The goal of this chapter is to develop a semi-analytical solution to the Boltzmann transport equation and solve it for quasiballistic electron transport in the base. We then test the predictions of this exact solution against measurements from the literature on similar devices and demonstrate that the computed transport characteristics are inconsistent with experiments, implying that quasiballistic transport is unlikely to be the origin of cryogenic non-ideal IV characteristics. Finally, we propose what we believe is the likely mechanism for non-ideal IV behavior in cryogeic SiGe HBTs.

2.1 Background: electron transport in the base region of SiGe HBTs

Following the first reports of SiGe HBTs grown by molecular beam epitaxy [71, 72], studies of the cryogenic performance of HBTs were performed in the early 1990s [71, 73]. Subsequent work focused on understanding and optimizing base doping and Ge grading profiles for cryogenic performance [37]. While these works demonstrated the enhanced collector current and transconductance expected at cryogenic temperatures, later studies reported marked deviations from the DC current-voltage characteristics predicted from drift-diffusion theory [6, 45]. Specifically, it was observed that below ~ 77 K the collector (I_C) and base current (I_B) exceeded the predicted values at a given temperature

and bias and were independent of temperature, with the transconductance g_m saturating instead of increasing as T^{-1}. These non-ideal IV characteristics limit the gain, cutoff frequency, and ultimately the microwave noise figure.

The origin of this behavior has been attributed to several mechanisms, including trap-assisted tunneling at base-emitter voltage (V_{BE}) well below the built-in potential; [45] and non-equilibrium carrier transport, in which electrons quasiballistically traverse the base, at biases comparable to the built-in potential [6]. The latter effect has been phenomenologically described using an elevated electron temperature that is taken as the effective temperature for thermionic emission at the base-emitter junction [2, 6, 12]. As base widths were scaled further down to ~ 20 nm in recent years, direct tunneling of electrons was reported to contribute to the collector current at biases approaching the built-in potential [4, 7, 8].

However, as alluded to in the previous chapter, there are several discrepancies with these explanations. First, non-ideal collector currents have been reported in first generation devices with base widths on the order of 100 nm [8], for which direct tunneling is unlikely. Further, at base doping levels above $\sim 3 \times 10^{18}$ cm^{-3} common in modern devices, [4, 8] ionized impurity scattering is expected to dominate, which is relatively insensitive to temperature. Therefore, quasiballistic transport is not expected to be markedly more pronounced at cryogenic temperatures relative to room temperature as evidenced by the weak temperature dependence of the minority carrier mobility [12, 74–76]. Finally, while electrons may be heated as they traverse the base by the built-in field, the collector current and transconductance depend on the electron temperature at the base-emitter junction prior to transport across the base and thus cannot be affected by the built-in field in the base.

A quantitative, non-empirical description of the quasiballistic transport process would allow a more thorough test of whether quasiballistic transport is a possible origin of the cryogenic DC non-idealities. Steady-state particle transport across a slab of thickness comparable to the MFPs of the particles is described by the Boltzmann equation [56, 77]. This slab problem has been extensively investigated for radiative [56, 78, 79], neutron [59], phonon [56, 57], and electron transport [60, 61, 63, 80] as well as for rarefied gases [81–83]. Although analytical solutions under the 'one-speed' or 'gray' approximations are possible, [63, 79] solutions considering energy-dependent relaxation times are

less tractable analytically. Alternative numerical approaches are computationally expensive owing to the need to discretize both the spatial and reciprocal space coordinates [60, 62, 63]. Several works have reported asymptotic series expansion methods, based on the original theory by Grad [55], for rarefied gas dynamics [84] and phonon transport [64]. These methods could enable the efficient solution of the present problem of electronic transport in a narrow base, but they have yet to be adapted for electronic transport.

Here, we report a study of quasiballistic electron transport across a narrow base using an exact, semi-analytic asymptotic expansion approach to solve the Boltzmann equation.

2.2 Theory: Boltzmann equation solution for quasiballistic transport

We begin by describing the semi-analytical asymptotic approach used to solve the one-dimensional Boltzmann equation describing electron transport across the base. Focusing on the DC characteristics, we assume steady transport across a base of width L with prescribed forward and reverse going electron distribution functions at the left and right boundaries, respectively. Then, the Boltzmann equation for the electronic distribution function $f_\lambda(x)$ is given by:

$$\frac{\partial f_\lambda}{\partial \overline{x}} = \frac{L}{v_{x\lambda}} \sum_{\lambda'} C_{\lambda\lambda'} f_{\lambda'} = \sum_{\lambda'} M_{\lambda\lambda'} f_{\lambda'} \tag{2.1}$$

where $C_{\lambda\lambda'}$ is the collision matrix, $v_{x\lambda}$ is the group velocity for electronic state λ, $M_{\lambda\lambda'}$ is a dimensionless matrix defined as above, x is the spatial coordinate, $\overline{x} \equiv x/L$, and f_λ is the desired distribution function normalized so that $V^{-1}\sum_\lambda f_\lambda(x) = n(x)$, where V is a normalizing volume. Macroscopic quantities like electric current are computed using the appropriate Brillouin zone sum [56].

In this work, we will solve this equation using an exact, semi-analytic asymptotic expansion method originally reported for rarefied gases [84] and recently adapted for phonons [64]. The theory for phonons is given in detail in Ref. [64] for an isotropic crystal under the relaxation time approximation. Here, we generalize this theory to incorporate the full electron collision matrix and arbitrary crystals and extend its applicability beyond linear deviations from a reference distribution.

In the asymptotic expansion approach, f_λ and associated observables are written as series expansions with the average Knudsen number $\epsilon \equiv \langle\Lambda\rangle / L$ as the expansion parameter, where the average mean free path $\langle\Lambda\rangle \equiv \sum_{\lambda_k} v_{x\lambda}\tau_\lambda f_\lambda^{eq}/n_{eq}$. Here f_λ^{eq} and n_{eq} are the reference equilibrium distribution function and electron density at zero base-emitter voltage, and τ_λ is the wave vector dependent relaxation time. As an example, f_λ is written as:

$$f_\lambda \quad = \quad \sum_l \epsilon^l f_{\lambda,l} \tag{2.2}$$

where $f_{\lambda,l}$ is the distribution function for order l. Substituting this expansion into Eq. 2.1, we get

$$\sum_l \epsilon^l \frac{\partial f_{\lambda,l}}{\partial x} = \sum_l \epsilon^l \sum_{\lambda'} M_{\lambda\lambda'} f_{\lambda',l} \tag{2.3}$$

Since $M_{\lambda\lambda'}$ scales with ϵ^{-1}, the left and right side of Eq. 2.3 are offset by one order of ϵ. Equating terms of the lowest order $l = 0$ we find that the zeroth-order solution satisfies

$$\sum_{\lambda'} M_{\lambda\lambda'} f_{\lambda',0}(x) = 0 = g_0(x) \sum_{\lambda'} M_{\lambda\lambda'} e_{0,\lambda'} \tag{2.4}$$

where we have split the solution into a pure $x-$dependent term $g_0(x)$ and wave vector dependent term $e_{0,\lambda}$, i.e. $f_{\lambda,0}(x) = e_{0,\lambda} g_0(x)$. We note here that the null eigenvector $e_{0,\lambda}$ can be any Boltzmann distribution function, but for this work we choose $e_{0,\lambda} = f_\lambda^{eq}$ corresponding to the Boltzmann distribution for the case where no bias is applied.

We now consider the first-order terms. From Eq. 2.3, the solution can be written using the zeroth-order solution:

$$f_{\lambda,1}(x) = \sum_{\lambda'} \epsilon^{-1} M^{-1}_{\lambda\lambda'} \left(\frac{\partial f_{\lambda',0}}{\partial \overline{x}} \right) + g_1(x) e_{0,\lambda} \tag{2.5}$$

This solution is also determined only up to an x-dependent multiple of the null eigenvector, denoted $g_1(x)$, which will be obtained after deriving the governing equation for x-dependence. The higher-order solutions proceed similarly.

The x-dependence of the zeroth-order solution can be derived by enforcing current continuity for the electric current density J_x in the x-direction for a 1D steady slab:

$$\frac{\partial J_x}{\partial \overline{x}} = 0 = V^{-1} \frac{\partial}{\partial \overline{x}} \sum_{\lambda} q v_{x\lambda} \sum_{l} \epsilon^l f_{\lambda,l} \tag{2.6}$$

which must be satisfied at each order of the expansion. Substituting from Eq. 2.5 for the first-order term, we find that

$$\sum_{\lambda'} v_{x\lambda} \epsilon \frac{\partial}{\partial \overline{x}} \left(\epsilon^{-1} M^{-1}_{\lambda\lambda'} \frac{\partial f_{\lambda',0}}{\partial \overline{x}} + g_1(x) e_{0,\lambda} \right) = 0 \tag{2.7}$$

The second term in the parentheses vanishes since $v_{x\lambda}$ is odd in λ whereas $e_{0,\lambda}$ is even. Therefore, we find

$$\frac{\partial^2 f_{\lambda,0}(x)}{\partial \overline{x}^2} = 0 \tag{2.8}$$

Applying $V^{-1} \sum_\lambda f_{\lambda,0}(x) = n_0(x)$ to the above equation, we see that the zeroth-order electron density $n_0(x)$ satisfies the diffusion equation. Similarly, it can be shown that higher-order terms of $f_{\lambda,l}(x)$ also satisfy the diffusion equation (see Appendix A of Ref. [64]).

To solve these equations, the boundary conditions at each order must be specified. The boundary conditions at zeroth order are simply the prescribed isotropic, hemispherical electron distribution functions at the edges of the slab specified by n_L and n_R. Note that in general, the actual carrier density at the edges of the slab will differ from these values owing to quasiballistic transport. Thus, the solution at zeroth order is just the diffusion equation solution. Note that the boundary conditions of the original problem are completely satisfied at zeroth order.

We now discuss the boundary conditions at higher orders. Because the zeroth order solution completely satisfies the boundary conditions of the original problem, to enforce the boundary conditions at higher orders we must introduce a boundary correction term $\Phi_\lambda(x)$ that satisfies the Boltzmann equation in the boundary region. This boundary correction must exactly cancel the contribution from $f_\lambda(x)$ at the boundaries and vanish in the bulk.

The Boltzmann equation for the boundary solution at first-order is:

$$\frac{\partial \Phi_{\lambda,1}(\eta)}{\partial \eta} = \sum_{\lambda'} \epsilon M_{\lambda\lambda'} \Phi_{\lambda',1}(\eta) \tag{2.9}$$

where we introduce the stretched boundary-region coordinate $\eta \equiv x/\epsilon$. Focusing on the left boundary at $\overline{x} = 0$, the condition enforced on this first-order boundary term is that it must cancel the first-order bulk term: $\Phi_{\lambda,1}|_0 = -f_{\lambda,1}|_0$. Using Eq. 2.5, the condition for the left boundary is:

$$\Phi_{\lambda,1}|_0 = -c_1 e_{0,\lambda} \left.\frac{\partial g_0}{\partial x}\right|_0 - \sum_{\lambda} \epsilon^{-1} M^{-1}_{\lambda\lambda'} \left.\frac{\partial g_0}{\partial x}\right|_0 e_{0,\lambda'} \tag{2.10}$$

where, as in Ref. [64], we anticipate the boundary term to scale as the gradient of the previous order solution:

$$g_1|_{x=0} = -c_1 \left.\frac{\partial g_0}{\partial \overline{x}}\right|_{x=0} \tag{2.11}$$

An analogous boundary condition applies to the right boundary. The unknown constant c_1 captures the jump-type boundary condition for non-diffusive corrections at first order. Solving for c_1 involves obtaining the eigenvalues and eigenvectors of M and is described in detail in Ref. [64]. In brief, the general solution to Eq. 2.9 can be written as a linear combination of the eigenvectors corresponding to the negative eigenvalues of M:

$$\Phi_{\lambda,1} = \sum_i A_i h_{\lambda,i} e^{\rho_i \eta} \tag{2.12}$$

where A_i are unknown coefficients, and ρ_i and $h_{\lambda,i}$ are the negative eigenvalues and the corresponding eigenvectors, respectively. Only the negative eigenvalues are used so that the boundary solution tends to zero in the bulk. Then, Eq. 2.10 gives a linear system of equations for A_i and c_1. We note that in the formulation in Ref. [64], c_1 represents a deviation in a linearized quantity, such as temperature, relative to an equilibrium value. However, in the present formulation, c_1 multiplies the absolute distribution function rather than a deviation and is not restricted to linear deviations from that distribution.

After calculating c_1, the first-order solution is completely specified using the diffusion equation for $g_1(x)$ and the boundary condition from Eq. 2.11. The analysis progresses similarly for higher-order solutions. For the specific slab problem here, it can be shown that the jump coefficients associated with second-order derivatives vanish as in Appendix C of Ref. [64]. Therefore, c_1 is the only required coefficient, allowing the asymptotic expansion to be summed

over all higher-order terms. After summing f_λ over the Brillouin zone to obtain the carrier density, we obtain:

$$n(x) = n_0 + (n_R - n_L)(1-2\overline{x}) \sum_{n=1}^{\infty} \epsilon^n (-2)^{n-1} c_1^n = n_0 + \frac{\epsilon c_1}{1+2\epsilon c_1}(n_R - n_L)(1-2\overline{x}) \tag{2.13}$$

where $n_0(x)$ is the zeroth-order carrier density, and the higher-order terms correct for non-diffusive transport. Because the macroscopic constitutive relation between electric current density and number density gradient applies in the bulk, [64] the current density including the effect of quasiballistic transport is given by:

$$J_{e,x} = -qD_{e,Si}\frac{\partial n(x)}{\partial x} \tag{2.14}$$

Here, $D_{e,Si}$ is the bulk diffusivity. These results have been extensively validated by comparison to Monte Carlo simulations in Ref. [64]. We also observe from Eq. 2.13 that the dependence of carrier density and thus electric current on base-emitter voltage V_{BE} is only through the left boundary condition $n_L \sim e^{qV_{BE}/kT}$, allowing the current-voltage characteristics for arbitrary V_{BE} to be obtained once c_1 is computed.

We briefly discuss the features of the present asymptotic approach compared to those reported previously for electronic transport. An early study of the slab electron transport problem employed a direct scattering matrix solution to the Boltzmann equation [60] that required discretization in wave vector and spatial coordinates and was thus numerically expensive. Approximate methods such as the McKelvey flux method [61, 85] and the Landauer approach [58, 62] were next applied for electron and phonon transport. These flux-based methods provide approximate solutions to the Boltzmann equation with minimal computational expense due to simplifications to the collision term. The advantage of the present approach is that it provides the exact solution to the Boltzmann equation with the full collision matrix while requiring only discretization in wave vector space rather than in both real space and wave vector space. The resulting calculation is thus orders of magnitude faster than the purely numerical solution of the Boltzmann equation. Further, compared to Ref. [64] this work does not require linearization around an equilibrium distribution and can accommodate arbitrary crystals, rather than isotropic ones;

and the full collision matrix, rather than the relaxation time approximation. Finally, with a standard numerical treatment, the current density would need to be recomputed when any variable is changed. With the present method, the expensive calculation for c_1 only needs to be performed once at each temperature because the average Knudsen number and V_{BE} are independent of c_1 and included directly in Eq. 2.13.

2.3 Results: Calculation of collector current in a SiGe base

We apply this approach to study 1D steady-state electron transport in slabs of non-degenerate silicon ($N_A = 3 \times 10^{-18}$ cm^{-3}) and of width $L \sim 40$ nm - 100 μm. The hemispherical distribution function at the left and right boundaries is a Boltzmann distribution with carrier density $n_L = n_{L,eq} \exp(qV_{BE}/kT)$ and $n_R = 0$, respectively, where $n_{L,eq}$ is the equilibrium minority carrier concentration. Note that at high biases the law of the junction used for n_L may not be strictly satisfied due to degenerate carrier statistics, but this approximation will not affect our conclusions as discussed later. The junction is assumed to be a step junction with a uniform Ge fraction of 0.2, with bandgap values for SiGe obtained from Ref. [86]. Owing to lack of precise knowledge of the electronic structure and scattering mechanisms in the strained SiGe:C films used in devices, in this work we assume parabolic bands and employ the relaxation time approximation, with energy-dependent impurity and acoustic phonon scattering rates based on the forms given in Chapter 3 of Ref. [77]. Several works report that the temperature dependence of minority carrier mobility in p-doped SiGe does not obey the $\sim T^{1.5}$ scaling typical of impurity scattering at cryogenic temperatures [74–76]. Therefore, we extract coefficients and exponents for relaxation time $\tau = \mu_0 T^p E^s$ by fitting the computed mobility to minority carrier mobility data reported in Fig. 3 of Ref. [76] and combining the relaxation times for acoustic and impurity scattering using Matthiessen's rule. The fitting coefficients and exponents for acoustic (impurity) scattering rates are $\mu_0 = 350$ (700) cm^{2}V^{-1}s^{-1}, $p = -1.5$ (0.25) and $s = -0.5$ (-0.5), respectively. Our conclusions are robust to these assumptions. We solve for c_1 at the temperatures corresponding to Ref. [4], assuming an isotropic crystal using a 2200×2200 grid in energy and angular coordinate space. The collision matrix used in this work corresponds to Eq. B.5 of Ref. [64]. For example, at 300 K we find $c_1 = 0.7341$.

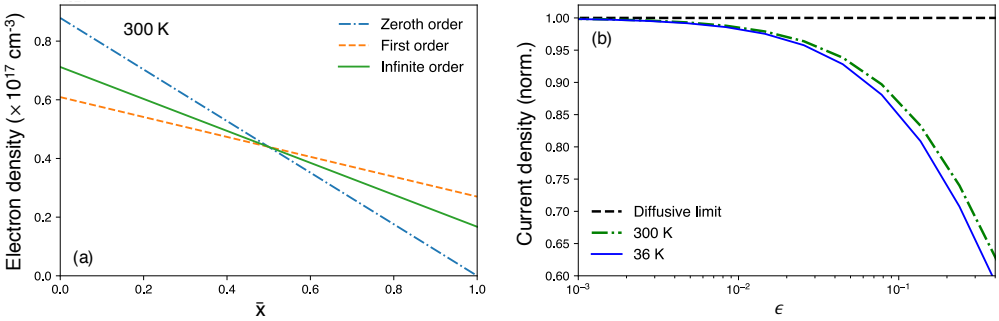

Figure 2.1: (a) Electron density $n(x)$ versus normalized distance $\overline{x}$ at 300 K and $V_{BE} = 0.8$ V at zeroth order (blue dash-dotted line), first order (orange dashed line) and infinite order (green solid line). (b) Normalized electric current density versus Knudsen number ϵ at 300 K (green dash-dotted line) and 36 K (blue solid line) derived from carrier concentration gradient. The current density is normalized to the diffusion current density obtained at zeroth order (dashed line). Quasiballistic transport predicts a comparable decrease in current relative to drift-diffusion at both room and cryogenic temperatures as Knudsen number increases.

Figure 2.1a shows the carrier density versus normalized distance at 300 K for $L = 40$ nm and $V_{BE} = 0.8$ V calculated at different orders of the expansion. The zeroth-order solution is by definition the drift-diffusion solution and exhibits a linear profile with a carrier density at the left edge of the slab of $n_L = n_{L,eq} \exp(qV_{BE}/kT) = 0.87 \times 10^{17}$ cm^{-3}. The higher-order non-diffusive corrections predict a reduced carrier concentration gradient across the base relative to the zeroth-order case. This feature occurs because at $\epsilon = 0.38$, transport is quasiballistic, with electron mean free paths being on the order of the base width. Under these conditions, the ballistic propagation of some electrons across the base lowers the carrier density at the left boundary and increases it at the right boundary, resulting in jump-type boundary conditions at each edge and a shallower carrier density across the base. The solution at the first-order over-corrects for non-diffusive effects, but the infinite series accounts for higher-order terms and lies in between the zeroth and first-order solutions. This non-monotonicity occurs because the closed form solution switches signs at each order in Eq. 2.13.

To study how the electric current density is impacted by quasiballistic transport, we calculate the current density versus Knudsen number in Fig. 2.1b for two temperatures values reported in Ref. [4]. The electric current density

from Eq. 2.14 is proportional to the carrier concentration gradient in Fig. 2.1a for a given voltage, temperature and Knudsen number. At 300 K, the current density is observed to decrease from the diffusive limit as $\epsilon \to 1$ (quasiballistic limit). As seen from Fig. 2.1a, quasiballistic corrections lower the concentration gradient, and the contribution of the correction terms is multiplied by Knudsen number, resulting in greater deviation with increasing Knudsen number. Therefore, a shallower concentration gradient and consequently a decreased current density is expected with increasing Knudsen number. At 36 K corresponding to the temperature reported in Ref. [4], the calculation for c_1 is repeated to give a value of 0.733. At this temperature, we see that the deviation from the diffusive limit is comparable to that at 300 K. The difference between the two curves is due to changes in bulk diffusivity at 36 K that are independent of c_1 and predict a slightly smaller current density than at 300 K. This calculation shows that even at cryogenic temperatures, quasiballistic effects yield a lower collector current density relative to the drift-diffusion prediction, opposite to that observed experimentally.

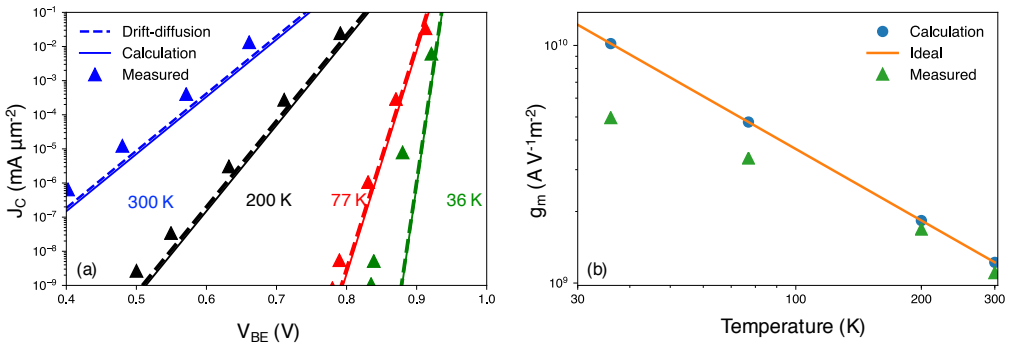

Figure 2.2: (a) Collector current density J_c versus base-emitter voltage V_{BE} from drift-diffusion (dashed line) and quasiballistic calculations (solid line) compared to measured data (triangles, Ref. [4]) at various temperatures. (b) Transconductance per unit area g_m versus temperature for an ideal diode (dashed line), from calculation (circles), and experiment (triangles, Ref. [4]) for a fixed J_C derived from the $J - V$ characteristics in (a). The present calculations do not predict the increased current density or decreased transconductance observed in measurements at cryogenic temperatures.

We now compare the predictions of our calculation with experimentally reported DC IV characteristics. The data from Ref. [4] is selected due to the availability of Gummel curves for a state-of-the-art device at a reasonably dense concentration of temperatures. Figure 2.2a plots calculated and mea-

sured collector current density versus base-emitter voltage V_{BE}. We observe that at all temperatures, quasiballistic transport predicts a weakly reduced current density compared to the drift-diffusion prediction, as expected from the discussion of Fig. 2.1b. The calculation nearly coincide in Fig. 2.2a because the deviation of quasiballistic current density from the diffusive current density is small on the logarithmic scale in Fig. 2.2a. At 300 K, 200 K, and 77 K, both predictions agree well with measured data. However, at 36 K, quasiballistic and drift-diffusion current density predictions are similar in magnitude but are both orders of magnitude lower than the measured data for a given V_{BE}. Further, the predicted slope of the $J - V$ curve is unchanged from the drift-diffusion prediction and does not saturate to a value similar to that at 77 K as observed in the measured data.

To further examine this result, we present transconductance versus temperature at a fixed value of collector current density in Fig. 2.2b. The transconductance per unit area g_m is calculated as the slope of the current-voltage curve at a fixed bias, and for an ideal SiGe HBT it is given by $g_m = qJ_C/kT$. The measured transconductance exhibits a plateau to a lower value than the ideal value as temperature decreases. However, the transconductance values calculated from the slope of the calculated results in Fig. 2.2a are identical to the ideal values. Therefore, quasiballistic transport does not change the temperature dependence of the transconductance. The reason can be seen in Eq. 2.13 in which V_{BE} affects the electron density only through the left boundary condition n_L; therefore, a change in voltage affects current density in a way that is independent of the mechanism of carrier transport and thus preserves the diffusive temperature dependence regardless of the Knudsen number.

2.4 Discussion

Our analysis has showed that the predicted influence of quasiballistic transport on the IV characteristics of HBTs is inconsistent with the experimental observations. We now address several mechanisms that we have not included in our analysis. First, we have not incorporated the built-in field in the base region due to Ge grading. However, as in Ref. [87], the only effect of a field term is to modify M and thus change the value of c_1, and our conclusions are robust to such changes. Second, modern devices may have base doping levels exceeding 10^{19} cm^{-3} [4, 8, 88] to minimize base resistance and prevent carrier freeze-out. This high level of doping leads to degenerate carrier statistics,

while we have assumed non-degenerate statistics. However, non-idealities in the IV characteristics are observed at temperatures up to $\sim$ 80 K for which the electrons are non-degenerate, and the present analysis thus applies under relevant conditions. Further, in degenerate conditions the law of the junction overpredicts the minority carrier density, [89] implying that accounting for degenerate statistics would predict a further decreased collector current that again contradicts experiment. Lastly, the asymptotic solution is restricted to values of average Knudsen number such that $2\epsilon c_1 < 1$, which limits our analysis to a minimum base width of 40 nm for the chosen scattering rates. However, DC non-idealities were reported in devices with base widths on this order,[4, 7, 8] and again our analysis applies. Given these considerations, we conclude that quasiballistic transport is not responsible for non-ideal cryogenic DC characteristics of SiGe HBTs.

Finally, we discuss alternate explanations for the cryogenic non-idealities. Prior works have suggested that direct tunneling from the emitter to the collector is a possible origin of non-idealities in devices with narrow base widths $\sim 10\ nm$ [4, 7]. However, non-ideal cryogenic transconductance has been observed in first-generation SiGe HBTs with base widths on the order of 100 nm [6, 8] for which the direct tunneling current is expected to be negligible. Other reported evidence for a transition from trap-assisted transport to a tunneling or quasiballistic mechanism is the change in slope of the collector I-V characteristics [7, 8]. However, similar trends are observed in the forward regime of Schottky diodes [67, 90] for which direct tunneling or quasiballistic transport is not relevant, and the possibility of a similar mechanism occurring in SiGe HBTs has not been excluded.

We instead offer a hypothesis for the origin of cryogenic non-idealities as originating from spatial inhomogeneities in the base-emitter potential barrier. The earliest works on heavily doped p-n junctions reported temperature-independent slopes of cryogenic forward-bias I-V characteristics for voltages where band-to-band tunneling is unlikely to occur [91–93]. Extensive studies of Schottky diodes have reported a variety of cryogenic $I-V$ non-idealities including the so-called T_0 anomaly [94] and temperature-dependent ideality factors [65, 66, 95]. These non-idealities have been explained by inhomogeneities in barrier height [67] that exist even in high-quality epitaxial junctions such as $NiSi_2$/Si junctions and have been linked to the atomic structure of the inter-

face [96, 97]. In SiGe HBT junctions, non-ideal base currents and the resulting random telegraph noise have been attributed to voltage barrier height fluctuations arising from trap states in the base-emitter space charge region [98] such as those of electrically-active carbon defects [99]. Future work will examine whether such barrier inhomogeneities are capable of explaining the collector current non-idealities of SiGe HBTs.

2.5 Conclusion

In this chapter, we have reported a study of quasiballistic transport in SiGe HBTs using an exact, semi-analytic solution to the Boltzmann equation based on an asymptotic expansion method. We find that the predicted IV characteristics including quasiballistic transport are inconsistent with experiment. Specifically, our calculations including quasiballistic transport predict collector currents that are orders of magnitude smaller than the measured currents for a given base-emitter voltage and an unaltered temperature dependence of transconductance relative to the ideal value, both of which contradict experimental observations. We suggest that local fluctuations in the base-emitter barrier height could account for the non-ideal collector current as has been observed in Schottky diodes. The presence of these spatial inhomogeneities has not yet been tested in SiGe HBTs, and in the next chapter we directly explore this hypothesis using an experimental technique involving capacitance-voltage measurements.

Chapter 3

BASE-EMITTER JUNCTION INHOMOGENEITIES USING CAPACITANCE-VOLTAGE CHARACTERISTICS

This chapter was adapted in part from:

[1] Nachiket R. Naik et al. "Investigation of Cryogenic Current-Voltage Anomalies in SiGe HBTs: Role of Base-Emitter Junction Inhomogeneities". In: *arXiv preprint arXiv:2302.14210* (2023). DOI: arXiv:2302.14210.

As discussed in the previous two chapters, the anomalous current-voltage characteristics of cryogenic SiGe HBTs have been a topic of investigation for many years. In Chapter 2 we demonstrated through a theoretical calculation that quasiballistic transport is not the likely origin of the anomalous behavior. Instead, we hypothesized that spatial inhomogeneities in the base-emitter junction potential, similar to those seen in Schottky diodes, may be a relevant phenomenon. In this chapter, we introduce an electronic capacitance-voltage (CV) based method to probe the junction potential of SiGe HBTs at cryogenic temperatures, inspired from work on Schottky diodes in the 1980s and 90s. We then experimentally probe the barrier potential of the junction as a function of temperature using the CV characteristic. Then, by comparing this to the I-V derived barrier potential, we conclude that spatial inhomogeneities are in fact a relevant phenomenon that could explain the cryogenic anomalies of SiGe HBTs. Finally, we provide the likely physical origins for the spatial inhomogeneities as well as suggested directions to conclusively verify their presence.

3.1 Background and introduction to spatial inhomogeneities

SiGe HBTs have witnessed a range of technical advances aimed at improving their performance for high-speed and low-noise amplification applications. [11, 27, 100] These include architectural developments such as a reduction in emitter width, reduced base resistances and capacitances through advanced epitaxial techniques, [11] and enhanced gain and noise performance through doping optimization. [2, 18] While these advances have enabled the RF performance of SiGe HBTs to rival that of III-V HEMTs, [18] the explanation for

the cryogenic non-ideal current-voltage characteristics remains unclear, thus preventing an understanding of the physical limits on cryogenic SiGe HBT performance. [2, 12]

In Chapters 1 and 2, we have discussed the anomalous behavior in the cryogenic operation of SiGe HBTs observed as a saturated transconductance below $\sim$ 100 K, and temperature-dependent base-emitter junction ideality factor $n(T)$ that greatly exceeds unity. [4, 101] We have also highlighted discrepancies in the various mechanisms including quasiballistic transport [6, 12], direct tunneling [4], or trap-assisted tunneling [7] that have been reported in the literature as the origin of the observed non-idealities. In Chapter 2, we have reported through our work that quasiballistic electron transport cannot explain the observed collector cryogenic non-idealities, and that observations of these non-idealities in devices with base width of $\sim$ 100 nm [8] reduce the likelihood of tunneling currents as the origin. Finally, we hypothesized that spatial inhomogeneities in the base-emitter junction potential barrier could explain the non-ideal collector current behavior in modern SiGe HBTs.

The basis for the above hypothesis derives from the fact that similar anomalies have been observed and extensively investigated in Schottky diodes between the 1960s-1980s. [65, 66, 102–104] Specifically, it was observed that the ideality factor $n(T)$ showed various anomalous dependences on temperature below $\sim$ 77 K. [66–68] These anomalous ideality factor dependences were ultimately attributed to spatial inhomogeneities in the built-in potential Φ_{BI}. [67, 105–107] Although semiconductor junctions are often modeled as uniform across the lateral area, in fact various imperfections exist which affect the local electronic structure of the junction. Even at epitaxial interfaces, it was found that different crystallographic orientations [108–110] or the presence of dislocations [111, 112] can lead to potential barrier variations on the order of hundreds of mV. In Schottky junctions, these inhomogeneities have been directly observed using ballistic electron emission microscopy, which allows the local barrier height to be mapped with nanometer spatial resolution. [70, 113] Various theories and numerical analyses of the electrical characteristics of inhomogeneous junctions have been reported and lead to compatible conclusions. [67, 105, 106] For example, the theory of Werner and Güttler assumes a Gaussian distribution of barrier heights and makes several specific predictions regarding the temperature-dependence of the ideality factor and the relation

between the built-in potential as measured by different methods. Further, it was shown that different spatial distributions of barrier inhomogeneities may yield various trends of ideality factor versus temperature, with some closely resembling those seen in HBTs at cryogenic temperatures [67, Fig. 11]. However, an experimental test of these anomalous barrier potentials for SiGe HBTs has not yet been reported.

One experimental approach used to investigate non-uniform built-in potentials is its electrical characterization using two methods, CV and IV measurements at various temperatures down to the cryogenic temperatures. As the IV characteristics vary exponentially with barrier height whereas the CV characteristics vary with a weaker polynomial dependence, discrepancies in the extracted built-in potential between the two methods become apparent if spatial inhomogeneities exist. [65, 69] Since the thermally-activated mechanism of carrier injection across Schottky barriers and p-n junctions is essentially identical, this electrical characterization approach can be used to obtain evidence for the existence of barrier inhomogeneities in SiGe HBTs. However, such a study has not yet been reported.

Here, we perform this experimental investigation by characterizing the base-emitter built-in potential using IV and CV measurements in modern SiGe HBTs from room to cryogenic temperatures. We observe a marked discrepancy in the trends of Φ_{BI} versus temperature extracted from these methods, consistent with the presence of a spatially inhomogeneous base-emitter junction potential. Further, we observe strong agreement of our measurements with predictions of prior studies that analyze Gaussian-distributed barrier potential inhomogeneities. We suggest a possible physical origin of the inhomogeneities as Ge clusters or electrically active C impurities which are introduced to minimize dopant diffusion, and we discuss how the existence of barrier inhomogeneities could be further confirmed and mitigated in optimized devices.

3.2 Theory and methods

Theoretical framework for IV and CV extraction of the built-in potential

The theory of Werner and Güttler describes electrical transport over the lateral area of a Schottky junction with a spatially inhomogeneous barrier characterized by a mean barrier height and a variance. [105] The distribution of the

barrier heights is taken to be Gaussian, an assumption which is supported by local measurements of the barrier heights [69, Fig. 19.12]. The variance of the distribution is assumed to decrease with increasing junction bias due to the pinch-off of low-barrier patches of dimension less than the depletion length, a concept that was originally introduced in [106] and later developed in [67].

The theory makes several predictions regarding the trends of electrical characteristics with temperature and other parameters in junctions exhibiting voltage-independent ideality factors $n(T)$. In particular, $n(T)$, as determined from the slope of $I-V$ characteristics, is predicted to vary with temperature according to

$$n(T)^{-1} - 1 = -\rho_2 + \frac{\rho_3}{2kT/q} \tag{3.1}$$

where k is Boltzmann's constant, q is the electric charge, and ρ_2 and ρ_3 are constants describing a linear variation of the mean barrier height, $\overline{\phi_B}$, and variance, σ_s^2, with junction voltage U: [105, Eq. 23]

$$\Delta\overline{\phi_B} = \rho_2 U \tag{3.2a}$$

$$\Delta\sigma_s^2 = \rho_3 U \tag{3.2b}$$

A plot of $n(T)^{-1} - 1$ versus T^{-1} should therefore yield a line over some range of temperatures if any temperature-dependence of ρ_2 and ρ_3 is negligible.

In addition, the effective built-in potential Φ_{BI} can be measured using IV and CV characteristics, and discrepancies between the two measurements provide insight into barrier inhomogeneities owing to the difference in their functional dependence on Φ_{BI}. In more detail, the collector current I_C is given by the diode equation similar to Eq. 1.7:

$$I_C = A\exp(-q\Phi_{BI}/kT)\exp(qV_{BE}/n(T)kT) = I_{C,0}exp(qV_{BE}/n(T)kT) \tag{3.3}$$

where A is a constant prefactor that is used to lump the doping, mobility and base width terms, V_{BE} is the base-emitter voltage, and $n(T)$ is the measured ideality factor, defined as $\partial I_C/\partial V_{BE} = qI_C/n(T)kT$. $I_{C,0}$ is the collector saturation current that captures the built-in potential and prefactor terms.

The temperature dependence of the base-emitter built-in potential Φ_{BI}, relative to a value at a reference temperature, can be obtained by fitting the ideal portion of the $I_C - V_{BE}$ characteristics with (3.3) and neglecting any temperature-dependence of A. A log-linear Gummel plot between I_C and V_{BE} represents the following relationship:

$$\ln(I_C) = \ln(I_{C,0}) + \frac{qV_{BE}}{n(T)kT} \tag{3.4}$$

implying that the saturation current $I_{C,0}$ can be obtained from the intercept of the linear fit. Using this saturation current relative to a known saturation current at a reference temperature, the built-in potential $\Phi_{bi}(T)$ can be extracted as:

$$\ln(I_{C,0}(T)) - \ln(I_{C,0}(T_{ref})) = \frac{-q\Phi_{bi}(T)}{kT} + \frac{q\Phi_{bi}(T_{ref})}{kT_{ref}} \tag{3.5}$$

Similarly, $n(T)$ can also be extracted from the slope of the IV Gummel curves using Eq. 3.4. From Eq. 3.3, it is possible to deduce that small variations in Φ_{BI} over the emitter area can lead to a non-ideal increased collector current and $n(T) \gg 1$. This sensitivity to variations in Φ_{BI} is particularly true at cryogenic temperatures due to the $1/T$ dependence in the exponential.

The capacitance-voltage characteristics of the base-emitter junction may also be used to obtain the built-in potential, through the relationship of the potential barrier with the stored charge in the depletion region. [65, 69] The base-emitter depletion capacitance is a direct result of charge storage across both sides of the p-n junction depletion region. The magnitude of charge stored is given for a junction with constant doping as [Ch. 6][53]

$$Q_j(V) = A\sqrt{2q\epsilon N_{eff}(x)(\Phi_{bi} - V_{be})} \tag{3.6}$$

where $N_{eff}(x) = N_D N_A/(N_D + N_A)$ is the effective doping concentration, q is the electron charge and ϵ is the permittivity. It is important to note here that the Φ_{bi} is the same built-in potential barrier for current flow. Then, by differentiating with respect to the applied voltage, we obtain the depletion capacitance for a junction with uniform doping concentration

$$C_{BE}(V_{BE}) = A\sqrt{\frac{q\epsilon N_{eff}}{(\Phi_{bi} - V_{be})}} = \frac{C_{BE,0}}{\sqrt{(1 - V_{be}/\Phi_{bi})}} \tag{3.7}$$

where $C_{BE,0}$ is the zero-bias depletion capacitance. This relationship can be generalized for a junction with non-uniform doping concentration to give [69, 114]

$$C_{BE}(V_{BE}) = \frac{C_{BE,0}}{(1 - \frac{V_{BE}}{\Phi_{BI}})^m} \tag{3.8}$$

where instead of a square-root dependence, we have a characteristic exponent m. For a uniformly doped junction, $m = 1/2$. By performing a measurement of C_{be} vs V_{BE} at each operating temperature and fitting to Eq. 3.8 with Φ_{bi} and m as the two parameters, we can extract Φ_{bi} from the CV characteristics.

Finally, the inhomogeneous junction theory predicts that the barrier measured in these two ways should differ in magnitude and temperature dependence owing to the fact that current depends on V_{BE} exponentially while the capacitance varies with V_{BE} with a weaker polynomial dependence. The barrier as determined through CV characteristics is therefore typically interpreted as the mean barrier height, while that determined from IV characteristics is often less than the mean value due to the larger contribution from low-barrier regions. [105, 115] The theory gives a relation between these barrier heights as: [105, Eq. 14]

$$\Phi_{BI}(IV) = \Phi_{BI}(CV) - \frac{\sigma_s^2}{2kT/q} \tag{3.9}$$

Considering the form of $n(T)$ in Eq. 3.1, this relation is compatible with the empirical observation that $\Phi_{BI}(CV) \approx n(T)\Phi_{BI}(IV)$ [65] (see also [105, Sec. V]). Therefore, discrepancies between the Φ_{BI} extracted using these two methods are interpreted as evidence for the presence of spatial inhomogeneities in the junction potential.

Experimental methods: IV and CV characteristics

We now describe the measurement techniques and setup used to extract Φ_{bi} from the from $C_{BE} - V_{BE}$ and $I_C - V_{BE}$ characteristics from 20 – 300 K on an IHP SG13G3 SiGe HBT. These structures consist of discrete transistors from

the 130 nm process technology as well as the associated OPEN and SHORT de-embedding structures on one wafer, which was mounted on a stainless steel platform which is screwed onto the chuck of the probe station. The transistors were probed in a custom-built cryogenic probe station (CPS) described in detail in Refs. [13, 116]. The components of the probe station are modified to operate it in S-parameter mode which is depicted in Fig. 3.1 and Fig. 3.2. Primarily, a vector network analyzer (VNA, Keysight E5061B) is used to measure Y-/S-parameters. Further, no attenuators or pre-amplifiers are used in the input and output chains to enable direct probing of the DUT. A pair of Keithley 2400 sourcemeters outside the probe station are used to provide bias to both ports, connected through hermetic feedthroughs and phosphor-bronze wiring. We employed Nickel/Tungsten probes (40A-GSG-100-DP, GGB Industries) which are suitable for probing Al pads, instead of Berryllium Copper (BeCu). We note here that the choice of probe tips and probing conditions is important; Ni alloy probes are more suited to Al pads as they are less prone to oxidation. Also, even at 300 K, the probe measurements must be performed in vacuum to prevent contact variations due to rapid oxide formation on Al. Figure 3.4 displays a micrsocope image of the device wafer being probed in the CPS at 300 K under vacuum using Ni alloy probes.

Measurement of the $C_{BE} - V_{BE}$ characteristic can be performed through various techniques, but in this work we characterize the capacitance through RF parameters over a chosen frequency range at each bias point of interest. There are multiple configuration parameters that must be selected appropriately to enable a clean extraction and fitting of the CV characteristics. We now describe some of the experimental procedures used to arrive at the choices for these parameters.

The first choice regarding measuring the $C_{BE}-V_{BE}$ characteristic is to do with the appropriate bias regime. Fig. 3.3 provides a simplified schematic of the small-signal model of the intrinsic SiGe HBT. Relative to the full schematics shown in Ref. [12], the first simplifying assumption we can make by restricting the bias range is to neglect contributions of the series resistances at each of the terminals (not displayed in Fig. 3.3). We do this by measuring in the reverse-bias to low-forward bias regime [-0.5 V, $+0.5$ V], well below the forward-active regime (FAR), to minimize the current loads on each of the terminals. Further, these series resistances are typically on the order of $10\Omega.\mu m^2$ or smaller, and

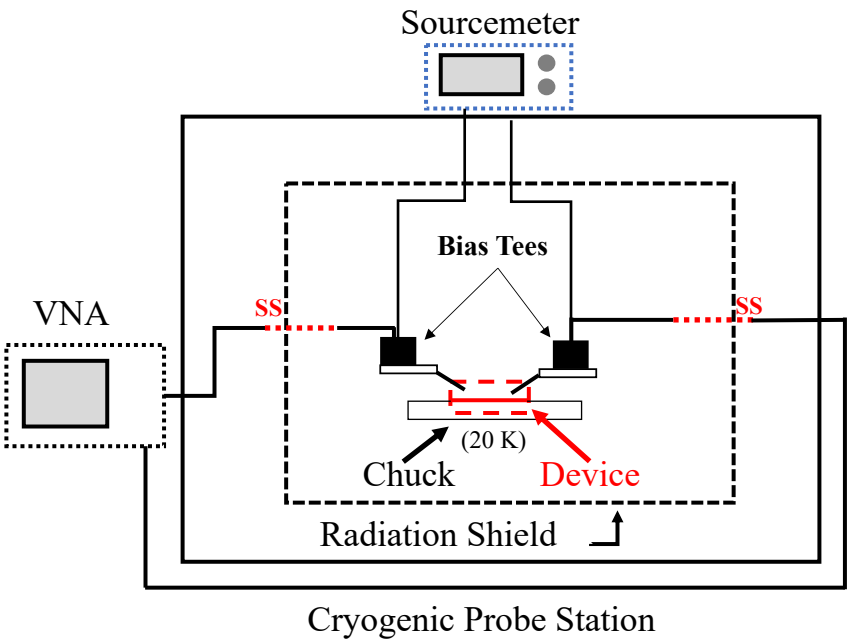

Figure 3.1: Schematic representation of the custom-built cryogenic probe station used to extract temperature-dependent IV and CV characteristics of discrete transistors. This setup is modified from the noise-mode setup described in Ref. [116] to include a VNA instead of a noise source, and remove the pre-amplifier and attenuators used for the cold attenuator method. The devices are place on the temperature controlled chuck that is able to stabilize at temperatures between 20 – 300 K. Bias-tees are used to provide DC bias independent of the RF pathway. Copper braided straps are used to thermally ground the bias-tees to the coldfinger. Stainless steel (SS) inner-conductor cables are used closer to the device to minimize thermal load.

therefore will result in an even further reduced voltage drop across them. By restricting CV measurements to this voltage regime, we may also neglect the contributions of the transconductance g_m which is only appreciably high in FAR. Most importantly, V_{BE} being restricted to $[-0.5\text{ V}, +0.5\text{ V}]$ minimizes the contributions of diffusion capacitance, allowing us to probe the pure depletion capacitance C_{BE}. These assumptions are verified using the measured $Y-$parameters in the next section.

The next choice is regarding the RF bias conditions provided to each of the terminals. At first glance, from Fig. 3.3 we might be tempted to perform a simpler, 1-port Y-parameter measurement at port 1, the base port, while leaving port 2, the collector port Open. In theory, this RF measurement should give us C_{BE} through Y_{11} vs frequency as

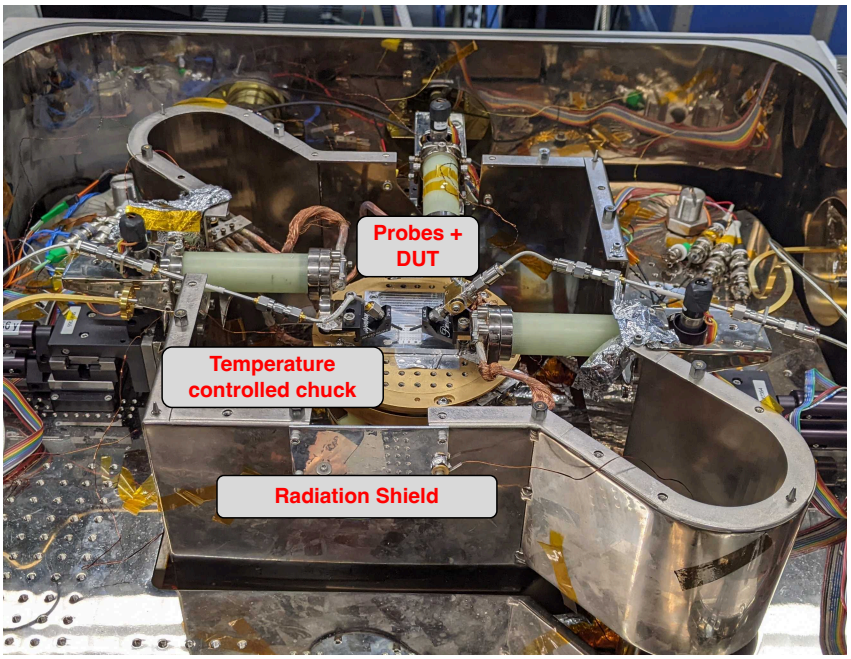

Figure 3.2: Layout of the CPS in S-parameter mode, with probes and bias-tees remaining, but input attenuator and output pre-amplifier removed. The DUTs are epoxied to a metal plate that is bolted down to the temperature-controlled chuck. RF cables to the input and output use stainless steel inner conductors and are thermally strapped to the coldfinger to minimize thermal load.

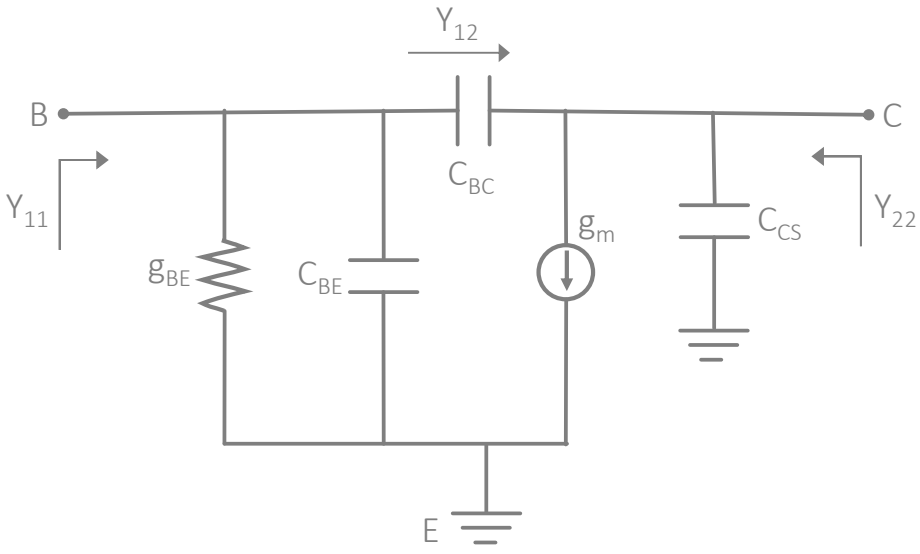

Figure 3.3: Intrinsic region small-signal model schematic for a typical SiGe HBT operating in common-emitter mode. Under reverse-bias conditions at the base-emitter junction, no current flows through the collector and therefore the transconductance $g_m = 0$. The $Y-$ parameters measured in this biasing regime allow for an extraction of the displayed depletion capacitances, including C_{BE}.

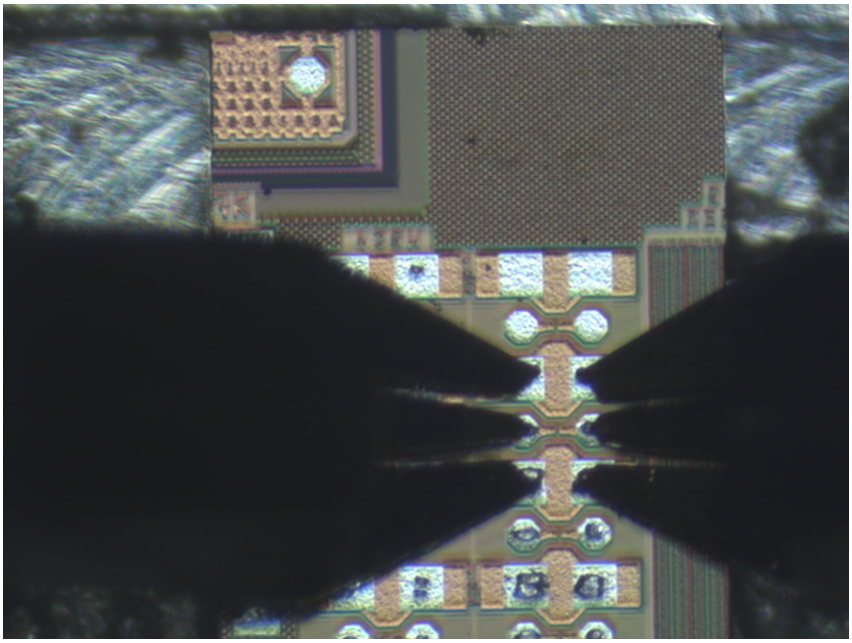

Figure 3.4: Microscope image of an IHP SG13G2 130nm process wafer being probed in the CPS under vacuum. The probes used here are Nickel alloy suited for Al pads. The wafer consists of various test structures, including one SiGe HBT device (depicted here as the landing target), and associated OPEN and SHORT de-embedding structures. Device maps were obtained from IHP Solutions.

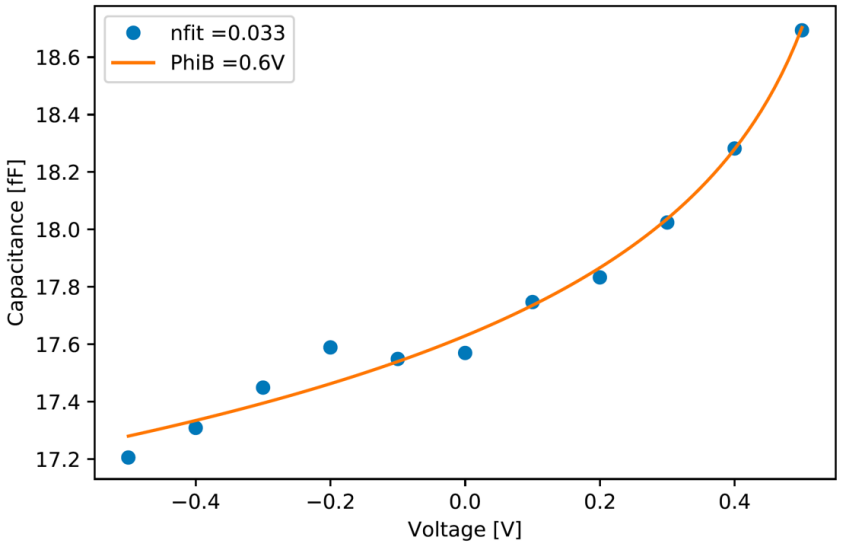

Figure 3.5: Representative dataset for a measured $C_{BE} - V_{BE}$ sweep at 300 K for the IHP HBT devices using a 1-port measurement technique. The results of the fitting to Φ_{BI} and the characteristic exponent m, denoted here as nfit, are also displayed. The non-monotonic kink in the CV characteristic near 0 V is consistently observed across multiple devices and experimental trials, and results in unphysical values for the fits.

$$Y_{11} = g_{BE} + j\omega C_{BE} \tag{3.10}$$

where g_{BE} is the base-emitter conductance, and $\omega = 2\pi f$ is the angular frequency. With the collector port left Open, there should be no current pathway through the collector, making the base-collector depletion capacitance C_{BC} invisible to the Y_{11} measurement. However, when the 1-port CV characteristics were performed at 300 K, a repeatable kink near $V_{BE} = 0$ V was observed consistently across multiple HBT devices, as shown in Fig. 3.5. The non-monotonicity due to the kink is uncharacteristic of a depletion capacitance trend with voltage and results in unphysical fits for Φ_{BI}. This origin of this kink in the $C_{BE} - V_{BE}$ was identified as being due to incorrect accounting of the through capacitance C_{BC}. While no current path through the C_{BC} is expected due to the collector being left open, the collector-substrate capacitance C_{CS} provides an alternate RF current path to ground due to the substrate being grounded. This results in some dependence of C_{BC} and C_{CS} through Y_{11}. Further, with no controlled bias provided at the collector terminal, small voltage fluctuations due to static buildup or DC offsets can alter the value of the depletion capacitance C_{BC}, and therefore C_{BE}. After this conclusion, the choice was made to capture $C_{BE} - V_{BE}$ characteristics while applying a known, constant V_{BC} and accounting for the presence of C_{BC} in Y_{11}, similar to the standard procedure in literature [69, 101].

Finally, the measurement parameters of the VNA must be chosen appropriately. The frequency range of measurement was chosen based on the frequency ratings of the components in the CPS. A range of RF powers supplied through the VNA between -35 dBm and -10 dBm were tested, and an input signal power of -20 dBm was found to provide a relatively low-noise CV sweep without any risk of power saturation of the device. The most important RF measurement parameter however was found to be the total sweep time. The original configuration set for the Y-parameter measurement involved a sweep over 501 frequency points, with 100 ensemble averages and an IF bandwidth of 10 kHz, repeated for 11 bias points. This resulted in a total sweep time for a $C_{BE} - V_{BE}$ measurement of $\sim$ 180 s. Looking closer at the extracted C_{11} versus time of measurement, a time-dependent drift of capacitance on the order of 1 fF for a fixed bias point was observed, which in turn manifested as kinks in the C_{BE} plot. This time-dependent drift is likely due to contact vari-

ations on probe landing as well as $1/f$ gain fluctuations in the measurement system. Therefore, to reduce the impact of time-dependent drift, the VNA was configured to sweep across 11 frequency points with 10 ensemble averages to lower the total sweep time. As a tradeoff, the IF bandwidth was lowered to 1 kHz to reduce signal noise. This reduced the total sweep time to 11 s where no time-dependent drift or kinks were observed.

With the preliminary experiments required to establish the measurement parameters and configurations complete, we now describe the finalized measurement details. We perform a 2-port Y-parameter measurement of the SiGe HBT discrete device in the CPS across a 20 – 300 K temperature range. In reverse-bias and low-forward bias regimes, the Y-parameters related to port 1 of the intrinsic SiGe HBT are given by: [12, Appendix D]

$$Y_{11} = g_{BE} + j\omega(C_{BE} + C_{BC}) \tag{3.11}$$

$$Y_{12} = -j\omega C_{BC} \tag{3.12}$$

The base-emitter capacitance can therefore be expressed as:

$$C_{BE} = (Im(Y_{11} + Y_{12}))/2\pi f. \tag{3.13}$$

As mentioned above, the range of V_{BE} is restricted to [−0.5 V, +0.5 V], below the forward active regime (FAR), to minimize the contributions of the transconductance and diffusion capacitance. While V_{BE} is swept between [−0.5 V, +0.5 V] at intervals of 0.1 V, $V_{BC} = 0$ V is held constant to hold the C_{BC} depletion capacitance constant. The Y parameters are measured in $1 - 3$ GHz frequency range and the extractions were performed at 2.4 GHz. The lower limit of frequency is set by the operating frequency of the bias-tees, and the upper limit is chosen to minimize the effects of any inductive components. At these frequencies, it was observed that the imaginary part of Y_{11} is linear in frequency, indicating purely capacitive behavior. Short-Open-Load-Through (SOLT) calibration was performed on a CS-5 calibration standard at each temperature, and the shunt parasitic capacitance at the input of the device was de-embedded using an OPEN structure. The intermediate-frequency bandwidth (1 kHz) and frequency points (every 0.2 GHz) were selected to limit the

total sweep time to less than 15 s to avoid drift due to changes in contact and Allan variance effects.

At each bias, Y-parameters were swept across frequency and ensemble-averaged 10 times. Φ_{BI} was extracted from a sweep of C_{BE} versus V_{BE} by fitting the parameters Φ_{BI}, $C_{BE,0}$ and m as in (3.8) using a trust region reflective algorithm from the SciPy library. [117] Φ_{BI} was constrained to [0.5 V, 1.2 V], $C_{BE,0}$ was constrained between the minimum and maximum values of the sweep, and m was constrained to [0, 1] based on physical limits of these parameters.

3.3 Results

Fig. 3.6a shows the collector current I_C versus V_{BE} at various temperatures between 20 K and 300 K. Consistent with prior findings, [4, 8, 12] the measurements exhibit deviations from drift-diffusion theory at cryogenic temperatures, with the curves exhibiting a weakening dependence on temperature below $\sim$ 80 K. At high-injection current values $>$ 1 mA, current rolloff due to second-effects can be seen; however, this regime of current is not used in the fitting procedure. The noise floor of the IV characterisitic is $\sim 10^{-8}$ A which is set by the length of phosphor-bronze DC cables used between room temperature to 20 K to minimize thermal leakage to the chuck. Current values below 10^{-8} A are difficult to resolve due to voltage fluctuations along these lines.

Next, $n(T)$ at each physical temperature is extracted from the slope obtained by fitting a line to the log-linear region of each curve in Fig. 3.6a as described in Eq. 3.4. The current range used for this fitting is limited to 0.02 mA. We plot the extracted ideality factor $n(T)$ as $T_{eff} = n(T)T_{phys}$ versus T_{phys} in Fig. 3.6b. T_{eff} is observed to deviate from the ideal predictions of (3.3), plateauing to $\sim$ 100 K due to $n(T) > 1$ at cryogenic temperatures as has been reported previously [12]. This corresponds to an ideality factor of $\sim$ 5.0 at T_{phys} = 20 K. These two results confirm that devices tested display similar cyrogenic anomalies as observed in prior literature.

Finally, in Fig. 3.7 we plot the fitted collector saturation current $I_{C,0}$ versus temperature as extracted from the measured IV characteristics. The extracted $I_{C,0}$ are compared to the values predicted from the ideal temperature dependence of the saturation current. It is assumed for this model that the $1/T$ in the exponential is the dominant temperature dependence relative to that of the prefactors. The measured temperature dependence of $I_{C,0}$ is similar to

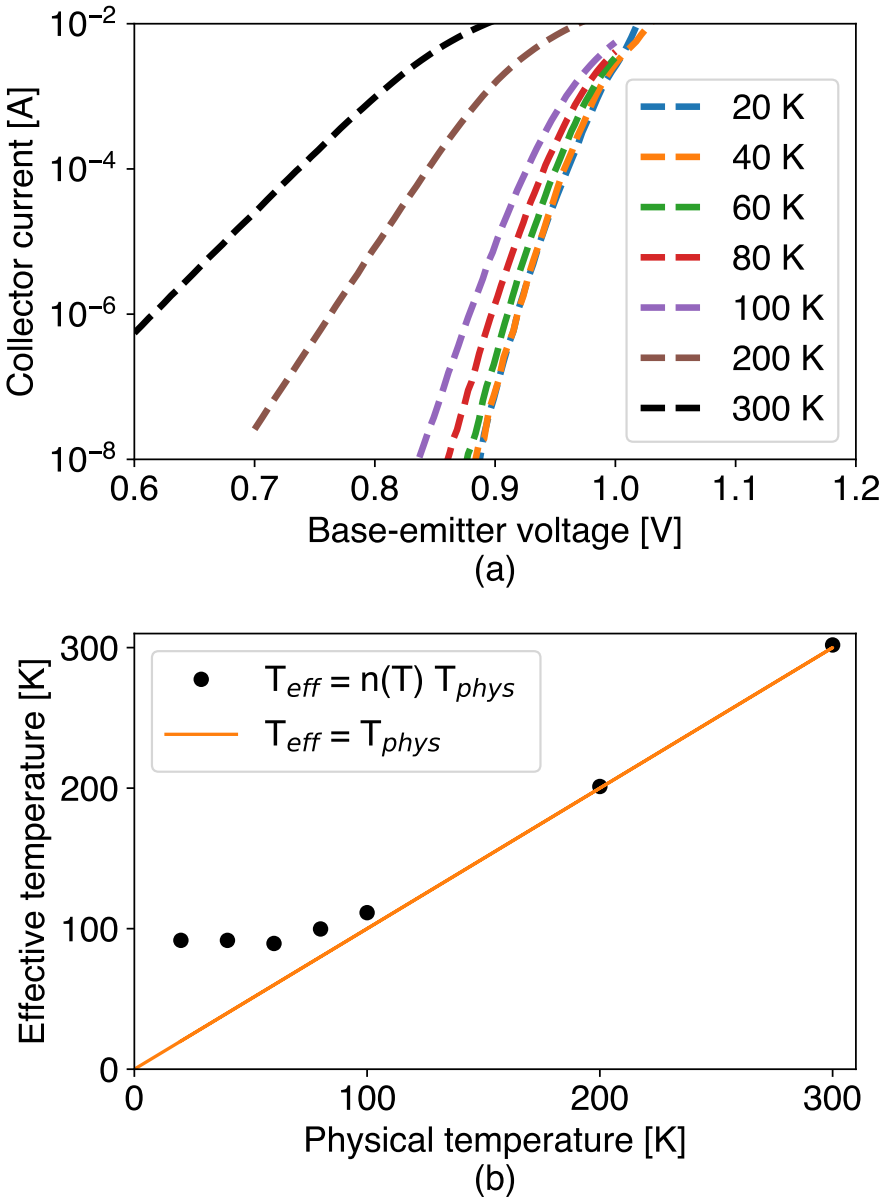

Figure 3.6: (a) Measured I_C versus V_{BE} for various temperatures. The characteristics become independent of temperature at cryogenic temperatures $\sim$ 80 K. (b) $T_{eff} = n(T)T_{phys}$ vs T_{phys} from measurements (symbols) and theory (line), indicating the non-ideality of the base-emitter junction at cryogenic temperatures.

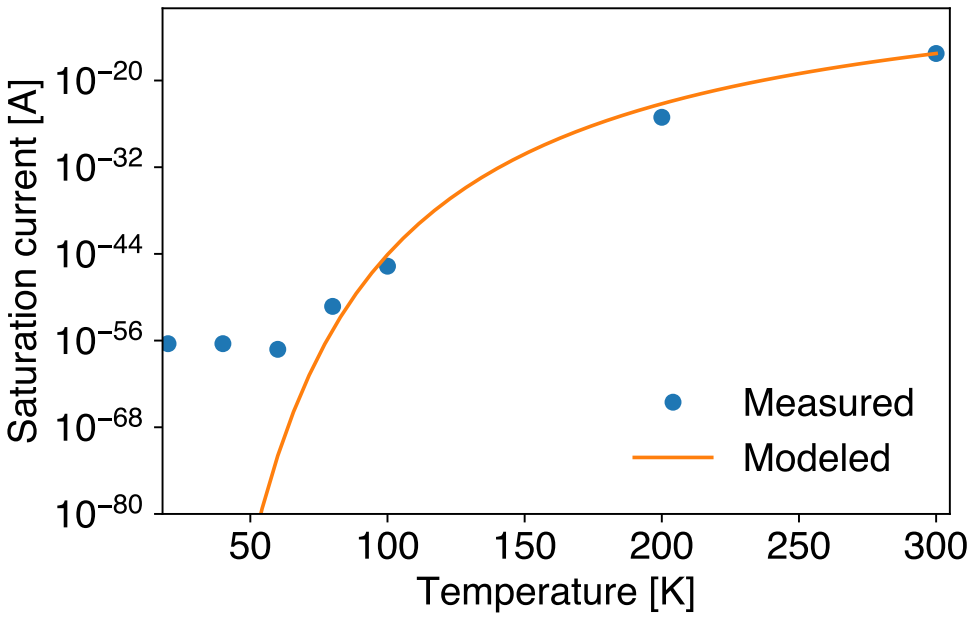

Figure 3.7: Saturation collector current $I_{C,0}$ versus physical temperature extracted from fits to the measured IV characteristics. Also plotted is a comparison to modeled predictions of the ideal temperature dependence of $I_{C,0}$. The deviation from the model predictions at cryogenic temperatures points to the presence of a non-ideal low-potential barrier region.

that observed in the literature for similar devices, validating our extraction method.[101] From the observed deviation of $I_{C,0}$ away from the ideal predictions below $\sim$ 80 K, we can expect that the temperature dependence of the IV extracted Φ_{bi} will show similar non-ideal behavior.

We next examine the measured RF characteristics. Fig. 3.8a plots the raw, measured data for $Im(Y_{11})$ and Fig. 3.8b for $Im(Y_{12})$ in a narrow frequency range across the entire V_{BE} sweep at 300 K. We observe that $Im(Y_{11})$ is linear in frequency across all biases, indicating a purely capacitive behavior in this frequency range. Similar, $Im(Y_{12})$ demonstrates the expected linear trend and is < 0, as is expected from Eq. 3.12. Further, we see that the capacitance C_{BC} that is captured by the slope of $Im(Y_{12})$ remains constant as intended with a $V_{BC} = 0$ V. Using this data, the $C_{BE} - V_{BE}$ characteristics can be calculated.

Fig. 3.9a plots a sweep of $Im(Y_{11} + Y_{12})/\omega$ versus f for various V_{BE} at 300 K, where $\omega = 2\pi f$. A narrowed frequency range from the 1$-$3 GHz measurements is plotted to aid in distinguishing the curves. The de-embedded base-emitter

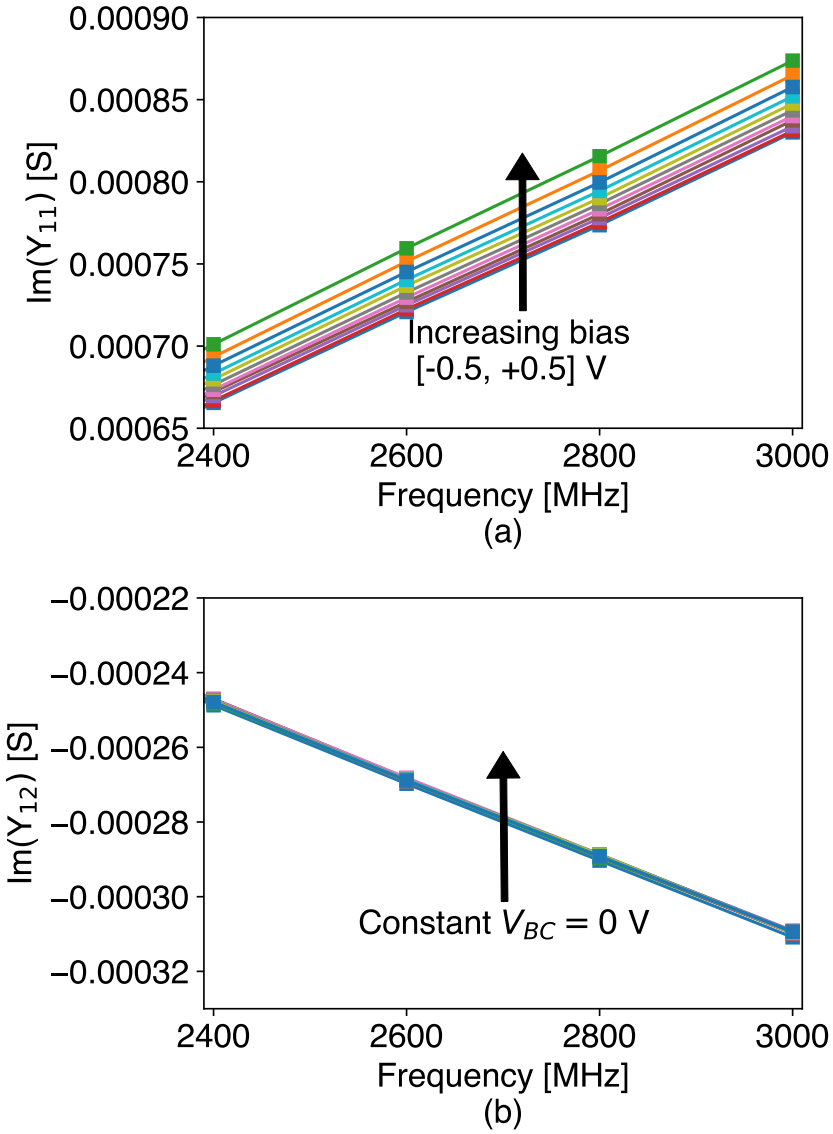

Figure 3.8: (a) Measured data for $Im(Y_{11})$ versus frequency across all V_{BE} bias points. A narrow frequency range is plotted to distinguish the curves. The plot is linear in frequency confirming a pure capacitive behavior, and the capacitance value given by the slope of the line increases with increasing bias. (b) Measured $Im(Y_{22})$ versus frequency for a V_{BE} sweep with V_{BC} held constant at 0 V. The lines coincide almost perfectly indicating a constant C_{BC} value that is extracted from the negative of the slope.

capacitance C_{BE} is directly obtained from this plot by averaging across the frequency range. We see a relatively flat dependence of $C_{BE} = Im(Y_{11}+Y_{12})/\omega$ on frequency indicating ideal depletion capacitance behavior, and a steady increase in the value with increasing forward bias. Using this data, we are able to plot the capacitance-voltage characteristics and fit to Eq. 3.8 for Φ_{bi} and m at each temperature. Fig. 3.9b plots the resulting C_{BE} versus V_{BE} at three representative temperatures across the overall range, along with the fitted curves from (3.8). The error bars, representing the 2σ error in C_{BE}, are obtained from statistical analysis of the 10 $C-V$ sweeps performed at each temperature.

Following the discussion in Sec. 3.2, these data are analyzed to obtain Φ_{BI} from the $I_C - V_{BE}$ and $C_{BE} - V_{BE}$ characteristics. At room temperature, $\Phi_{BI}(CV)$ is found to be 0.83 V, in good agreement with observations in the literature. [101] This value is specified as the room temperature reference value for $\Phi_{BI}(IV)$ to facilitate the extraction at other temperatures.

Fig. 3.10 plots the extracted Φ_{BI} from both IV and CV measurements versus T_{phys}. For $\Phi_{BI}(CV)$, the error bars represent the 2-σ error in Φ_{BI}, obtained by performing fits with Eq. (3.8) for 100 $C_{BE} - V_{BE}$ sweeps generated with error values randomly determined based on a normal distribution defined by the uncertainty in the measured C_{BE}. The extracted $\Phi_{BI}(CV)$ is observed to weakly increase with decreasing temperature, consistent with observations for similar devices [101] and Schottky diodes [65]. In contrast, $\Phi_{BI}(IV)$ exhibits a stronger dependence on temperature and deviates sharply from $\Phi_{BI}(CV)$ below $\sim$ 100 K, similar to what was observed observed previously for Schottky diodes [65, 69]. This marked deviation in magnitude from the $\Phi_{BI}(CV)$ is interpreted as a signature of a non-uniform barrier potential and the likely presence of lateral spatial inhomogeneities. Following a method employed in the Schottky junction literature, [65] we also plot $\Phi_{BI}(IV)n(T)$, which for Schottky junctions have been empirically observed to agree with the measured $\Phi_{BI}(CV)$. This effect is also observed in the present data for the SiGe base-emitter junction, indicating that modifying the barrier potential by the IV derived $n(T)$ can explain the observed temperature deviation within the error bounds of the measurement.

The error bars for $\Phi_{bi}(CV)$ are observed to get slightly larger at cryogenic temperatures due to increased uncertainty in C_{be}. This is likely due to ther-

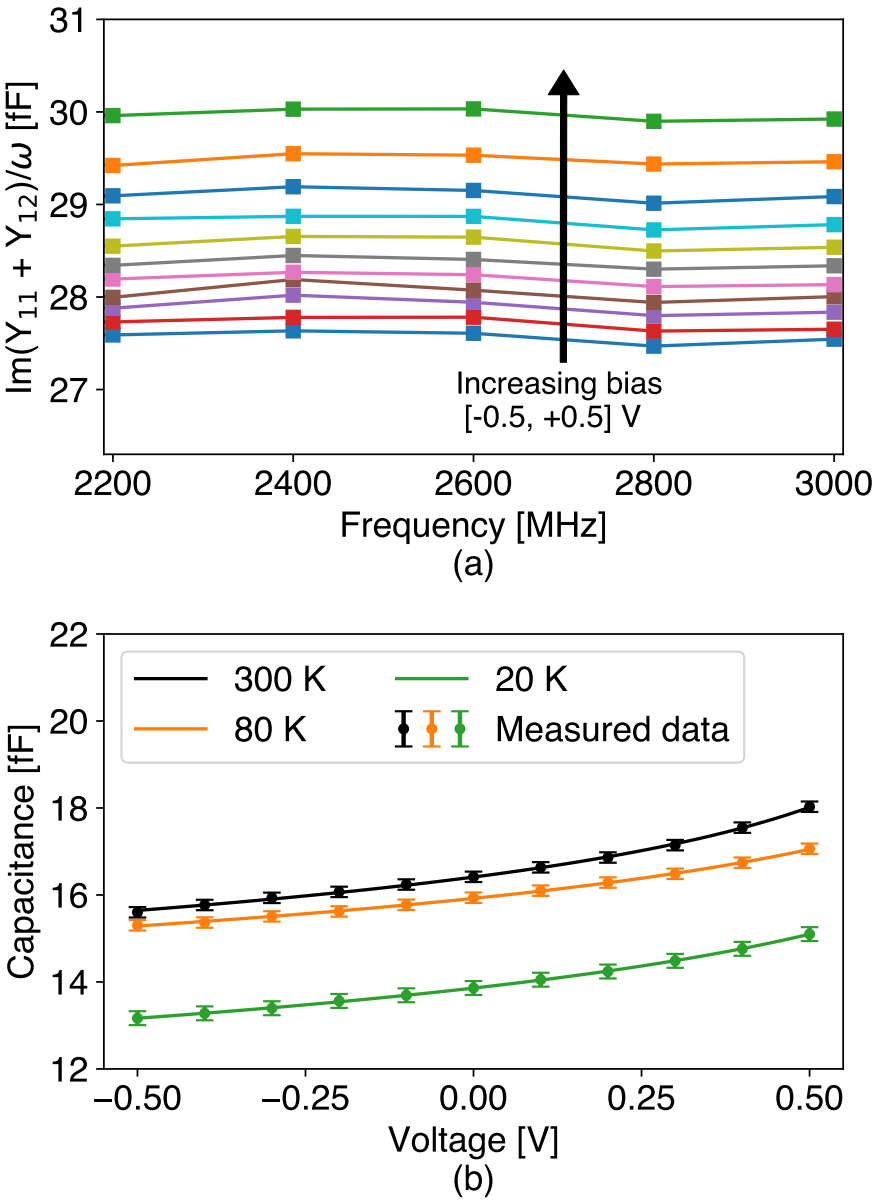

Figure 3.9: (a) Measured $Im(Y_{11} + Y_{12})/\omega$ (symbols) versus f at 300 K for various V_{BE} in steps of 0.1 V. The flat dependence of the capacitance of the base-emitter junction with the frequency and a steadily increasing capacitance with bias indicates a pure depletion capacitance. (b) Measured (symbols) and fitted (solid lines) C_{BE} versus V_{BE} at 300 K, 80 K and 20 K. As a representative example, the fit for 300 K yields $\Phi_{BI} = 0.83$ V and $m = 0.10$.

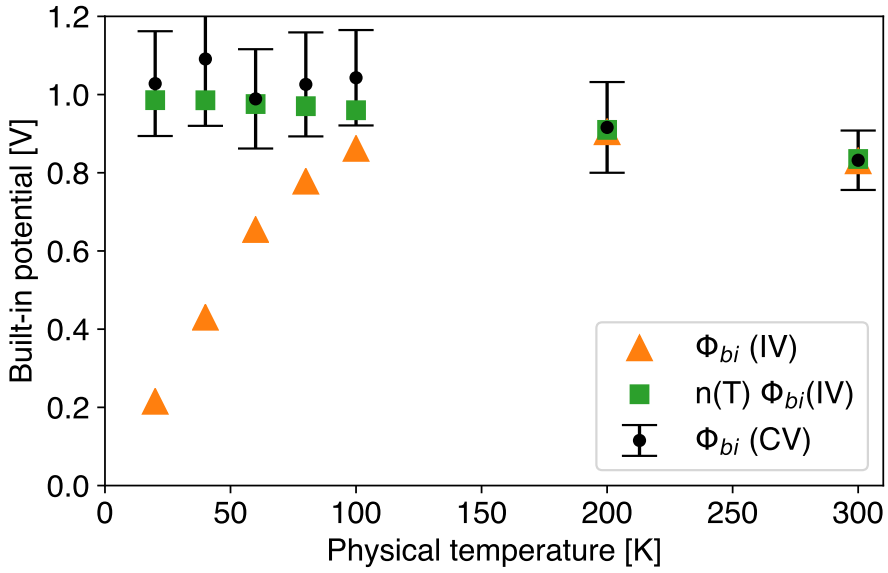

Figure 3.10: Built-in potential Φ_{BI} versus physical temperature from CV (black circles) and IV (orange triangles) measurements. Also plotted is the empirical relation $n(T)\Phi_{BI}(IV)$ (green squares) from the Schottky junction literature. The measured $\Phi_{BI}(CV)$ agrees well with this quantity, supporting the existence of lateral spatial inhomogeneities in Φ_{BI}.

mal drift and variations in probe-tip contact which are likely induced by the vibrations from coldhead operation. Error bars are not detectable for $\Phi_{bi}(IV)$ as the uncertainty bound for the IV measurement is two orders of magnitude below the current range used for the fitting.

We now examine the agreement between the data and the predictions from the inhomogeneous junction theory of [105]. Equation 3.1 predicts that $n(T)^{-1}-1$ versus T^{-1} should be a straight line over some range of temperatures, assuming ρ_2 and ρ_3 to be independent of temperature. Figure 3.11 plots this quantity for the present device and other devices with data obtained from [12, Fig. 5.8]. For all the devices, the expected trend is observed over a temperature range which is comparable in relative width to that in [105, Fig. 9], confirming the prediction.

Two regimes of deviation from the linear trend are observed at high and low temperatures. At high temperatures ~ 300 K, $n(T)^{-1}-1$ plateaus to zero for all the devices, corresponding to an ideal junction with $n=1$. This deviation was also observed in [105, Fig. 8] and is expected since $n \geq 1$ for fabricated junctions, meaning $n(T)^{-1}-1 \leq 0$. It could be explained by a temperature-

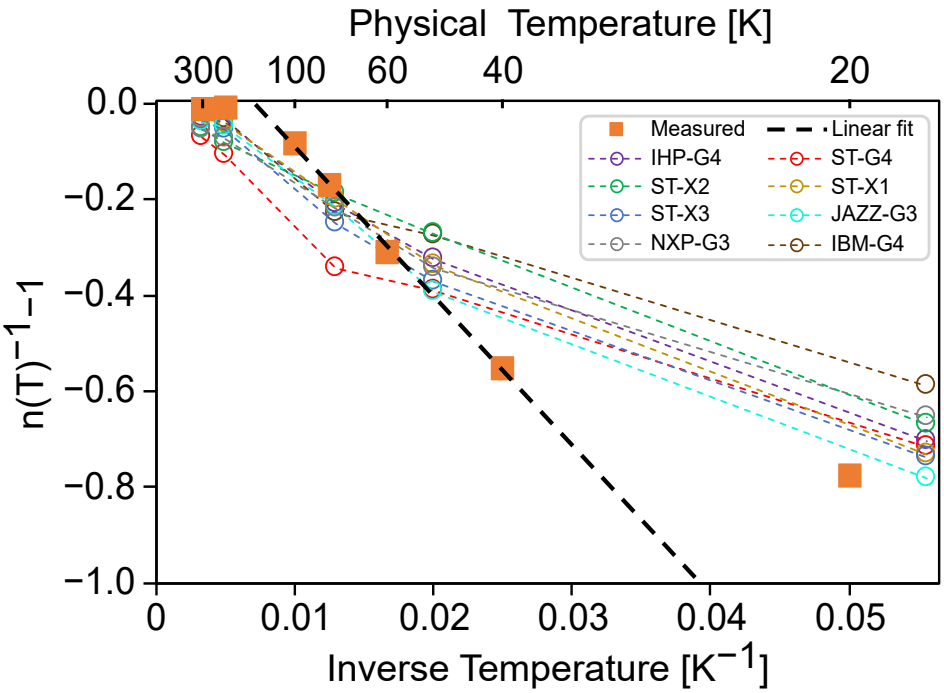

Figure 3.11: Measured inverse ideality factor $n(T)^{-1}-1$ versus inverse physical temperature T^{-1} for measured data on the SG13G2 (base width $<$ 20 nm) with a linear fit to the data in 40-100 K following the prediction in [105]. Data obtained from older-generation devices [12, Fig. 5.8] are also shown.

dependence of ρ_2 and ρ_3 which was neglected in this work and in [105].

The SG13G2 also exhibits a deviation from the linear trend at low temperature ($\sim$ 20 K). This discrepancy could be attributed to the presence of a direct tunneling current which has been previously reported to exist in highly-scaled devices. [4, 101] The present device has a base width less than 20 nm, [118] and so direct tunneling could occur. The older-generation devices exhibit the linear trend down to 20 K, which is compatible with the absence of tunneling current in these devices with larger base widths. Despite these deviations, overall the experimental trends are in good qualitative agreement with the theoretical predictions of the inhomogeneous barrier theory.

Semi-quantitative information regarding the variation of the barrier height variance with bias for the present device can be obtained from the linear fit in 3.11. If $\rho_2 + \rho_3/(2kT/q) \ll 1$, the theory of [105] described in Section 3.2 reduces to the T_0 model for non-ideal junctions which has been extensively studied in the Schottky junction literature. [67, 102, 105] In this case, the slope of the linear fit in 3.11 is simply T_0. Performing this fit for the present

data yields $T_0 \approx 30$ K, a value which is generally compatible with values for Schottky diodes compiled in [105]. T_0 in turn can be linked to ρ_3 as: [105, Eq. 33]

$$T_0 \approx -\frac{\rho_3}{2k/q} \tag{3.14}$$

We obtain a value $\rho_3 = -5.2$ mV. The magnitude of this value indicates that changes in standard deviation of the potential barrier height distribution with base-emitter bias of less than a percent of the mean barrier height are sufficient to account for the observed electrical anomalies.

3.4 Discussion

The agreement of our data with the predictions of the inhomogeneous barrier theory suggests that inhomogeneities in the base-emitter junction potential of SiGe HBTs could contribute to the cryogenic electrical anomalies. The similarity of the base-emitter junction characteristics with those reported for Schottky junctions provides evidence supporting a similar underlying physical mechanism, lateral inhomogeneities in Φ_{BI} across the emitter area. Further, the agreement of $\Phi_{bi}(IV)n(T)$ with $\Phi_{bi}(CV)$ suggests that a non-ideal barrier profile can explain the anomalous $n(T) \gg 1$ values at cryogenic temperatures. Similar to Ref. [65], a simple empirical model to account for non-ideal barrier heights is to define an effective barrier height $\Phi_{bi}^{eff} = \Phi_{bi}(IV)n(T)$ that is then used in the $I_C - V_{be}$ relationship

$$I_C(T) = A \exp \frac{-q\Phi_{bi}(IV)}{n(T)kT} \exp \frac{V_{BE}}{n(T)kT} \tag{3.15}$$

which may model the cryogenic Gummmel curves of SiGe HBTs better.

We note that other mechanisms for cryogenic IV anomalies such as electron tunneling [8], conduction band tail effects [119], and junction periphery effects may still play a role, and further study is necessary to test these other possibilities. Additional evidence for the barrier inhomogeneity hypothesis could be obtained using techniques employed previously for Schottky junctions which directly measure the spatial profile of the built-in potential such as ballistic emission electron microscopy (BEEM). [69, 70] This method has enabled inhomogeneities in Schottky barriers to be attributed to specific material defects

such as dislocations. [120] Other methods which would be applied without requiring specialized samples might include transmission electron microscopy or a combination of device physics simulations and electrical measurements. However, none of these methods give as direct evidence as BEEM.

We now discuss material defect origins of the base-emitter junction potential inhomogeneities in HBTs. Prior modeling studies of Schottky junctions have found that variations in barrier potential on the scale of the space-charge region (SCR) width can result in $n(T) \gg 1$ at cryogenic temperatures. [67, 68] Further, for Co metal-silicide Schottky contacts, the presence of Co clusters have been identified as the origin of low Schottky barrier height regions. [121] In HBTs, the relevant defects could be Ge clusters [122] or electrically active carbon defects [99]. Non-uniform Ge content over a few nanometers in SiGe p-wells with Ge concentration $\geq 30\%$ has been reported to lead to the degradation of electrical properties like hole mobility. [122] Trap states associated with C impurities have also been detected in modern HBTs, [99] and it has been shown that similar trap states in the space-charge-region (SCR) can result in voltage barrier height fluctuations. [98] With Ge concentrations for modern HBTs being on the order of 30% [4] and C doping on the order of 10^{20} cm^{-3}, [1], these defects could be responsible for spatial potential inhomogeneities at the base-emitter junction. Fig. 3.12 provides a schematic representation for the anticipated type of barrier fluctuations along the emitter width dimension x. The observation that the barrier height does not diverge between IV and CV characteristics at 300 K, but does so sharply at cryogenic temperatures indicates that the the fluctuations $\delta\Phi_{bi}$ need only be a small fraction of the mean potential barrier height and can occupy a relatively smaller region.

The precise origin of these inhomogeneities in terms of materials defects will require a thorough characterization of the structural and electrical properties of carefully prepared SiGe heterojunctions. If the presence of spatial inhomogeneities across the emitter area is verified, a less aggressive Ge doping concentration and profile, especially in narrow-base SiGe HBTs, could decrease the concentration of these defects and thereby lead to a more uniform base-emitter junction potential. The impact of structural properties on the electrical properties can be characterized by correlating atomic-structural and electrical characterizations of SiGe heterojunction structures with varying Ge profiles.

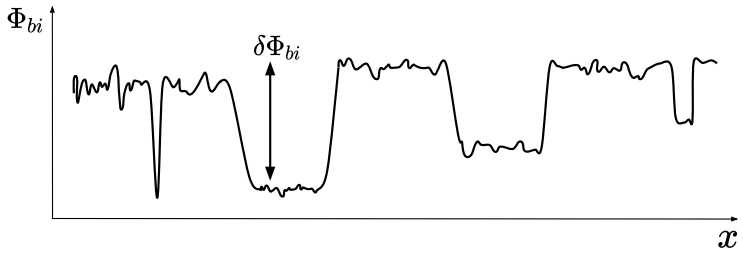

Figure 3.12: Schematic for the profile of the base-emitter potential barrier Φ_{bi} that is anticipated in SiGe HBTs (not to scale). x is the lateral dimension along the emitter width. Perturbations in the barrier $\delta\Phi_{bi}$ can vary in magnitude and spatial density; however, at cryogenic temperatures, narrow width inhomogeneities that are fractions of Φ_{bi} may be adequate to explain the observed IV anomalies.

Finally, we discuss the possible improvements in low-noise amplifier performance that may be obtained with more ideal base-emitter junctions. A more uniform base-emitter junction potential will result in cryogenic transconductance and collector current values which are closer to their ideal values. Further, improved ideality in these DC parameters directly affects the minimum noise temperature T_{min} of HBTs. For example, a decrease in T_{eff} from 80 K to the physical temperature 20 K, corresponding to an ideality factor at 20 K of $n = 1$ instead of $n = 4$, linearly improves the achievable T_{min} by a factor of 4 in the low-frequency and low base-resistance limit (see [2, Eq. 2]). Therefore, decreasing inhomogeneities in the base-emitter junction potential is expected to lead to improved cryogenic microwave noise performance, advancing their use in scientific and industrial applications.

3.5 Conclusion

In this chapter, we have reported measurements of the built-in potential of the base-emitter junction and its temperature dependence of a SiGe HBT using IV and CV characteristics. The differing values of the built-in potential at

cryogenic temperatures obtained from these two methods supports the origin of cryogenic electrical anomalies as arising from spatial inhomogeneities in the base-emitter junction potential. The physical origin of these barrier inhomogeneities is hypothesized to be Ge clusters or C impurities. Further characterization of carefully fabricated Si:SiGe junctions will have to be performed to verify and mitigate the impact of spatial inhomogeneities on the cryogenic DC and microwave noise performance of SiGe HBTs.

Chapter 4

REDUCING MINIMUM ACHIEVABLE NOISE TEMPERATURE IN SIGE HBTS: THE EFFECTS OF SHOT NOISE CORRELATION

In this chapter, we model and attempt to measure the effects of shot noise correlation at cryogenic temperatures in a SiGe HBT using the cold probe station mentioned in the previous chapter. We first use an existing small-signal model for a device and incorporate the effects of shot noise correlation to develop an expectation of the magnitude of deviation in noise temperature relative to modeling with no correlation. We find that the largest gains in noise performance are expected at frequencies between 20 - 100 GHz. While measuring noise accurately at these high frequencies requires dedicated development of a noise setup, we modify the probe station to measure noise temperature between 14 - 18 GHz where we expect to see the effects of shot noise correlation without the introduction of errors associated with higher frequency operation. However, we find that due to the narrow operating bandwidth of the setup and sources of error in the noise measurement technique, capturing the shot noise correlation at these frequencies is difficult. Finally, we propose modifications to the setup and techniques to resolve noise versus frequency trends with the accuracy required to detect shot noise correlation.

4.1 Noise modeling in SiGe HBTs

To understand the mechanism of shot noise correlation, we must first understand how noise is modeled in SiGe HBTs. This section will briefly introduce cryogenic noise modeling in SiGe HBTs, highlighting only the relevant concepts and topics. A more detailed understanding of developing noise models of cryogenic SiGe HBTs can be found in Refs. [12, 51, 123].

Noise is a fundamental process in any real, electronic device that stems from two fundamental sources: the discrete nature of charges carriers (electrons or holes) and the thermal vibrations of these carriers due to operation at a finite temperature. The former mechanisms is known as shot noise and the latter is known as Johnson-Nyquist noise, or simply thermal noise.

Consider a constant flux of charge carriers flowing across a region. As the ensemble of charge carriers traverses this region, their arrival at the end of the region results in a current that is on average, constant. However, there are atomic level fluctuations in the arrival time of these carriers that result in microscopic fluctuations of the current about its average. These fluctuations in the current are referred to as shot noise current. The amplitude of these fluctuations is commonly captured in the frequency domain through a noise power spectral density, $S_{i,n}(f)$ or $S_{v,n}(f)$, which represents the mean square current or voltage fluctuations in a unit frequency bandwidth. For shot noise, the current power spectral density $S_{i,n}$ is given in units of $[A^2/Hz]$ [124]

$$S_{i,n}(f) = \frac{\langle i_n^2 \rangle}{\Delta f} = 2qI_{dev} \tag{4.1}$$

where f is the absolute value of frequency, q is the charge of the electron and I_{dev} is the mean device current about which the noise fluctuates. Similarly, the voltage power spectral density $S_{v,n}$ is given as a function of temperature from the Nyquist theorem as [124]

$$S_{v,n}(f) = \frac{\langle v_n^2 \rangle}{\Delta f} = 4kT_{phys}R \tag{4.2}$$

where k is the Boltzmann constant, T_{phys} is the physical temperature of the element at equilibrium, and R is the resistance of the dissipative element. From Eqs. 4.1 and 4.2 above, both shot noise and thermal noise are white noise sources, i.e. they are independent of frequency. In most microwave and RF devices including SiGe HBTs, some combination of these noise sources is used in conjuction with the small-signal model of the device to develop a noise model.

A commonly used noise model for cryogenic SiGe HBTs is shown in [3, Fig. 1], similar to what is used elsewhere in the literature. [5, 18, 125] Here, we use two shot noise sources to denote the noise associated with the two main terminal currents, I_B and I_C. We neglect the thermal noise sources associated with the emitter and collector resistances, and assume that the thermal noise due to the base resistance R_B dominates as it gets amplified across the transistor. [125] The equations for the spectral density for each of these noise sources in a SiGe HBT are given below under the assumption that the shot noise sources are uncorrelated [1, 125, 126]:

$$S_{ic} = \langle i_c^2 \rangle / \Delta f = 2qI_C \tag{4.3}$$

$$S_{ib} = \langle i_b^2 \rangle / \Delta f = 2qI_B \tag{4.4}$$

$$S_{vb} = \langle v_b^2 \rangle / \Delta f = 4kTr_B \tag{4.5}$$

where i_b, i_c, and v_b are the small-signal noise currents and voltage associated with each noise source. Moving forward we will assume that the noise currents and voltages are specified for a bandwidth of 1 Hz allowing us to drop the Δf term in the above equations.

At this stage, we have added elements that allow us to capture each of the individual noise amplitudes into the small-signal model, but we have not yet described how these individual elements affect the noise of the system as whole. The overall noise performance of a 2-port electron device can be captured using a system of four noise parameters. In general, the choice of these parameters varies based on the application, but following from the work in Ref. [13], we use the set consisting of the minimum noise temperature T_{min}, generator resistance R_n, optimum source admittance $Y_{opt} = G_{opt} + jB_{opt}$ where G_{opt} and B_{opt} are the optimum source conductance and susceptance respectively [1]. Using these four parameters, the input referred noise temperature T_n, is given by: [1, 123]

$$T_n = T_{min} + T_0 \frac{R_n}{G_S} |Y_S - Y_{opt}|^2 \tag{4.6}$$

where the reference temperature $T_0 = 290$ K, $Y_S = G_S + jB_S$ is the source admittance, and $Y_{opt} = Z_{opt}^{-1}$ is the optimum source admittance. Using the S-/Y-parameters obtained from the small-signal circuit model for the device, it is possible to derive equations for each of these noise parameters under various assumptions concerning the frequency and relative important of the circuit elements. Here we follow the representation given in Ref. [12], Eqs. (2.31)-(2.34).

The standard operating procedure to model the noise performance for a SiGe HBT involves developing small-signal model by fitting to measured S-parameters by extracting the values of the circuit elements at various biases using a procedure similar to that highlighted in Ref. [12]. This small-signal model is ported into a microwave simulation software such as AWR Microwave Office or ADS.

In this software model, the relevant noise sources and their magnitudes are added as shown in Fig. 4.1 for given bias conditions. The software then allows a calculation of the noise quantities of interest, such as T_{min} or T_{50} as functions of frequency. The noise model is verified by measuring these quantities on the device. It is almost always assumed in the noise model that the shot noise sources for i_b and i_c are uncorrelated, and the predictions of the model correspond to this assumption.

4.2 Theory and modeling of shot noise correlation

While assuming that the base and collector shot noise sources makes understanding and analytically solving for noise quantities relatively easier, this assumption is in-fact not correct. [2, 5, 125, 126] The collector current is constituted of electrons that are injected from the emitter to the base, over a potential barrier that is governed by the applied bias V_{BE}. The base current is constituted of holes that are injected from the base to the emitter, over a potential barrier that is also governed by the same bias voltage V_{BE}. Therefore, any small fluctuations in the base-emitter voltage v_{be} will result in correlated fluctuations of the base and collector currents, i_b and i_b, resulting in two correlated shot noise sources.

The observation that base and collector currents are correlated is not novel, and a simple model to study the effects of shot noise correlation has been developed in Ref. [125]. The model starts by considering the emitter and collector currents in the common-base mode as completely correlated due the electrons constituting both currents being the same. This correlation term is parametrized by a noise delay time τ_n

$$S_{ie,ic^*} = \langle i_e i_c^* \rangle = 2qI_C e^{j\omega\tau_n} \tag{4.7}$$

Then, this correlation model is converted from common-base mode to common-emitter mode as described in Ref. [125]. This results in an additional noise spectral density term along with the set in Eqs. 4.3 - 4.5 which accounts for the complex correlation between i_c and i_b, giving us the shot noise equations as:

$$S_{ib} = \langle i_b^2 \rangle = 2qI_B + 4qI_C Re[1 - e^{j\omega\tau_n}] \tag{4.8}$$

$$S_{ic} = \langle i_c^2 \rangle = 2qI_C \tag{4.9}$$

$$S_{ib^*,ic} = \langle i_b^* i_c \rangle = 2qI_C(e^{-j\omega\tau_n} - 1) \tag{4.10}$$

where $\omega = 2\pi f$ is the angular frequency and j is the complex imaginary number. It is clear that with a shot noise correlation delay term of zero, the above equations revert back to the uncorrelated assumption.

This model of shot-noise correlation leads to an important conclusion, that accounting for the correlation term can reduce the contribution of the collector shot noise, thereby reducing the overall noise contribution. This reduction in noise strongly dependent on frequency through the $\omega\tau_n$ term, indicating that at higher frequency, the difference between correlated and uncorrelated noise sources is expected to have a large impact on the noise parameters. It has been shown in the past that the predictions of this noise model are closer to the measured noise parameters at 300 K as a function of frequency up to $\sim$ 20 GHz. Specifically, the minimum noise figure NF_{min}, a precursor to the minimum noise temperature T_{min}, predicted using the correlation model is reduced relative to the predictions of the uncorrelated model, and aligns closely with the measured noise figure. [125, 126] The uncorrelated noise model was shown to overestimate the minimum noise figure more significantly at higher frequencies and at higher biases. [126] The predictions for other important noise parameters such as the optimum noise reflection coefficient Γ_{opt} are observed to also be shifted relative to those from an uncorrelated noise model. [125] This shift is important because the design of low-noise amplifiers (LNAs) using these transistors relies heavily on the knowledge of Z_{opt}. Owing to the difficulty of a direct measurement of Z_{opt}, device engineers rely on noise models that are able to provide a calculation of Z_{opt} to design low-noise amplifiers. Therefore, accurate modeling of the noise phenomena in these SiGe HBTs becomes of relevance, especially for applications with operating frequencies above 20 GHz.

Finally, while the effects of shot-noise correlation have been demonstrated in devices at 300 K as a function of bias and frequency, the temperature dependence of this phenomenon and the resulting impact on cryogenic noise performance remains unanswered. With SiGe HBTs becoming a promising

contender for cryogenic low-noise amplification in radio astronomy for high-frequency and SIS based receivers, [2] understanding the impact of shot noise correlation at cryogenic temperatures is paramount. In this vein, we aim to apply the shot-noise correlation model for room temperature devices into a cryogenic SiGe HBT model and simulate its impact on noise temperature versus frequency. Further, we aim to confirm the predictions of the correlation model by measuring noise temperature versus frequency at cryogenic temperatures and fitting the noise delay time parameter τ_n from this measurement. This knowledge of τ_n at different biases and temperatures can then be used to tease out the underlying physical mechanisms relating noise and electronic transport phenomena in cryogenic SiGe HBTs.

Cryogenic implementation of correlated shot noise in a SiGe HBT model

We start from an existing cryogenic SiGe HBT small-signal model in AWR Microwave Office (MWO) characterized near the low-noise bias point, provided by Bardin et al. and described in Ref. [18]. Fig. 4.1 depicts the small-signal model along with relevant noise sources implement in MWO. This simplified small signal model is developed for a common-emitter mode DC biasing scheme with collector current density $J_C = 0.5mA/\mu m^2$, a DC gain $\beta = 1300$, and a transconductance $g_m = 77mS/\mu m^2$ at a physical operating temperature of $T_{phys} = 7K$. A detailed description of the extraction procedures can be found in Ref. [18].

We now describe each of the element of the small signal model and its relevance moving from outside to inside. The outermost layer of the model contains the three series resistance associated with each of the three terminals; base resistance R_B, collector resistance R_C and emitter resistance R_E. Each of these resistances have associated temperature T_{phys} which is specified to account for the thermal noise generated at each of these terminals. Moving inwards, the model consists of three capacitive elements, the input or base-emitter capacitance C_{be}, the output or collector-substrate capacitance C_{cs} and the through or base-collector capacitance C_{bc}. Accurate knowledge of the values of these capacitances is critical as they largely govern the frequency dependence of the small-signal model and directly factor into the Y-parameters that translate the noise sources to the circuit level noise parameters. At the innermost layer, we have the conductance for base-emitter current $g_{be} = 1/r_{be}$ at the input, and

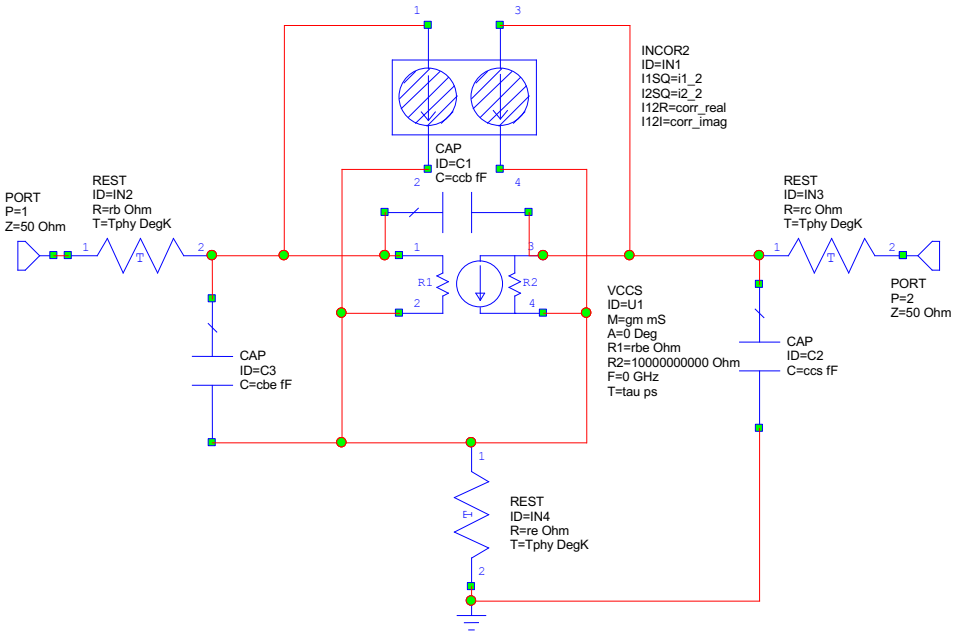

Figure 4.1: AWR Microwave Office implementation of a simplifed IHP SG13G2 SiGe HBT small-signal model for 4 – 20 K physical temperature. The two correlated current generators for base and collector shot noise are implemented through the INCOR2 element. Thermal noise is accounted for through the physical temperature specified through the resistive elements at each port. This model is used to generate predictions of T_{min}, T_{50} and other noise parameters.

a voltage-dependent current generator at the output with a transconductance g_m. The specification for the this current generator involves a load resistor in parallel $R2$; however, this value is set to an arbitrarily large value to make the dominant current path through the rest of the device. The delay time is specific as the electron transit time τ_e in ps. Finally, to complete the description of the noise model, we add the shot noise current generators associated with the base current I_B and collector current I_C. MWO allows for the implementation of a pair of correlated shot noise sources through the circuit element *INCOR2*. This element takes as inputs the mean square noise spectral power of each of the currents as i_1^2 and i_2^2. The values for these are given as in Eqs. 4.8 and 4.9 respectively. The correlation term is captured through the real and imaginary parts of the correlation coefficient ρ, given by

J_C	A_E	β	g_m	R_{BE}	R_B	C_{BE}	C_{BC}	C_{CS}
0.5	4.5	1300	76.7	20e+3	5.9	46.8	14.1	2.2

Table 4.1: Small-signal model parameters used with the MWO model for the IHP SG13G2 transistor. Units are in $J_C - mA/\mu m^2$, $A_E - \mu m^2$, $\beta - linear$, $g_m - ms/\mu m^2$, $R_{BE}, R_B - \Omega.\mu m^2$, $C_{BE}, C_{BC}, C_{CS} - fF/\mu m^2$.

$$\rho(f) = \frac{S_{ib*,ic}(f)}{\sqrt{S_{ib}S_{ic}}} \tag{4.11}$$

where the complex correlation term $S_{ib*,ic}$ is given by Eq. 4.10.

Specifying each of these device parameters completes the correlated noise model. It is common in semiconductor device small signal modeling to specify model parameters normalized to the emitter area A_E of the measured device, and it is assumed that these models can be scaled for devices of the same technology with different emitter areas. Following this convention, the parameters used in this model are provided in Table 4.1

Correlated vs uncorrelated noise predictions:

We now explore the effect of shot noise correlation on the predictions for the noise parameters across a range of frequencies. The model used here is for an IHP SG13G2 130-nm BiCMOS transistor device, with an emitter area of $4.5\mu m^2$ for a bias point of $0.5mA/\mu m^2$ at 4 K. The first quantity we predict is the dependence of the minimum noise temperature T_{min} as a function of frequency. For the correlated case, a noise transit time parameter of $\tau_n = 0.3ps$ was chosen corresponding to similar studies in the literature. [2] For the uncorrelated case, the noise transit time is set as zero.

Fig. 4.2 plots the minimum noise temperature T_{min} versus frequency across 1 - 30 GHz for both the correlated and uncorrelated case. Also plotted are the 50 Ohm input referred noise temperatures T_{50} for both the correlated and uncorrelated models. Plots are generated by MWO's solver for each of the noise parameters. As expected from the modeling done for room temperature correlation effects, accounting for correlation between base and collector shot noise lowers the value of T_{min}, and this reduction is more prevalent at higher frequencies. At 22 GHz for example, the difference reduction in T_{min} for a τ_n of 0.3 ps is nearly 1 K, from 3.8 K to 2.8 K.

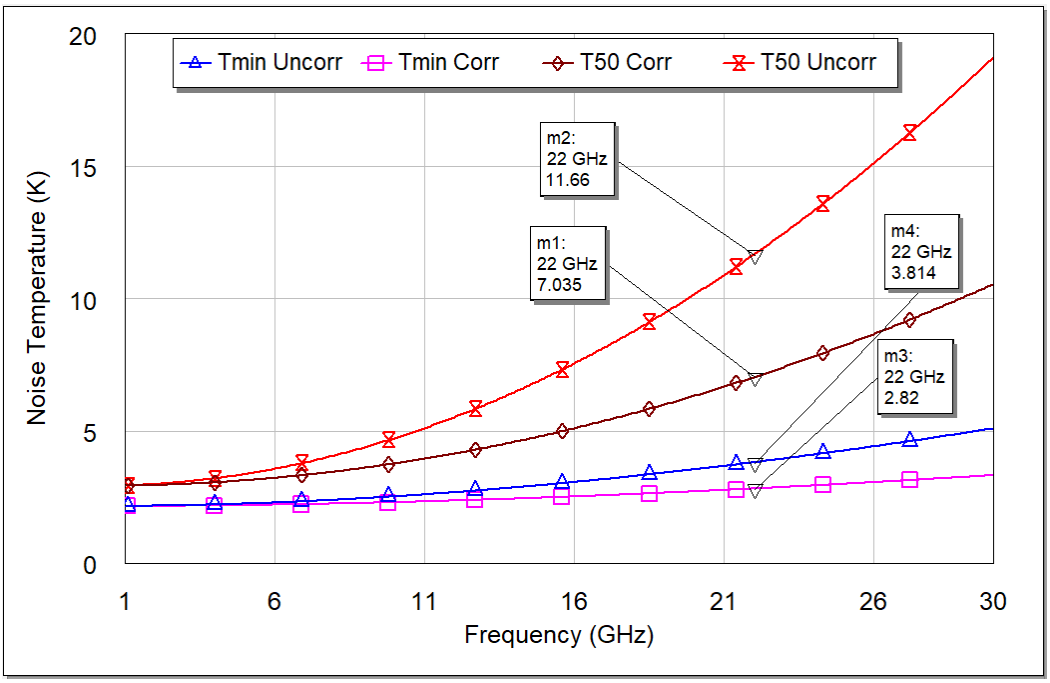

Figure 4.2: Model predictions of T_{min} vs frequency, and T_{50} versus frequency with the correlated (CORR) and uncorrelated (UNCORR) shot noise sources. While the difference in T_{min} with and without correlation is only $\sim$ 1 K at 22 GHz, the difference in T_{50} is $\sim$ 4.5 K making it easier to resolve through experiments.

Next we consider the change in the optimum input reflection coefficient Γ_{opt} due to correlation effects. Due to the interchangeability of reflection coefficient Γ and impedance Z, we will refer to them both as the optimum impedance Z_{opt}. Fig. 4.3 below plots the optimum impedance at 4 K for the correlated and uncorrelated models as function of frequency on a Smith chart. At first glance, it seems like both curves completely coincide with each other. However, at higher frequencies it becomes apparent that the value of Z_{opt} is shifted forward in frequency for the uncorrelated case relative to the correlated case. For this particular device at this bias point, the correlation results in a Z_{opt} that is closer to 50 Ohms than the uncorrelated model. This information is crucial for amplifier design, as the input matching network for the transistor is designed to transform a 50 Ohm line to an impedance as close to Z_{opt} as possible. Therefore, while designing amplifiers for applications at frequencies above 20 GHz, accurate knowledge of this noise parameter will directly impact the noise performance of the designed LNA.

The previous two plots illustrate the importance of modeling noise correla-

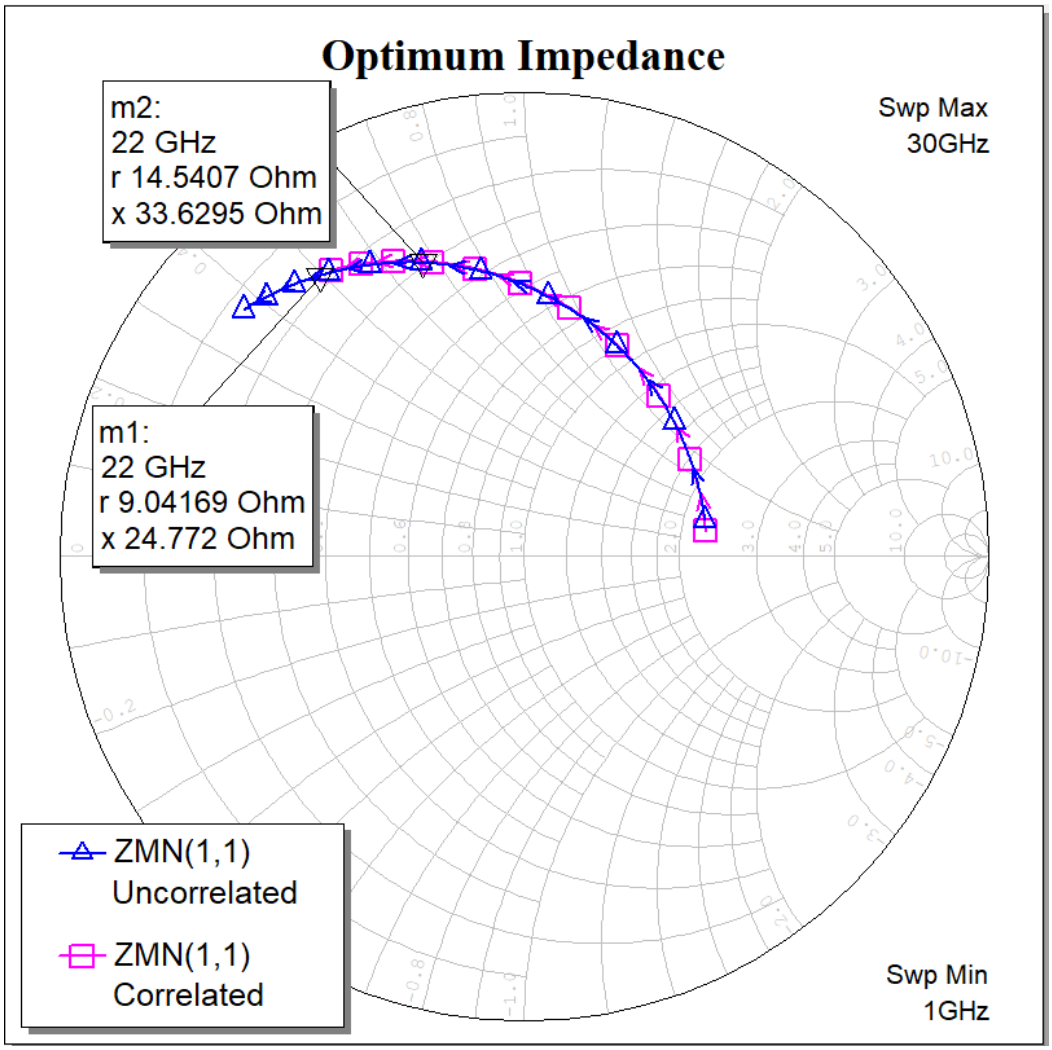

Figure 4.3: Modeled optimum generator impedance Z_{opt} (denoted ZMN in MWO) versus frequency on a Smith chart with and without correlation effects. It is seen that accounting for correlation provides a value of Z_{opt} that is shifted backwards in frequency.

tion so that the noise predictions of the model may be trusted. However, a direct measurement of the minimum noise temperature T_{min} of the transistor will already include the effects of correlation. In other words, the measured minimum noise temperature will always be the correlated noise temperature. While this is true, to measure the minimum noise temperature of the transistor, it must be provided with its optimum impedance Z_{opt} at the input. When an impedance tuner is not available to provide a large range of input impedances, MWO models are useful to provide an estimate of Z_{opt} required to achieve T_{min}. However, modeling the transistor without correlation provides a value of Z_{opt} different than the true optimum impedance. This will result in an error in the measured T_{min}. To illustrate this behavior, we simulate a pseudo-minimum noise temperature T_{min}^{pseudo}, defined as:

$$T_{min}^{pseudo} = T_{min}^{corr} + T_0 \frac{R_n}{G_s} |Y_s - Y_{opt}^{corr}|^2 \tag{4.12}$$

where the source admittance $Y_s = G_s + jB_s$ and optimum source admittance Y_{opt} are used instead of impedance, and T_{min}^{corr} is the true modeled minimum noise temperature with correlation effects. This quantity simulates the excess that is measured due to presentation of a source admittance $Y_s = Y_{opt}^{unccor} \neq Y_{opt}^{corr}$ that is different from the true optimum value. This results in a non-zero value for the second term in the above equation, therefore resulting in an assumed T_{min}^{pseudo} that is in fact greater than the true T_{min}^{corr}. As correlation effects dominate with increasing frequency, this difference in T_{min} becomes significant for transistors used in W-band applications up to 100 GHz. Fig. 4.4 plots the pseudo-minimum noise temperature T_{min}^{pseudo} versus frequency up to 100 GHz at 4 K, in comparison with the true T_{min}^{corr} and completely uncorrelated T_{min}^{uncorr}. The pseudo-minimum noise temperature is bounded at high frequencies by the completely uncorrelated and completely correlated predictions. At 80 GHz, the overestimation from the true T_{min}^{corr} to the measured T_{min}^{pseudo} is $\sim$ 3.3 K, which is a sizeable shift considering an absolute minimum noise temperature on the order of 10 K.

4.3 Measuring shot noise correlation through T_{50}

With the modeling of shot noise correlation at cryogenic temperatures complete, we would now like to extract the fitting parameter used in the models through experiments. To do this, we have a choice of measuring either T_{min}

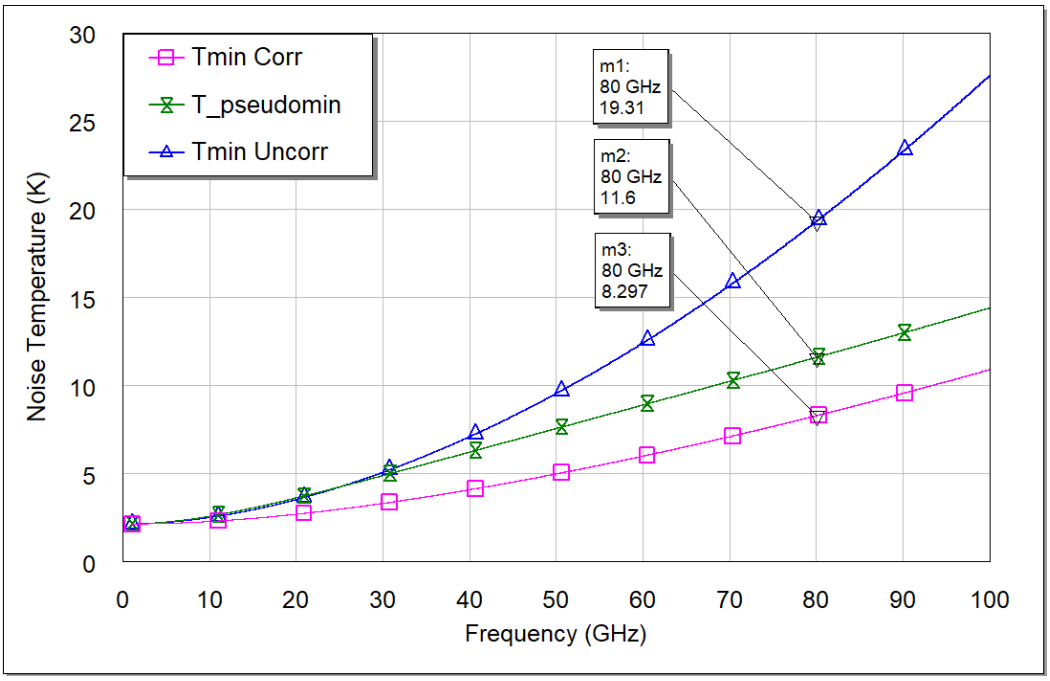

Figure 4.4: Modeled T_{min}^{pseudo} and T_{min} with and without correlation over a frequency extending into W-band. T_{min}^{pseudo} is bounded at higher frequencies by the correlated and uncorrelated predictions, and overestimates the minimum noise temperature value by $\sim$ 3.3 K compared to the true T_{min}.

vs frequency or T_{50} vs frequency. However, a measurement of Tmin requires apparatus that is able to present a wide range of impedances that cover the different regions of the Smith chart at the input of the device. While commercial impedance tuners are the common appartus of choice, they are expensive and less reliable at cryogenic temperatures than at room temperatures. Another clever way to tune the source impedance is through the development and use of a customized long-line module (LLM), as described in Ref. [13]. By using a combination of series and shunt transmission lines with carefully selected quarter wavelengths, the impedance presented at the output of the LLM can be looped around the Smith chart once every $\sim$500 MHz. Assuming that the optimum impedance of the transistor does not change appreciably within 0.5 GHz increments, measuring the noise temperature versus frequency within these 0.5 GHz buckets will provide input impedances that span the Smith chart. Therefore, through a least-squares fitting procedure common in microwave noise measurements, the noise parameters can be extracted for the center frequency of each of these 0.5 GHz buckets. [123]

This LLM method for noise parameter extraction has been used in the 4 - 8

GHz range at cryogenic temperatures. However, the design of such a module at higher frequencies poses many challengers. Primarily, the footprint of cables required to create the series and shunt transmission lines is on the order of tens of centimeters, which when used in conjunction with a noise source module occupies a large volume and thermal mass in the cryostat. Further, an LLM that spans higher frequencies would require modifications to the associated components such as noise sources, attenuators and microstrip lines which at high frequencies would result in greater measurement errors. Finally, the uncertainty budget of a T_{min} measurement is significantly lower than that of a T_e measurement, compounding the challenge of resolving correlation effects at frequencies around 20 GHz.

A workaround to measuring T_{min} is to measure T_e versus frequency at cryogenic temperatures. While this measurement will include changes to Z_{opt}, T_{min} and R_n due to correlation effects, fitting τ_n in the MWO model to match the predicted and measured T_e curves will still provide a preliminary confirmation of the presence of correlation effects. This measurement can be performed without an impedance tuner or an LLM by presenting the characteristic 50 Ohm impedance to the device-under-test (DUT), resulting in few loss components. More importantly, the cold probe station (CPS) setup described in Chapter 3 can easily be repurposed to probe the noise characteristics of the SiGe HBTs using the cold-attenuator method. [116]

Y-factor measurements using the cryogenic probe station:

Fig. 4.5 provides a schematic representation of the CPS in 'noise mode' using the cold attenuator Y-factor method. This measurement setup and procedure is described in detail in Ref. [116]. The overarching principle of this noise measurement method is to provide calibrated noise power to a device under test (DUT) at a fixed bias, measure the output noise power, and account for the noise contributions of the DUT by removing the calibrated noise contributions before and after the DUT. This is typically done by rapidly cycling a noise source between its ON state, where a large amount of noise power given by the excess noise ratio (ENR) is provided, and OFF state where the noise source radiates at ambient temperature $T_{cold} = T_0 = 290$ K. The relationship between the linear ENR and the ON state noise power is given by:

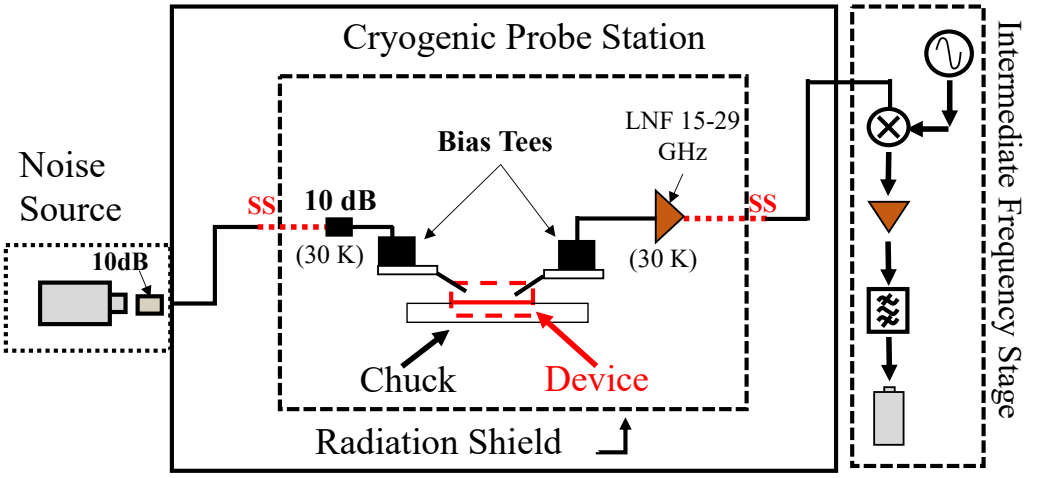

Figure 4.5: Schematic represenation of the custom-built cold probe station (CPS) in noise mode. The setup used here is the same as described in [116], with the exception of the pre-amplifer LNA being switched out for the LNF LNC15-29B with lower noise temperature between 15 – 29 GHz. Image credit: Bekari Gabritchidze

$$ENR_{lin} = \frac{T_{hot} - T_{cold}}{T_0} \tag{4.13}$$

For this measurement, we use a commercial smart noise source Keysight SNS N4002A with a nominal ENR of 15 dB and a frequency range from 10 MHz - 26.5 GHz, and maximum uncertainty around 18 GHz of ± 0.15 dB. The SNS is used at room temperature and a 10 dB attenuator is placed between the input of the probe station wall and the noise source to suppress mismatch to 50 Ohms. Coaxial cables with BeCu inner conductors, followed by stainless steel cables are used to translate from room temperature to the cold stage to balance flexibility and thermal leakage to the cold stage. Next, a cryogenic 10 dB attenuator is used prior to the DUT to suppress the uncertainty in noise power due to fluctuations in the ENR of the noise source. The advantage of using a cooled attenuator is that it contributes minimally to the noise power at the input, thus maintaining a large Y-factor while suppressing noise power uncertainty at the DUT input. [5, 12, 123] Finally, cryogenic bias tees are used to provide DC bias to the DUT terminals, which then connect to a commercial cryogenic probe (GGB industries, 40A-GSG-100-DP). The DUT is epoxied to a metal platform that is screw-mounted to the chuck with Indium foil between the two surfaces to reduce thermal resistance. The attenuator and both bias

tees are thermally strapped with braided copper wire to a coldfinger within the probe station to enhance thermal contact area.

At the output, we employ a commercial LNA as a pre-amplifier with low cryogenic noise temperature and high gain to minimize noise contributions of the backend chain. For this experiment, we chose an LNF LNC15-29B from Low Noise Factory, with an operating bandwidth of 15-29 GHz, nominal cryogenic noise temperature of 7 K and gain of 28 dB. Following the pre-amp, coaxial cables were used to connect bring the output back to room temperature power readout system. The power measurement system was custom-built using a mixer to convert from RF to intermediate frequency (IF), followed by three stages of room temperature amplifiers and filters to limit the IF bandwidth to 500 MHz. Finally, a Keysight U8481A power sensor is used to detect the amplified noise power in both on and off states to calculate Y-factor versus frequency.

The Y-factor in this measurement with all noise temperatures translated to the input plane of the DUT is given as:

$$Y_{DUT}(f) = \frac{T_{hot}G_{in} + T_{e,DUT} + T_{be}/G_{DUT}}{T_{cold}G_{in} + T_{e,DUT} + T_{be}/G_{DUT}} = \frac{T'_{hot} + T_{e,DUT} + T_{be}/G_{DUT}}{T'_{cold} + T_{e,DUT} + T_{be}/G_{DUT}} \tag{4.14}$$

where T_{hot} and T_{cold} are the ON and OFF state noise powers provided by the noise source respectively, which when translated to the input plane of the DUT using the gain of the input system G_{in} become $T'_{hot} = T_{hot}G_{in}$ and $T'_{cold} = T_{cold}G_{in}$. $T_{e,DUT}$ is the input referred noise temperature of the transistor, and G_{DUT} is the gain of the transistor. Finally, T_{be} is the noise temperature contributed by the backend chain, dominated by the noise of the pre-amplifier.

From Eq. 4.14 above, we see that to arrive at the DUT noise temperature $T_{e,DUT}$, calibration measurements of the noise contributions of the input chain and backend chain are required. Details of how these measurements are performed are given in Ref. [127]. For the input chain, the losses of the attenuators and cables along with their physical temperatures are carefully measured to develop an estimate of noise power propagated to the DUT input plane. With known T'_{hot} and T'_{cold}, a Y-factor measurement of the backend is performed by landing the probes on a THRU calibration substrate, giving us a calibrated backend noise T_{be} from:

$$Y_{be}(f) = \frac{T'_{hot} + T_{be}}{T'_{cold} + T_{be}} \tag{4.15}$$

It is impoprtant to note here that in the current measurement system, the backend calibration step is performed for each DUT measurement; however, the input calibration step is only performed once for a given input chain.

Finally, using the hot and cold noise powers recorded in the backend and DUT noise measurements the gain of the DUT can be extracted through:

$$P_{h,DUT} - P_{c,DUT} = kG_{DUT}G_{be}(T_{h,DUT} - T_{c,DUT}) \tag{4.16}$$

$$P_{h,be} - P_{c,be} = kG_{be}(T_{h,be} - T_{c,be}) \tag{4.17}$$

$$G_{DUT} = \frac{P_{h,DUT} - P_{c,DUT}}{P_{h,be} - P_{c,be}} \frac{T_{h,be} - T_{c,be}}{T_{h,DUT} - T_{c,DUT}} \tag{4.18}$$

where $P_{h,DUT}$ etc. are the noise powers measured during hot and cold states for the DUT and backend measurements, and $T_{h,DUT}$ etc. are the calibrated noise temperatures at the input plane of the DUT or backend chain in each of the measurements.

Noise measurement results for cryogenic SiGe HBTs

We now present the results of the above described measurements for an IHP SG13G2 130nm process device using the probe station. The devices used for the measurements were different than the ones used in the modeling of shot noise, in that emitter area for the measured devices is $A_e = 1\mu m^2$ instead of $4.5\mu m^2$ for the modeled devices. The reason for this change is that the devices available to us with the same emitter area as the model had contact pads that were non-standard in pitch and too narrow to be probed using the $100\mu m$ pitch GSG probes in the CPS. However, since SiGe HBT models are specified with parameters normalized to the area, the model remains valid with only small modifications to the parameters. The primary change is to the collector current using the low-noise bias point, specified as $J_C = 0.5$ mA/μm^2 [18], which for a device with emitter area $A_E = 1\mu$m^2 is $I_C = 0.5$ mA.

Fig. 4.6 plots the measured T_{50} versus frequency for three trials with a collector current $I_C = 0.5$ mA between 15 - 18 GHz. A secondary bias point of $I_C = 2.5mA$ is also tested to compare gain and noise temperature differences.

Fig. 4.7 plots the measured gain versus frequency at both collector current biases.

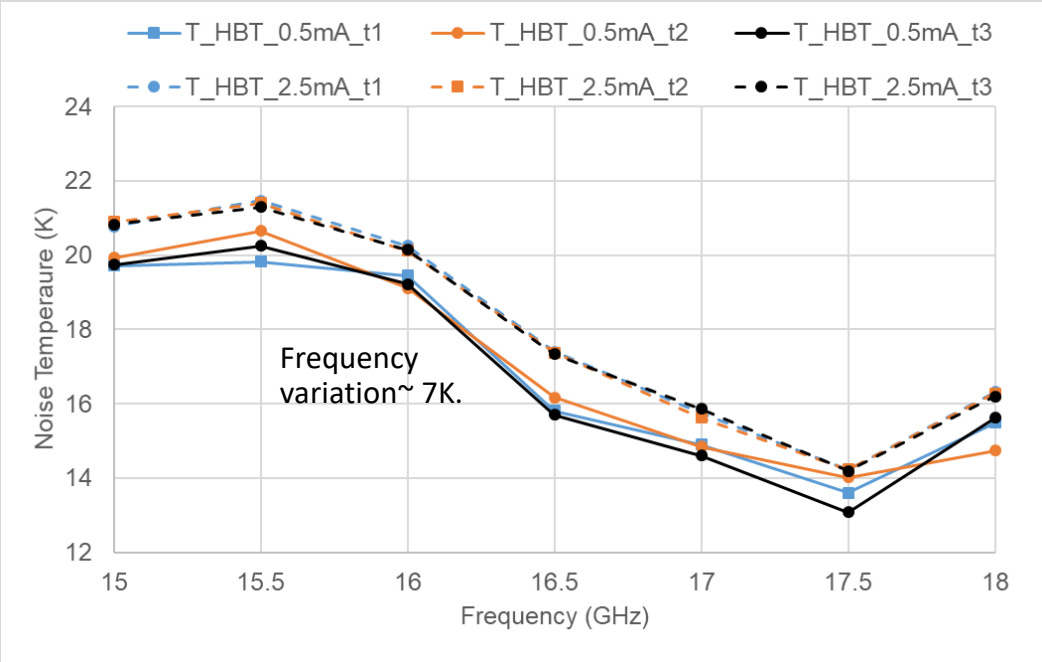

Figure 4.6: Three sweeps of the measured T_{50} versus frequency of the HBT device across both bias points, $I_C = 0.5mA$ and $I_C = 2.5mA$. The noise temperature measurements are repeatable within 1 K for $I_C = 0.5mA$ and lower for $I_C = 2.5mA$. The profile of the noise temperature displays a non-monotonic frequency dependence that is not expected from the model.

The measured T_{50} show a large frequency profile within the bandwidth of measurement across all trials of measurement. The noise temperature swings between 13 K to 20 K, and the decreasing trend with frequency is uncharacteristic of the physical noise behavior of any transistor. In comparison with the modeled noise temperature using an MWO model with the small-signal parameters adjusted for the new emitter area, we see from Fig. 4.8 that the modeled T_{50} does not predict the same trend between 15 - 17 GHz as seen in the measurement. While the absolute value of measured T_{50} is similar to the model around 17 GHz, the non-monotonic frequency trend in measurements is the opposite of what is seen in model predictions. More importantly, the difference in correlated and uncorrelated noise temperature predictions from the modified MWO model at 17 GHz is only $\sim$ 1 K. The frequency-dependent variation in noise temperature of 7 K in the measurements at both $I_C = 0.5mA$ and $I_C = 2.5mA$ makes detection of this noise temperature difference due to correlation effects unresolvable.

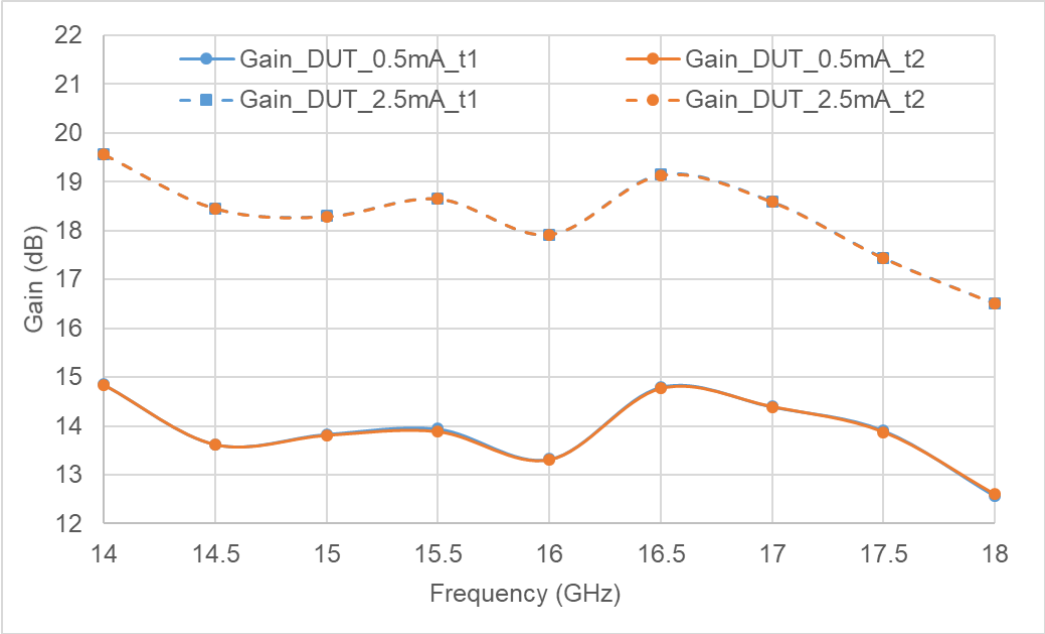

Figure 4.7: Gain extracted from Y-factor measurements for the I_C bias points. The gain increases substantially from $\sim$ 14 dB to $\sim$ 19 dB between $I_C = 0.5$ mA to 2.5 mA. The additional gain at the higher bias point provides a reduced backend noise temperature T_{be} being translated back to the DUT input plane.

We note here that the repeatability of the noise measurements is on the order of $\sim$ 1 - 2 K, even at the lower bias point with lower DUT gain. Comparison of the T_{50} results between the two bias points in Fig. 4.6 indicates a small improvement in the repeatability in noise temperature at the higher bias point. This is due to the increase in DUT gain from $\sim$ 14 dB to $\sim$ 19 dB as shown in Fig. 4.7, which in turn reduces the uncertainty contributions of the backend noise components ΔT_{be}. However, the same trend with frequency is observed at both biases indicating that the repeatability of device data is likely not the source of the error. The origin of these anomalous frequency trends will now be explored. In the next section, we will discuss in detail an analysis of the potential sources of error that prevent us from resolving trends in noise temperature to decipher noise correlation.

4.4 Sources of error and future recommendations

The magnitude of variation in noise temperature with frequency on the order of 7 K in the measurement of T_{50} in Fig. 4.6 indicates a significant source of uncertainty in the measurement system that prevents resolution of correlation effects. This uncertainty could originate from three main sources: (a) faulty

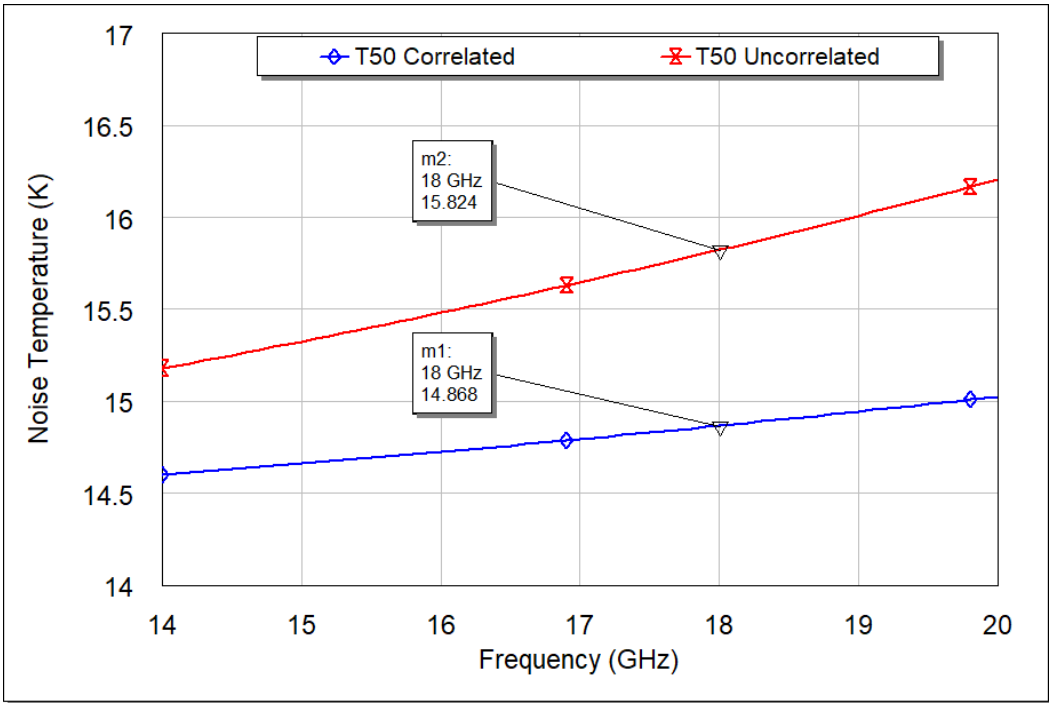

Figure 4.8: Modeled T_{50} for the correlated and uncorrelated device model modified for an $A_e = 1\mu m^2$ across the frequency range of the experimental measurement. With a smaller emitter area device, the absolute values of the currents are lower, resulting in lower absolute noise temperatures. Further, with the limitations of the measurement setup, the highest reliable frequency for the measurement is shifted down to 18 GHz. Both of these factors lower the resolvable difference between the correlation and uncorrelated assumptions to ~ 1 K.

device behavior, (b) backend component frequency profile, or (c) pre-DUT component frequency profile. We will address each of these possible sources through individual identification experiments.

First, we address the possibility of noise frequency profile originating from the SiGe HBTs not performing as expected by testing the presence of the frequency trends on a secondary IHP HBT and a HEMT device. Fig. 4.9 plots T_{50} versus frequency at 20 K and a bias of $I_C = 0.5mA$ for the SiGe HBT, and an $I_{ds} = 10mA$ for the HEMT device. The HEMT devices used here are the same as those described in Ref. [127]. We see from the measurement of T_{50} on the secondary HBT that the frequency profile non-monotonicity is present in both devices. Further, the noise temperature data for the HEMT device shows a similar non-monotonicity and frequency profile, although suppressed and shifted lower due to its superior noise performance. Finally, based on the

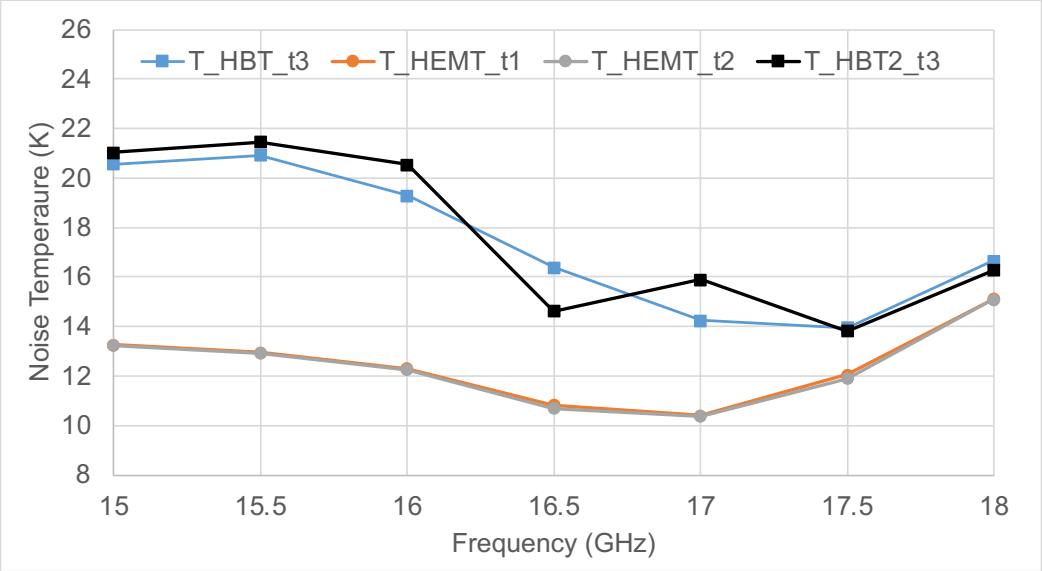

Figure 4.9: Measured T_{50} versus frequency for two different HBTs and one HEMT device. The frequency profile is quantitatively similar for both HBTs, indicating the devices themselves are not faulty. The HEMT demonstrates a qualitatively similar frequency profile as the HBTs, with an absolute noise temperature lower than HEMTs due to a superior noise performance. This implies that the non-monotonic frequency trend is not device specific and originates from the experimental setup.

bias dependent gain increase seen in the SiGe HBT from Fig. 4.7 earlier, the measured HBT's response to DC stimulus seems to be as expected. These data indicate that faulty device behavior is not the cause of the anomalous noise temperature profile.

Next, we consider the effects of backend noise temperature and it's frequency profile on the extraction of DUT noise. It is possible that with a low enough DUT gain, the effects of the backend components are detectable at the DUT input plane. Further, the difference in the impedance match at the backend input plane between the calibration step and device measurement step cannot be accounted for with the current measurement setup. Therefore, any frequency dependent behavior of the backend chain is not accurately carried into the calibration step. We can make conclusions about the impact of the backend chain by looking closely at the backend noise temperature in comparison to the DUT noise temperature.

Fig. 4.10 plots the backend noise temperature T_{be}, the DUT noise temperature T_{DUT} and the system noise temperature T_{sys}, defined as:

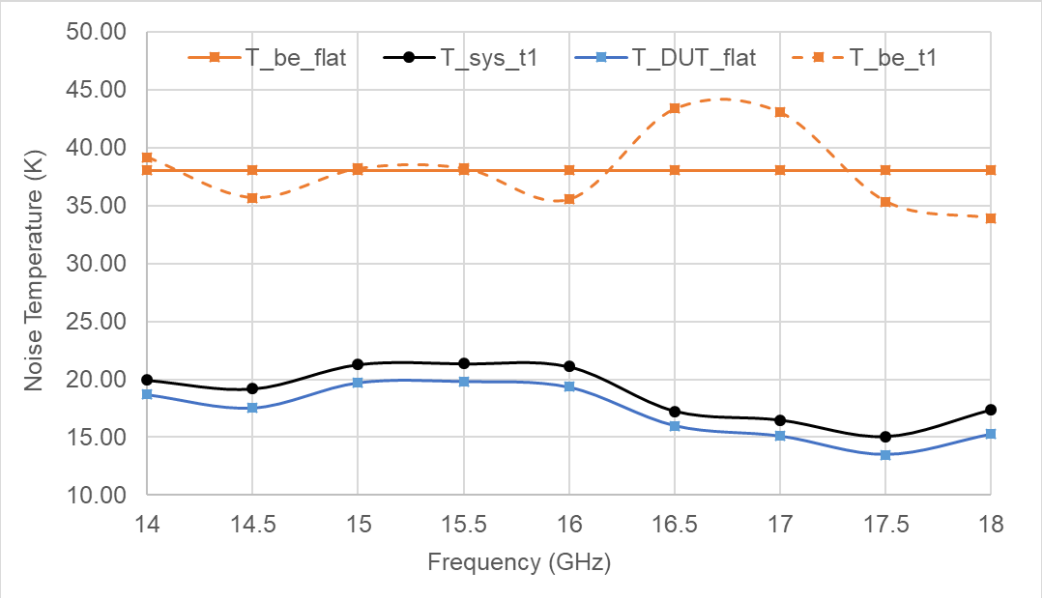

Figure 4.10: Measured noise temperature versus frequency for the backend T_{be}, DUT T_{DUT} and system noise T_{sys}. Also plotted is the mean T_{be} value across the frequency range, T_{be}^{flat} that is used to test the backend frequency profile contribution to the DUT noise. The frequency profile of the backend is different compared to that of the DUT and system noise, indicating the non-monotonicity observed in T_{DUT} does not originate from the backend components.

$$T_{sys}(f) = T_{DUT}(f) + \frac{T_{be}(f)}{G_{DUT}} \tag{4.19}$$

The backend noise temperature is extracted from the Y-factor of the THRU structure using Eq. 4.15. The system noise temperature is used to capture the cumulative behavior of the DUT and the backend from which the value of T_{DUT} is extracted. The curve for T_{be} versus frequency demonstrates a large but different frequency profile than what is observed for T_{DUT} in Fig. 4.6. Further, while the LNF pre-amplifier LNA with $T_e \approx 7$ K is expected to dominate the backend noise temperature, we see that the value of the noise temperature is closer to 40 K. This is likely due to the noise contributions of a 3 dB cryogenic attenuator at the input of the LNF LNA to supress mismatch, and the losses associated with the probes and cryogenic bias-tees. However, the similarity between T_{sys} and T_{DUT} frequency profiles indicates that any frequency content from T_{be} is sufficiently suppressed through G_{DUT}. The primary difference between the two curves is an offset due to $T_{be}(f)/G_{DUT}$ which, due to the sufficient gain in the DUT, results in a similar frequency dependent trend in

the noise temperature profile in both curves. Strictly speaking the gain of the DUT may also have a frequency dependence but for the narrow bandwidth used here, a large shift in gain with frequency is not seen as shown in Fig. 4.7.

To further confirm that the backend chain noise contributions do not significantly impact the frequency dependence of noise at the DUT input plane, we artificially flatten the $T_{be}(f)$ to its average value. This is shown as the dotted line Fig. 4.10. Even with no frequency content in the backend noise profile, the non-monotonicity of T_{sys} and T_{DUT} remains. Therefore, we can conclude that the backend components are not responsible for the non-monotonic frequency profile at the DUT input plane.

Sources of uncertainty in the pre-DUT component chain

Now that we have concluded that both faulty device behavior as well as contributions from the backend noise components cannot be responsible for uncertainty in the frequency-dependent noise temperature of the DUTs, we look to the components prior to the DUT.

The losses, physical temperatures, and therefore noise contributions of pre-DUT components are known to set the uncertainty limit of any noise measurement setup. [12] The key contributor of noise uncertainty among the pre-DUT components is in fact the smart noise source (SNS) itself, with ENR uncertainties on the order of $\pm 0.2dB$ for the Keysight N4002A. [128] Specifically, the fluctuations in the ON state noise power can contribute a large amount of uncertainty to the known noise power being provided to the DUT. This is an important reason for the development of the cold attenuator method of Y-factor measurements. [12] Despite the use of a 10 dB cooled attenuator in our measurement setup, it is likely that uncertainty originating from the T_{hot} of the noise source and propagating to the DUT is still relevant.

A simple heuristic to assess the importance of this effect is to artificially alter the calibrated ON state noise power provided to the input of the DUT, T'_{hot} and observe how the extracted T_{DUT} changes in response. Fig. 4.11 plots the measured, uncorrected T_{DUT} versus frequency, along with a corrected T_{DUT} in which a manual correction factor to T'_{hot} has been applied to generate a mostly flat noise profile. A list displaying the correction offset to T'_{hot} along with their percentage changes is also displayed. It is important to note here that this artificial frequency trend of noise temperature need not be the true frequency

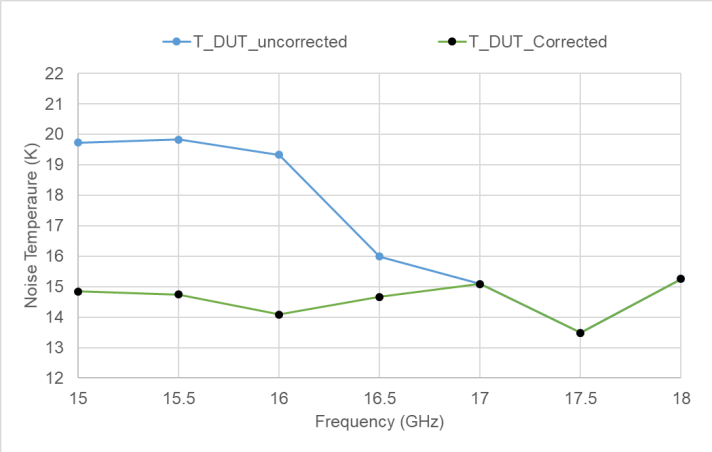

T'_{hot} (K)	Correction (K)	% Correction
108.794	4.000	3.546
106.962	4.000	3.605
105.172	4.000	3.664
102.732	4.000	3.748
100.377	4.000	3.832
100.340	1.000	0.987
98.450	0.000	0.000
96.463	0.000	0.000
94.537	0.000	0.000

Figure 4.11: Measured noise temperature of the DUT $T_{DUT}^{uncorrected}$ and the corrected noise temperature $T_{DUT}^{corrected}$ versus frequency. The correction is applied to T'_{hot} at the input plane of the DUT to estimate the offset required to provide a flatter T_{DUT} frequency profile at the lower end of the frequency spectrum.

profile, but rather is meant to qualitatively resemble model predictions.

We see that a rather small offset in T'_{hot} of 4 K is enough to correct the 7 K frequency swing between 15 - 17 GHz and bring the noise temperature curve to within the uncertainty bounds of the measurement system. To understand the source of this offset, we must first model the uncertainty in T'_{hot} due to the ENR uncertainty and the uncertainty of the losses prior to the DUT.

Modeling the uncertainty in T_{hot}

Using Eq. 4.4, we can translate the uncertainty in ENR to an uncertainty in T_{hot} at the output of the shot noise source by taking the appropriate partial differential. It is important to note here the uncertainty in ENR that is specified in dB cannot be directly converted into linear scale; instead the ENR must be expressed in dB as a function of T_{hot} as follows:

$$ENR_{dB} = 10log_{10}(ENR_{lin}) = 10log_{10}\left(\frac{T_{hot} - T_0}{T_0}\right) \tag{4.20}$$

where we have used the fact that $T_{cold} = T_0$. Now, rearranging for T_{hot} and differentiating with respect to ENR_{dB} gives us the uncertainty ΔT_{hot} at the output plane of the noise source:

$$\Delta T_{hot} = \frac{\partial T_{hot}}{\partial ENR_{dB}} = T_0(\frac{10^{ENR_{dB}/10}}{10})\Delta ENR_{dB} \tag{4.21}$$

where ΔENR_{dB} is the specified uncertainty in the ENR of the noise source. For a noise source with a nominal ENR of 15 dB ($T_{hot} \sim 10345$ K) and an uncertainty of ± 0.15 dB at 18 GHz, we calculate a value of ΔT_{hot} at the output plane of the noise source as 150.83 K.

This uncertainty must now be propagated through the dominant lossy components of the pre-DUT input chain, and the noise contributions of these lossy components must be factored in. As example, we calculate the noise power at the output of the 300 K 10 dB attenuator $T_{tot,A}$, referred to here as attenuator A, as well as the propagated uncertainty at the output of the attenuator. Here, we use the terms noise power and noise temperature interchangeably as they are related to each other through the Boltzmann constant k_B and the bandwidth, which are both constants.

$$T_{tot,A} = T_{hot}G_A + T_{n,A} \tag{4.22}$$

In the equation above, $T_{tot,A}$ is the total noise temperature at the output of attenuator A, G_A is the linear gain of the attenuator, and $T_{n,A}$ is the noise temperature contributed by the attenuator given by $T_{n,A} = T_{phys}(1 - G_A)$. Here, T_{phys} is the physical temperature of the attenuator which is recorded using a calibrated temperature sensor. Next, the total uncertainty at the output of attenuator A $\Delta T_{tot,A}$ is calculated as:

$$\Delta T_{tot,A} = \sqrt{(\Delta T_{hot}G_A)^2 + (T_{hot}\Delta G_A)^2 + \Delta T_{n,A}^2} \tag{4.23}$$

where ΔG_A is the uncertainty in the gain measurement of the attenuator and $\Delta T_{n,A}$ is the uncertainty in the noise temperature of the attenuator. For this analysis, $T_{n,A}$ is assumed to be negligible due to the large loss value of the attenuator and the accuracy of the calibrated DT-670 temperature sensors. The calculated value of this uncertainty is ~ 0.5 K, relative to the uncertainty values ~ 10 K propagated through T_{hot}. The uncertainty ΔG_A is limited by the calibration of the VNA used to measure the losses, which is assumed to be ± 0.1 dB, a typical value at frequencies near 18 GHz. Using this information,

Stage	**SNS out**	**Att A**	**Att B**	**BT + Probe**
$T_{n,tot}$ (K)	10345.37	1336.25	169.52	141.93
Δ ENR/G (dB)	0.15	0.10	0.10	0.10
Propagated $\Delta T_{n,tot}$ (K)	150.83	18.93	2.44	1.97
$\Delta T_{n,loss}$ (K)	–	0.31	0.03	0.24

Table 4.2: Calculated values for propagated noise powers at each stage (first row), uncertainty associated with key components of each stage (second row), propagated unceratinty contributions at each stage (third row), and noise contributions of lossy components (last row).

the total uncertainty in noise temperature propagated to the output of the 10 dB attenuator is calculated as $\pm$18.93 K, and the total propagated noise temperature is 1336.25 K. The analysis progresses in a similar way for the remaining components of the input chain, of which the losses associated with the cryogenic 10 dB attenuator, denoted B, and the bias-tee and probe are considered the dominant ones. Table 4.2 displays the propagated noise powers and associated uncertainties at each stage of the input chain leading up the probe.

As mentioned above, the last row of the above table demonstrates that the noise temperatures of the lossy components themselves are minimal, barring the loss of the probe and bias-tee which has been accounted for. As a result of this uncertainty analysis, we see that the total uncertainty in ON state noise power $\Delta T'_{hot}$ propagated to the input plane of the DUT is $\pm$2.21 K. Recall that the correction required due to uncertainty in T'_{hot} is on the order of $\pm$4 K. This indicates that while the uncertainty in the noise measurement due to T_{hot} is relative large, it is still not adequate to completely predict the frequency shift observed in T_{DUT}.

Finally, we consider the possibility that changes in reflection coefficients between the various connectors in the input chain may result in some frequency content of T_{DUT} that is not accounted for during the individual characterization of the cables and attenuators. As mentioned previously, the losses and physical temperatures of each component prior to the DUT were measured in a cryostat using a VNA as a function of temperature. These losses and associated temperatures were then used to account for the pre-DUT noise contributions. However, a measurement of the noise as a function of frequency once all the individual connections are assembled is not made.

Measuring the noise power at the end of the input chain may seem straightforward and similar to how the backend noise temperature is characterized. However, recall that the backend noise is calibrated using a Y-factor method that depends on knowledge of the noise power at the input plane of the THRU substrate. In other words, either the pre-DUT noise or the backend noise must be known to accurately characterize the other. Instead, as a heuristic to determine whether reflections in the input chain could explain the 4 K correction required to flatted the measured T_{DUT}, we calculate the magnitude of the reflection coefficient Γ_{in} at any one interconnection that results in the desired T'_{hot} correction.

The power input to the device P_{in} is a function of the power available from the source $P_{av,s}$ and the reflected power P_{ref}

$$P_{in} = P_{av,s} - P_{ref} = P_{av,s}(1 - |\Gamma_{in}|^2) \tag{4.24}$$

where we have used the relation between reflected and available power $P_{ref} = P_{av,s}|\Gamma_{in}|^2$. Then, the corrected power provided to the input of the DUT is given as:

$$T'_{hot,corrected} = T'_{hot}(1 - |\Gamma_{in}|^2) \tag{4.25}$$

where $T'_{hot,corrected}$ is the actual noise power that is provided to the input plane of the DUT after accounting for any mismatch due to Γ_{in}. Using the same correction offsets to T'_{hot} as shown in Fig. 4.11 and assuming that a correction value of 0 K corresponds to a mismatch magnitude of -20 dB, we plot the change in $|\Gamma_{in}|^2 = |S_{11}|^2$ required to correct T'_{hot} in Fig. 4.12.

We see that an S_{11} magnitude shift between -15 dB to -20 dB is adequate to explain the shift in T'_{hot} that will result in the frequency profile observed in T_{DUT}. This level of mismatch to 50 Ohms represents very offsets in S_{11} that are on the order of the uncertainty bounds of the measurement, and can be the result of small variations at any of the interconnections along the input chain. Each of these connections, which are nominally ideal 50 Ohm connections up to 18 GHz, may result in a small mismatch if not made correctly. Further, each time modifications to the setup are made, the mismatch change will result in a slightly different frequency profile than previously observed.

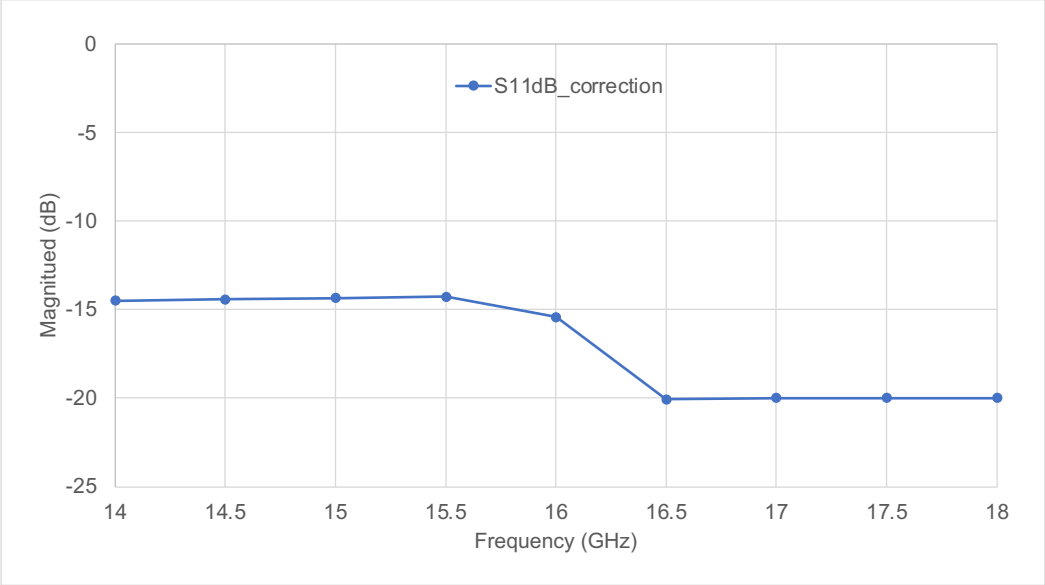

Figure 4.12: Calculated magnitude of the input reflection coefficient $|S_{11}|^2$ that are able to provide an offset in T'_{hot} that can predict the frequency dependent uncertainty in T_{DUT}. A relatively small mismatch change from -20 dB to -15 dB at the lower-end of the frequency spectrum is sufficient to result in an uncertainty in T_{DUT} on the order of 7 K.

Finally, the possibility of standing waves is also not ruled out which could result in reflection coefficients of this magnitude. Therefore, a detailed study of the frequency-dependent noise of the input chain must be carried out *in-situ*, once all components are assembled. Otherwise, to improve the repeatability and accuracy of the measurement, the transistor can be packaged for coaxial measurements in a cryostat, thus reducing the total length and connections required at the input chain. In the next section, we discuss the possibilities of such a measurement.

4.5 Modifications to experimental techniques

Here, we suggest some modifications to the experimental approach that will provide better resolution for shot-noise correlation effects.

First, to reduce the frequency-dependent systematic uncertainty in the cold probe station, an accurate method to characterize the noise contributions of the input chain before each DUT noise measurement must be developed. As mentioned earlier, a calibration step for either the pre-DUT or backend chain is required to then accurately characterize the remaining system. Measuring the noise of a temperature-controlled 50 Ω load using the backend chain can

act serve as a calibration method. The noise power output by a resistive load at a given physical temperature is $kT_{phys}\Delta B$ within a frequency bandwidth ΔB. By measuring the total noise power at the output of backend chain for a known input 50 Ω noise power, the noise contributions of the backend can be calculated. Once the backend noise is accurately known, the input chain noise can be measured *in situ* to characterize its frequency dependence when fully assembled. However, the sensitivity to noise fluctuations due to reflection coefficients will remain and the limitations on the probe stations frequency range will keep the required noise resolution close to $\sim 1 - 2$ K.

Another alternative method to perform this measurement is to package the transistor with an appropriate bias-tee input network, that allows it be measured in a smaller form factor. The packaged fixture can be measured using shorter coaxial cables with fewer interconnects, in a smaller cryostat than the CPS. Further, the measurement can then be performed at frequencies closer to 30 GHz that provide a larger sensitivity budget to distinguish between the modeled correlated and uncorrelated predictions. The frequency limits in this method would primarily arise from the choice of coaxial cable, and the availability of a noise source with sufficient ENR at the measurement frequency. Fig. 4.13 depicts preliminary packaged fixtures and the layout within that were designed to be measured in a small 6 K cryostat with coaxial cables as described above.

The fixtures were tested against an MWO model that included the displayed input and output bias-tee networks. However, it was found that the gain of the device was well below the modeled values, with negative dB of gain above 18 GHz. Therefore, a noise measurement of the structures was not possible as the transistors was found to not be operating as predicted. Nevertheless, future iterations of packaged fixtures with transistors operating as expected will likely allow for more accurate noise measurements to establish the effect of shot noise correlation in SiGe HBTs.

4.6 Summary

We have established in this chapter the importance of shot-noise correlation effects by implementing a model for correlated noise that uses a noise transit time as its parameter. The effect of correlation on the modeled T_{min}, T_{50} and Z_{opt} predicts a reduction in anticipated noise performance and a frequency

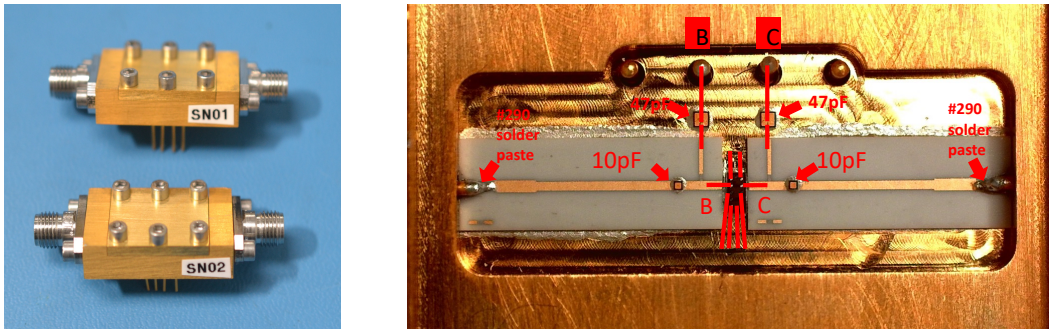

(a) (b)

Figure 4.13: Pictures of (a) packaged device fixtures to measure shot noise correlation effects, and (b) layout of assembled fixture with the DUT at the center and input and output bias networks built-in. The four pins at the top of the structure are used to provide base and collector bias, while the emitter is grounded through the chassis. The substrates with transmission lines were custom-designed for the chassis, translated to K-connectors for the RF terminals.

shift in the optimum impedance required to noise-match the transistor. We then detailed an experimental approach to verify the impact of shot noise correlation and extract the noise transit time parameter τ_n by measuring discrete transistors on a custom-built probe station. The resulting experimental data contains an uncharacteristic frequency profile that precludes a determination of the expected T_{50} trends with and without correlation effects. Further analysis towards the identifying the source of the error indicates the presence of frequency dependent systematic errors originating from the input chain of the setup. Specifically, the large number of interconnects and coaxial cable lengths result in shifts in reflection coefficients that offset that noise power provided to the DUT. Accurate knowledge of this noise power is critical towards reducing the uncertainty of the noise measurement setup. Therefore, a new measurement technique using a packaged device fixture with reduced input cable length and connections is suggested. Preliminary experiments of a packaged fixture provided no significant results due to uncharacteristic device behavior, but future iterations with carefully designed bias networks and probed devices will allow for detection of shot noise correlation mechanisms.

Chapter 5

CONCLUSIONS AND OUTLOOK

The work described in this thesis has aimed to address the long-standing observations of cryogenic non-ideal IV characteristics of SiGe HBTs. This anomalous cryogenic behavior directly limits the associated DC, RF and microwave noise performance. Therefore, understanding the physical mechanisms responsible for these anomalies is crucial to enabling the full potential of SiGe HBTs as LNAs in cryogenic applications that have large-scale amplification requirements.

In Chapter 2, we have studied quasiballistic transport in SiGe HBTs using an exact, semi-analytic solution to the Boltzmann equation based on an asymptotic expansion method. We report that the predictions of IV characteristics including quasiballistic transport are inconsistent with experiment. Specifically, our calculations predict collector currents smaller than the measured currents for a given base-emitter voltage and a temperature dependence of transconductance close to ideal, both of which contradict experimental observations. We suggest that local fluctuations in the base-emitter barrier height could account for the non-ideal IV behavior. In Chapter 3, we have reported measurements of the built-in potential of the base-emitter junction and its temperature dependence of a SiGe HBT using IV and CV characteristics. The differing values of the built-in potential at cryogenic temperatures obtained from these two methods supports the origin of cryogenic electrical anomalies as arising from spatial inhomogeneities in the base-emitter junction potential. The physical origin of these barrier inhomogeneities is hypothesized to be Ge clusters or C impurities. Finally, in Chapter 4 we have established the importance of shot-noise correlation effects by implementing a model for correlated noise that predicts a reduction in anticipated noise performance and a frequency shift in the optimum impedance required to noise-match the transistor. We detailed an experimental approach to verify the impact of shot noise correlation and extract the noise transit time parameter τ_n. The resulting experimental data contains an uncharacteristic frequency profile, making a determination of shot noise correlation effects from T_{50} trends inconclusive. In this chapter, we discuss possible avenues for future research that arise from

the work that reported here thus far.

BEEM measurements to probe spatial inhomogeneities in custom-grown SiGe structures

We have already touched upon the fact that certain spectroscopic techniques may be useful in directly probing and verifying the presence of spatial inhomogeneities at the Si:SiGe heterojunction between the emitter and base. Techniques such as ballistic electron emission spectroscopy (BEEM) have been used to probe potential barrier heights at a lateral resolution on the nanometer length scales. [70, 121] This technique relies on injecting electrons from the tip of a scanning tunneling miscroscope (STM) with an energy governing by the tunneling voltage V_T. The interface to be probed is deposited with a metallic film with thickness on the order of a few nanometers. A fraction of the injected electrons for a given energy traverse the metallic film ballistically, i.e. without any scattering events, and reach the interface to be probed at approximately the same energy as at the injection qV_T. If the local potential barrier height at the interface is lower in energy than the energy of the eletrons, the charge passes the barrier resulting in a collector current. Therefore, an IV sweep between the BEEM collector current I_{BEEM} and the applied tunneling voltage V_T provides a threshold voltage for the current flow corresponding to the local potential barrier height $\Phi_{BI}(x)$. IV sweeps of lateral scans across the interface width x can then provide a spatially variant potential barrier height.

The BEEM technique has been used to directly probe variations in Schottky barrier height of metal-semiconductor interfaces with Co clusters. [121] Figure 5.1 is adapted from [121] to demonstrate the end result of a BEEM characterization of the Au/Co/GaAs metal-semiconductor junction. The samples in the reference work were prepared using discontinuous Co films and continuous Au films, resulting in Co clusters on the order of 5 nm wide at the Schottky interface. From Fig. 5.1 we see that these Co clusters result in a reduction of Schottky barrier height by $\sim$ 100 meV that is detectable through the BEEM measurement.

We propose that a similar BEEM measurement of a Si:SiGe heterojunction representing the base-emitter junction of an HBT will provide further evidence on the presence of spatial inhomogeneities in the SiGe alloy. Si:SiGe structures grown with Ge doping concentrations of ranging from 10% – 30%

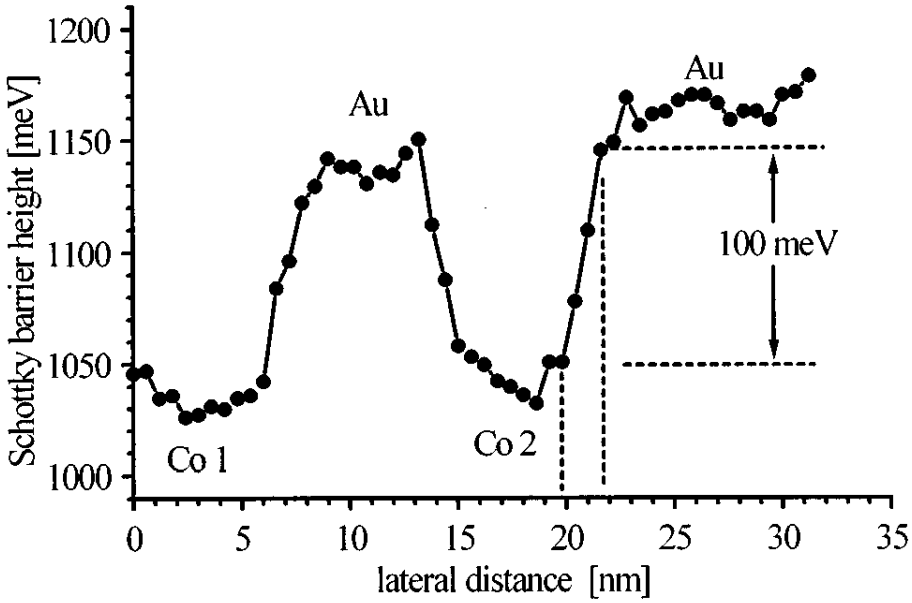

Figure 5.1: Schottky barrier height measurements using BEEM as a function of lateral distance x along the width of the junction, adapted from [121]. The clusters of Co deposited discontinously among the continuous Au layer are labeled Co1 and Co2. The presence of these clusters of width ~ 5 nm is shown to result in a sharp gradient in the barrier height, as well as a lowering of the barrier energy by 100 meV.

or greater can be imaged to identify the presence of Ge clusters and determine the impact of aggressive Ge doping on the homogeneity of the potential barrier. Further, samples doped with and without C impurities, commonly used in SiGe HBTs to prevent Boron out-diffusion, can be probed to determine the impact of C dopants on potential barrier. The doping profile as a function of lateral width can be carefully curated to identify a concentration of Ge with minimal clustering and reduction of potential barrier, should they be identified as the primary origin for barrier inhomogeneities. Finally, to concretely demonstrate the effects on noise performance, these tailor-made junction profiles characterized using BEEM may then be measured through CV and IV characteristics, followed by noise characterization measurements to determine potential improvements in cryogenic DC and RF performance.

Increasing the accuracy of noise measurement techniques

We have described the accuracy of the existing noise measurement system using the cold probe station (CPS), and the potential sources of uncertainty. Primarily, we have identified that variations in the reflection coefficient $|S_{11}|^2$

between -15 dB and -20 dB along the length of the input chain of the CPS noise setup can completely account for the observed uncertainty in the measurement noise temperature. The likely origin of these variations is the number of interconnections and cables used leading up to the DUT, as well as the inability to calibrate the noise power input to the DUT each time the pre-DUT components are assembled. However, no easy solutions exist to counteract these variations in the reflection coefficient. Measuring packaged structures of transistors with fewer input cables may result in a lower chance of reflection associated uncertainty, but the reducing the uncertainty of the noise source still requires the use of attenuation prior to the DUT. Further, the smart noise sources commonly used operate at ambient temperature and therefore require cables to translate the noise power to the cryogenic stage.

A noise source capable of operating at cryogenic temperatures, with rapid cycles between ON and OFF states and sufficient noise power may provide an alternative technique to measure noise of DUTs without multiple pre-DUT components. These noise sources would be operated at cryogenic temperatures and can be used adjacent to the DUT, thus eliminating the need for cables. A shot-noise tunnel junction (SNTJ) has been proposed in the literature as a cryogenic noise source that uses a packaged Si tunnel junction as a noise source upto 10 GHz has been demonstrated. [129] However, expanding and calibrating this noise source to operate at the frequencies of interest for shot-noise correlation measurements might prove to be challenging. Instead, if the mechanism used to generate noise power is thermal, the noise source can be operated across all frequencies and the accuracy of calibration would depend primarily on the knowledge of the physical temperature of the load.

A fast-switching, variable temperature load that can be used in waveguide system has been suggested in the literature. [130] The adaptation of this type of thermal load based noise source to a coaxial measurement system would provide a cryogenic noise source capable of operation to arbitrary frequencies, limited only by the choice of cables. The primary challenges associated with developing such a noise source involve careful design and selection of materials that enables switching speeds below $\sim$ 10 s, and thermal isolation of the noise source from the DUT. The packaged variable temperature noise source must also be small enough to enable cryostat measurements, and must be designed to minimize input return losses at the frequencies of interest. However, a noise

source packaged this way also presents the opportunity for integration with a variable impedance device like the long-line module (LLM). If developed for operation a high-frequencies, a packaged combination of a variable temperature noise source and an LLM can provide a cryogenic noise parameter extraction technique that would increase the likelihood of observing shot noise correlation effects.

With a more accurate method to measure noise temperatures and parameters at cryogenic temperatures, the physical mechanisms underlying shot noise correlation may be identified. The empirical noise transit time fitting parameter τ_n is currently assumed to be a fraction of the electron transit time, but this assumption has not been validated. An extraction of the noise transit time will provide greater insight into the physics of noisy signals in SiGe HBTs, and ultimately inform the strategy to minimize their noise performance at cryogenic temperatures.

BIBLIOGRAPHY

[1] John D Cressler and Guofu Niu. *Silicon-germanium heterojunction bipolar transistors*. Artech house, 2003.

[2] J. C. Bardin, S. Montazeri, and Su Wei Chang. "Silicon Germanium Cryogenic Low Noise Amplifiers". In: *Journal of Physics: Conference Series* 834.1 (2017). ISSN: 17426596. DOI: 10.1088/1742-6596/834/1/012007.

[3] Shirin Montazeri et al. "Ultra-Low-Power Cryogenic SiGe Low-Noise Amplifiers: Theory and Demonstration". In: *IEEE Transactions on Microwave Theory and Techniques* 64.1 (2016), pp. 178–187. ISSN: 00189480. DOI: 10.1109/TMTT.2015.2497685.

[4] H. Rucker, J. Korn, and J. Schmidt. "Operation of sige HBTs at cryogenic temperatures". In: *Proceedings of the IEEE Bipolar/BiCMOS Circuits and Technology Meeting* 2017-Octob (2017), pp. 17–20. ISSN: 10889299. DOI: 10.1109/BCTM.2017.8112902.

[5] Sander Weinreb, Joseph C. Bardin, and Hamdi Mani. "Design of Cryogenic SiGe Low-Noise Amplifiers". In: *IEEE Transactions on Microwave Theory and Techniques* 55.11 (2007), pp. 2306–2312. DOI: 10.1109/TMTT.2007.907729.

[6] David M Richey et al. "Evidence for non-equilibrium base transport in Si and SiGe bipolar transistors at cryogenic temperatures". In: *Solid-State Electronics* 39.6 (1996), pp. 785–789.

[7] D. Davidović et al. "Tunneling, current gain, and transconductance in silicon-germanium heterojunction bipolar transistors operating at millikelvin temperatures". In: *Physical Review Applied* 8.2 (2017), pp. 1–15. ISSN: 23317019. DOI: 10.1103/PhysRevApplied.8.024015.

[8] Hanbin Ying et al. "Collector Transport in SiGe HBTs Operating at Cryogenic Temperatures". In: *IEEE Transactions on Electron Devices* 65.9 (2018), pp. 3697–3703. ISSN: 00189383. DOI: 10.1109/TED.2018.2854288.

[9] Sander Weinreb et al. "Matched wideband low-noise amplifiers for radio astronomy". In: *Review of Scientific Instruments* 80.4 (2009). DOI: 10.1063/1.3103939.

[10] H Rücker and B Heinemann. "SiGe HBT technology". In: *Silicon-Germanium Heterojunction Bipolar Transistors for Mm-wave Systems Technology, Modeling and Circuit Applications*. River Publishers, 2022, pp. 11–54.

[11] Pascal Chevalier et al. "Si/SiGe:C and InP/GaAsSb Heterojunction Bipolar Transistors for THz Applications". In: *Proceedings of the IEEE* 105.6 (2017), pp. 1035–1050. ISSN: 00189219. DOI: 10.1109/JPROC.2017.2669087.

[12] Joseph Cheney Bardin. "Silicon-Germanium Heterojunction Bipolar Transistors For Extremely Low-Noise Applications Thesis by". In: *Changes* 2009 (2009).

[13] Damon Russell and Sander Weinreb. "Cryogenic Self-Calibrating Noise Parameter Measurement System". In: *IEEE Transactions on Microwave Theory and Techniques* 60.5 (2012), pp. 1456–1467. DOI: 10.1109/TMTT.2012.2188813.

[14] E. W. Bryerton, M. Morgan, and M. W. Pospieszalski. "Ultra low noise cryogenic amplifiers for radio astronomy". In: *2013 IEEE Radio and Wireless Symposium*. 2013, pp. 358–360. DOI: 10.1109/RWS.2013.6486740.

[15] Bishnu Patra et al. "Cryo-CMOS Circuits and Systems for Quantum Computing Applications". In: *IEEE Journal of Solid-State Circuits* 53.1 (2018), pp. 309–321. ISSN: 00189200. DOI: 10.1109/JSSC.2017.2737549.

[16] Anthony Joseph Ardizzi. "Self-Heating of HEMT Low-Noise Amplifiers in Liquid Cryogenic Environments and the Limits of Microwave Noise Performance". PhD thesis. California Institute of Technology, 2022.

[17] Alexander Youngsoo Choi. "Investigation of electronic fluctuations in semiconductor materials and devices through first-principles simulations and experiments in transistor amplifiers". PhD thesis. California Institute of Technology, 2022.

[18] Wei Ting Wong et al. "A 1 mW cryogenic LNA exploiting optimized SiGe HBTs to achieve an average noise temperature of 3.2 K from 4-8 GHz". In: *2020 IEEE/MTT-S International Microwave Symposium (IMS)*. IEEE. 2020, pp. 181–184. DOI: 10.1109/IMS30576.2020.9224049.

[19] Joel Schleeh. "Ultra-low noise InP HEMTs for cryogenic amplification". PhD thesis. Chalmers Tekniska Hogskola (Sweden), 2012.

[20] John D. Cressler. "Sige hbt technology: a new contender for si-based rf and microwave circuit applications". In: *IEEE Transactions on Microwave Theory and Techniques* 46.5 PART 2 (1998), pp. 572–589. ISSN: 00189480. DOI: 10.1109/22.668665.

[21] Chau-Ching Chiong et al. "Low-noise amplifier for next-generation radio astronomy telescopes: Review of the state-of-the-art cryogenic LNAs in the most challenging applications". In: *IEEE Microwave Magazine* 23.1 (2021), pp. 31–47.

[22] John Bardeen and Walter Hauser Brattain. "The transistor, a semiconductor triode". In: *Physical Review* 74.2 (1948), p. 230.

[23] William Shockley. "The Theory of p-n Junctions in Semiconductors and p-n Junction Transistors". In: *Bell system technical journal* 28.3 (1949), pp. 435–489.

[24] William Shockley, Morgan Sparks, and Gordon K Teal. "p- n Junction Transistors". In: *Physical Review* 83.1 (1951), p. 151.

[25] Aldert Van Der Ziel. "Theory of shot noise in junction diodes and junction transistors". In: *Proceedings of the IRE* 43.11 (1955), pp. 1639–1646.

[26] Morris Tanenbaum and DE Thomas. "Diffused emitter and base silicon transistors". In: *Bell System Technical Journal* 35.1 (1956), pp. 1–22.

[27] Tak H Ning. "History and future perspective of the modern silicon bipolar transistor". In: *IEEE Transactions on Electron Devices* 48.11 (2001), pp. 2485–2491.

[28] Tak H Ning and Randall D Isaac. "Effect of emitter contact on current gain of silicon bipolar devices". In: *IEEE Transactions on Electron Devices* 27.11 (1980), pp. 2051–2055.

[29] HN Ghosh et al. "Design and development of an ultralow-capacitance, high-performance pedestal transistor". In: *IBM Journal of Research and Development* 15.6 (1971), pp. 436–441.

[30] JW Slotboom and HC De Graaff. "Measurements of bandgap narrowing in Si bipolar transistors". In: *Solid-State Electronics* 19.10 (1976), pp. 857–862.

[31] Santosh P Gaur. "Performance limitations of silicon bipolar transistors". In: *IEEE Journal of Solid-State Circuits* 14.2 (1979), pp. 337–343.

[32] P Solomon and D Tang. "Bipolar circuit scaling". In: *1979 IEEE International Solid-State Circuits Conference. Digest of Technical Papers*. Vol. 22. IEEE. 1979, pp. 86–87.

[33] Herbert Kroemer. "Theory of a wide-gap emitter for transistors". In: *Proceedings of the IRE* 45.11 (1957), pp. 1535–1537.

[34] Gary L Patton et al. "Silicon-germanium base heterojunction bipolar transistors by molecular beam epitaxy". In: *IEEE Electron Device Letters* 9.4 (1988), pp. 165–167.

[35] Subramanian S Iyer et al. "Heterojunction bipolar transistors using Si-Ge alloys". In: *IEEE Transactions on Electron Devices* 36.10 (1989), pp. 2043–2064.

[36] John D Cressler et al. "On the low-temperature static and dynamic properties of high-performance silicon bipolar transistors". In: *IEEE transactions on electron devices* 36.8 (1989), pp. 1489–1502.

[37] John D Cressler et al. "On the profile design and optimization of epitaxial Si-and SiGe-base bipolar technology for 77 K applications. I. Transistor DC design considerations". In: *IEEE Transactions on Electron Devices* 40.3 (1993), pp. 525–541.

[38] Emmanuel F Crabbé et al. "Current gain rolloff in graded-base SiGe heterojunction bipolar transistors". In: *IEEE electron device letters* 14.4 (1993), pp. 193–195.

[39] DL Harame et al. "Optimization of SiGe HBT technology for high speed analog and mixed-signal applications". In: *Proceedings of IEEE International Electron Devices Meeting*. IEEE. 1993, pp. 71–74.

[40] John D Cressler et al. "An epitaxial emitter-cap SiGe-base bipolar technology optimized for liquid-nitrogen temperature operation". In: *IEEE Electron Device Letters* 15.11 (1994), pp. 472–474.

[41] John D Cressler et al. "Liquid-helium temperature operation of silicon-germanium heterojunction bipolar transistors". In: *Infrared Readout Electronics II*. Vol. 2226. SPIE. 1994, pp. 40–49.

[42] Peter Asbeck. "Heterojunction bipolar transistors: status and directions". In: *Proceedings of the Bipolar Circuits and Technology Meeting*. IEEE. 1989, pp. 65–69.

[43] DM Richey, JD Cressler, and RC Jaeger. "Numerical simulation of SiGe HBT's at cryogenic temperatures". In: *Le Journal de Physique IV* 4.C6 (1994), pp. C6–127.

[44] Jan W Slotboom et al. "Parasitic energy barriers in SiGe HBTs". In: *IEEE Electron device letters* 12.9 (1991), pp. 486–488.

[45] Alvin J Joseph, John D Cressler, and David M Richey. "Operation of SiGe heterojunction bipolar transistors in the liquid-helium temperature regime". In: *IEEE Electron Device Letters* 16.6 (1995), pp. 268–270.

[46] Stacey L. Salmon et al. "The influence of Ge grading on the bias and temperature characteristics of SiGe HBT's for precision analog circuits". In: *IEEE Transactions on Electron Devices* 47.2 (2000), pp. 292–298. ISSN: 00189383. DOI: 10.1109/16.822270.

[47] D.L. Harame et al. "Current status and future trends of SiGe BiCMOS technology". In: *IEEE Transactions on Electron Devices* 48.11 (2001), pp. 2575–2594. DOI: 10.1109/16.960385.

[48] Pascal Chevalier et al. "SiGe BiCMOS Current Status and Future Trends in Europe". In: *2018 IEEE BiCMOS and Compound Semiconductor Integrated Circuits and Technology Symposium, BCICTS 2018* (2018), pp. 64–71. DOI: 10.1109/BCICTS.2018.8550963.

[49] H. Rücker et al. "High-frequency SiGe:C HBTs with elevated extrinsic base regions". In: *Materials Science in Semiconductor Processing* 8.1 (2005). Proceedings of the Second International SiGe Technology and Device Meeting (ISTDM 2004) Kleist-Forum, Frankfurt (Oder), Germany, 16 - 19 May, 2004: From Materials and Process Technology to Device and, pp. 279–282. ISSN: 1369-8001. DOI: https://doi.org/10.1016/j.mssp.2004.09.061. URL: https://www.sciencedirect.com/science/article/pii/S1369800104001581.

[50] H. Rucker et al. "SiGe BiCMOS Technology with 3.0 ps Gate Delay". In: *2007 IEEE International Electron Devices Meeting*. 2007, pp. 651–654. DOI: 10.1109/IEDM.2007.4419028.

[51] Joseph C. Bardin and Sander Weinreb. "Experimental cryogenic modeling and noise of SiGe HBTs". In: *2008 IEEE MTT-S International Microwave Symposium Digest*. 2008, pp. 459–462. DOI: 10.1109/MWSYM.2008.4633202.

[52] Damon Russell and Sander Weinreb. "Low-Power Very Low-Noise Cryogenic SiGe IF Amplifiers for Terahertz Mixer Receivers". In: *IEEE Transactions on Microwave Theory and Techniques* 60.6 (2012), pp. 1641–1648. DOI: 10.1109/TMTT.2012.2190744.

[53] Jesus A Del Alamo, HL Tuller, and J Scholvin. *Integrated Microelectronic Devices*. Pearson, 2009.

[54] MV Fischetti, SE Laux, and W Lee. "Monte Carlo simulation of hot-carrier transport in real semiconductor devices". In: *Solid-state electronics* 32.12 (1989), pp. 1723–1729.

[55] Harold Grad. "Asymptotic theory of the Boltzmann equation". In: *The physics of Fluids* 6.2 (1963), pp. 147–181. DOI: https://doi.org/10.1063/1.1706716.

[56] Gang Chen. *Nanoscale energy transport and conversion: a parallel treatment of electrons, molecules, phonons, and photons*. Oxford university press, 2005.

[57] Chengyun Hua and Austin J. Minnich. "Semi-analytical solution to the frequency-dependent Boltzmann transport equation for cross-plane heat conduction in thin films". In: *Journal of Applied Physics* 117.17 (2015). ISSN: 10897550. DOI: 10.1063/1.4919432.

[58] J. Maassen and M. Lundstrom. "(Invited) The Landauer Approach to Electron and Phonon Transport". In: *ECS Transactions* 69.9 (2015), pp. 23–36. ISSN: 1938-6737. DOI: 10.1149/06909.0023ecst.

[59] J. Spanier and E.M. Gelbard. *Monte Carlo Principles and Neutron Transport Problems*. Addison-Wesley series in computer science and information processing. Addison-Wesley Publishing Company, 1969. ISBN: 9780598462183. URL: https://books.google.com/books?id=Gcd-AAAAIAAJ.

[60] Mark A. Stettler and Mark S. Lundstrom. "A Microscopic Study of Transport in Thin Base Silicon Bipolar Transistors". In: *IEEE Transactions on Electron Devices* 41.6 (1994), pp. 1027–1033. ISSN: 15579646. DOI: 10.1109/16.293317.

[61] Shin Ichi Tanaka and M.S. Lundstrom. "A compact HBT device model based on a one-flux treatment of carrier transport". In: *Solid-state electronics* 37.3 (1994), pp. 401–410. DOI: https://doi.org/10.1016/0038-1101(94)90004-3.

[62] Mark Lundstrom. "Carrier Transport in BJTs: From Ballistic to Diffusive and Off-Equilibrium". In: *2018 IEEE BiCMOS and Compound Semiconductor Integrated Circuits and Technology Symposium, BCICTS 2018* (2018), pp. 174–181. DOI: 10.1109/BCICTS.2018.8551154.

[63] Anatoly A Grinberg and Serge Luryi. "Diffusion in a short base". In: *Solid-state electronics* 35.9 (1992), pp. 1299–1309. DOI: https://doi.org/10.1016/0038-1101(92)90165-9.

[64] Jean Philippe M. Péraud and Nicolas G. Hadjiconstantinou. "Extending the range of validity of Fourier's law into the kinetic transport regime via asymptotic solution of the phonon Boltzmann transport equation". In: *Physical Review B* 93.4 (2016). ISSN: 24699969. DOI: 10.1103/PhysRevB.93.045424.

[65] A. S. Bhuiyan, A. Martinez, and D. Esteve. "A new Richardson plot for non-ideal schottky diodes". In: *Thin Solid Films* 161.C (July 1988), pp. 93–100. ISSN: 0040-6090. DOI: 10.1016/0040-6090(88)90239-8.

[66] Reuben Hackam and Peter Harrop. "Electrical Properties of Nickel-Low-Doped n-Type Gallium Arsenide Schottky-Barrier Diodes". In: *IEEE Transactions on Electron Devices* 19.12 (1972), pp. 1231–1238. ISSN: 15579646. DOI: 10.1109/T-ED.1972.17586.

[67] R. T. Tung. "Electron transport at metal-semiconductor interfaces: General theory". In: *Physical Review B* 45.23 (1992), pp. 13509–13523. ISSN: 01631829. DOI: 10.1103/PhysRevB.45.13509.

[68] J. P. Sullivan et al. "Electron transport of inhomogeneous Schottky barriers: A numerical study". In: *Journal of Applied Physics* 58.24 (Aug. 1991), p. 7403. ISSN: 00036951. DOI: 10.1063/1.104747. URL: https://aip.scitation.org/doi/abs/10.1063/1.349737.

[69] Winfried Mönch. "Semiconductor Interfaces". In: Springer, Berlin, Heidelberg, 2001, pp. 385–481. DOI: 10.1007/978-3-662-04459-9_19. URL: https://link.springer.com/chapter/10.1007/978-3-662-04459-9%7B%5C_%7D19.

[70] Mario Prietsch. "Ballistic-electron emission microscopy (BEEM): Studies of metal/semiconductor interfaces with nanometer resolution". In: *Physics Reports* 253.4 (1995), pp. 163–233. DOI: 10.1016/0370-1573(94)00082-E.

[71] Gary L. Patton et al. "Silicon-Germanium-Base Heterojunction Bipolar Transistors By Molecular Beam Epitaxy". In: *IEEE Electron Device Letters* 9.4 (1988), pp. 165–167. ISSN: 15580563. DOI: 10.1109/55.677.

[72] A Gruhle et al. "MBE-grown Si/SiGe HBTs with high beta, f_T, and f_{max} ". In: *IEEE electron device letters* 13.4 (1992), pp. 206–208. DOI: 10.1109/55.145022.

[73] Gary L Patton et al. "SiGe-Base Heterojunction Bipolar Transistors". In: *International Technical Digest on Electron Devices* 1.4 (1990), pp. 171–173. DOI: 10.1109/IEDM.1990.237237.

[74] S. E. Swirhun, D. E. Kane, and R. M. Swanson. "Temperature dependence of minority electron mobility and bandgap narrowing in p+ Si". In: *Technical Digest - International Electron Devices Meeting* (Dec. 1988), pp. 298–301. ISSN: 01631918. DOI: 10.1109/iedm.1988.32816.

[75] D. B. M. Klaassen. "A unified mobility model for device simulation—II. Temperature dependence of carrier mobility and lifetime". In: *Solid State Electronics* 35.7 (1992), pp. 961–967. DOI: https://doi.org/10.1016/0038-1101(92)90326-8.

[76] Jae Sung Rieh. "Temperature dependent minority electron mobilities in strained Si/sub 1-x/Ge/sub x/ (0. 2 < x < 0. 4) layers". In: *IEEE Transactions on Electron Devices* 47.4 (2000), pp. 883–890. ISSN: 00189383. DOI: 10.1109/16.831009.

[77] Mark Lundstrom. *Fundamentals of Carrier Transport*. 2000. DOI: 10.1017/cbo9780511618611.

[78] Subrahmanyan Chandrasekhar. Dover Publ.(New York, NY), 1960.

[79] Michael F Modest. *Radiative heat transfer*. Academic press, 2013.

[80] Melih Özaydin and Lester F Eastman. "Non-equilibrium carrier transport in the base of heterojunction bipolar transistors". In: *Solid-State Electronics* 39.5 (1996), pp. 731–735. DOI: https://doi.org/10.1016/0038-1101(95)00159-X.

[81] Carlo Cercignani and Adelia Daneri. "Flow of a rarefied gas between two parallel plates". In: *Journal of Applied Physics* 34.12 (1963), pp. 3509–3513. DOI: https://doi.org/10.1063/1.1729249.

[82] Carlo Cercignani. *Rarefied gas dynamics: from basic concepts to actual calculations*. Vol. 21. Cambridge University Press, 2000.

[83] Avshalom Manela and Nicolas G. Hadjiconstantinou. "Gas motion induced by unsteady boundary heating in a small-scale slab". In: *Physics of Fluids* 20.11 (2008). ISSN: 10706631. DOI: 10.1063/1.3010759.

[84] Yoshio Sone. "Asymptotic theory of flow of rarefied gas over a smooth boundary I". In: *Rarefied Gas Dynamics* (1969), pp. 243–253.

[85] Jesse Maassen and Mark Lundstrom. "Steady-state heat transport: Ballistic-to-diffusive with Fourier's law". In: *Journal of Applied Physics* 117.3 (2015). ISSN: 10897550. DOI: 10.1063/1.4905590. arXiv: 1408.1631. URL: http://dx.doi.org/10.1063/1.4905590.

[86] *NSM Archives, Si - Silicon*. [Online; accessed 29-April-2021]. URL: http://www.ioffe.ru/SVA/NSM/Semicond/Si/bandstr.html.

[87] Alexander Y Choi et al. "Electronic noise of warm electrons in semiconductors from first principles". In: *Physical Review Materials* 5.4 (2021), p. 044603. DOI: https://doi.org/10.1103/PhysRevMaterials.5.044603.

[88] Michael Schröter et al. "Physical and electrical performance limits of high-speed SiGeC HBTs- Part I: Vertical scaling". In: *IEEE Transactions on Electron Devices* 58.11 (2011), pp. 3687–3696. ISSN: 00189383. DOI: 10.1109/TED.2011.2163722.

[89] Vibhor Jain and Mark J. W. Rodwell. "Transconductance Degradation in Near-THz InP Double-Heterojunction Bipolar Transistors". In: *IEEE Electron Device Letters* 32.8 (2011), pp. 1068–1070. DOI: 10.1109/LED.2011.2157451.

[90] D. J. Ewing et al. "Inhomogeneous electrical characteristics in 4H-SiC Schottky diodes". In: *Semiconductor Science and Technology* 22.12 (2007), pp. 1287–1291. ISSN: 02681242. DOI: 10.1088/0268-1242/22/12/008.

[91] Leo Esaki, Yuriko Miyahara, and Sony Corporation. "A new device using the tunneling process in narrow p-n junctions". In: *Solid State Electronics* 1 (1960), pp. 13–21. ISSN: 00381101. DOI: 10.1016/0038-1101(60)90052-6.

[92] D. J. Dumin and G. L. Pearson. "Properties of gallium arsenide diodes between 4.2°and 300°K". In: *Journal of Applied Physics* 36.11 (July 1965), pp. 3418–3426. ISSN: 00218979. DOI: 10.1063/1.1703009. URL: https://doi.org/10.1063/1.1703009.

[93] Jesus A. Del Alamo and Richard M. Swanson. "Forward-bias tunneling: a limitation to bipolar device scaling". In: *Electron device letters* EDL-7.11 (1986), pp. 629–631. ISSN: 01938576. DOI: 10.1109/edl.1986.26499.

[94] FA Padovani and GG Sumner. "Experimental study of gold-gallium arsenide Schottky barriers". In: *Journal of Applied Physics* 36.12 (1965), pp. 3744–3747. DOI: https://doi.org/10.1063/1.1713940.

[95] F.A. Padovani and R. Stratton. "Field and thermionic-field emission in Schottky barriers". In: *Solid-State Electronics* 9.7 (1966), pp. 695–707. ISSN: 0038-1101. DOI: https://doi.org/10.1016/0038-1101(66)90097-9. URL: https://www.sciencedirect.com/science/article/pii/0038110166900979.

[96] R. T. Tung. "Schottky-Barrier Formation at Single-Crystal Metal-Semiconductor Interfaces". In: *Phys. Rev. Lett.* 52 (6 Feb. 1984), pp. 461–464. DOI: 10.1103/PhysRevLett.52.461. URL: https://link.aps.org/doi/10.1103/PhysRevLett.52.461.

[97] R. T. Tung et al. "Schottky-barrier inhomogeneity at epitaxial $NiSi_2$ interfaces on Si(100)". In: *Phys. Rev. Lett.* 66 (1 Jan. 1991), pp. 72–75. DOI: 10.1103/PhysRevLett.66.72. URL: https://link.aps.org/doi/10.1103/PhysRevLett.66.72.

[98] Martin von Haartman et al. "Random telegraph signal noise in SiGe heterojunction bipolar transistors". In: *Journal of applied physics* 92.8 (2002), pp. 4414–4421. DOI: https://doi.org/10.1063/1.1506197.

[99] J. Raoult et al. "Impact of carbon concentration on 1f noise and random telegraph signal noise in SiGe:C heterojunction bipolar transistors". In: *Journal of Applied Physics* 103.11 (2008). ISSN: 00218979. DOI: 10.1063/1.2939252.

[100] John D Cressler. "New Developments in SiGe HBT Reliability for RF Through mmW Circuits". In: *2021 IEEE International Reliability Physics Symposium (IRPS)*. IEEE. 2021, pp. 1–6. DOI: 10.1109/IRPS46558.2021.9405171.

[101] Xiaodi Jin et al. "Advanced SiGe:C HBTs at Cryogenic Temperatures and Their Compact Modeling with Temperature Scaling". In: *IEEE Journal on Exploratory Solid-State Computational Devices and Circuits* 7.2 (2021), pp. 175–183. ISSN: 23299231. DOI: 10.1109/JXCDC.2021.3130041.

[102] F. A. Padovani and G. G. Sumner. "Experimental study of gold-gallium arsenide schottky barriers". In: *Journal of applied physics* 36.12 (Dec. 1965), pp. 3744–3747. ISSN: 0021-8979. DOI: 10.1063/1.1713940. URL: http://aip.scitation.org/doi/10.1063/1.1713940 (visited on 09/01/2023).

[103] A.N. Saxena. "Forward current-voltage characteristics of Schottky barriers on n-type silicon". In: *Surface science* 13.1 (Jan. 1969), pp. 151–171. ISSN: 00396028. DOI: 10.1016/0039-6028(69)90245-3. URL: https://linkinghub.elsevier.com/retrieve/pii/0039602869902453 (visited on 09/08/2023).

[104] S. Ashok, J.M. Borrego, and R.J. Gutmann. "Electrical characteristics of GaAs MIS Schottky diodes". In: *Solid-state electronics* 22.7 (July 1979), pp. 621–631. ISSN: 00381101. DOI: 10.1016/0038-1101(79)90135-7. URL: https://linkinghub.elsevier.com/retrieve/pii/0038110179901357 (visited on 09/20/2023).

[105] Jürgen H. Werner and Herbert H. Güttler. "Barrier inhomogeneities at Schottky contacts". In: *Journal of Applied Physics* 69.3 (Feb. 1991), pp. 1522–1533. ISSN: 0021-8979. DOI: 10.1063/1.347243. eprint: https://pubs.aip.org/aip/jap/article-pdf/69/3/1522/8018481/1522_1_online.pdf. URL: https://doi.org/10.1063/1.347243.

[106] J. L. Freeouf et al. "Effective barrier heights of mixed phase contacts: Size effects". In: *Applied physics letters* 40.7 (Apr. 1982), pp. 634–636. ISSN: 0003-6951. DOI: 10.1063/1.93171. URL: https://pubs.aip.org/apl/article/40/7/634/47889/Effective-barrier-heights-of-mixed-phase-contacts (visited on 09/07/2023).

[107] Y.P. Song et al. "On the difference in apparent barrier height as obtained from capacitance-voltage and current-voltage-temperature measurements on Al/p-InP Schottky barriers". In: *Solid-state electronics* 29.6 (June 1986), pp. 633–638. ISSN: 00381101. DOI: 10.1016/0038-1101(86)90145-0. URL: https://linkinghub.elsevier.com/retrieve/pii/0038110186901450 (visited on 09/27/2023).

[108] R. T. Tung. "Schottky-Barrier Formation at Single-Crystal Metal-Semiconductor Interfaces". In: *Physical Review Letters* 52.6 (Feb. 1984), pp. 461–464. ISSN: 0031-9007. DOI: 10.1103/{PhysRevLett}.52.461. URL: https://link.aps.org/doi/10.1103/%7BPhysRevLett%7D.52.461 (visited on 06/24/2021).

[109] R. J. Hauenstein et al. "Schottky barrier height measurements of epitaxial NiSi2 on Si". In: *Applied physics letters* 47.8 (Oct. 1985), pp. 853–855. ISSN: 0003-6951. DOI: 10.1063/1.96007. URL: https://pubs.aip.org/apl/article/47/8/853/51219/Schottky-barrier-height-measurements-of-epitaxial (visited on 09/08/2023).

[110] RT Tung et al. "Schottky-barrier inhomogeneity at epitaxial NiSi2 interfaces on Si(100)." In: *Physical Review Letters* 66.1 (Jan. 1991), pp. 72–75. DOI: 10.1103/{PhysRevLett}.66.72. URL: http://dx.doi.org/10.1103/%7BPhysRevLett%7D.66.72 (visited on 09/11/2023).

[111] Hans von Känel, Thomas Meyer, and Michaela Klemenc. "Ballistic-Electron-Emission Microscopy on Epitaxial Silicides". In: *Japanese journal of applied physics* 37.6S (June 1998), p. 3800. ISSN: 0021-4922. DOI: 10.1143/{JJAP}.37.3800. URL: https://iopscience.iop.org/article/10.1143/%7BJJAP%7D.37.3800 (visited on 09/07/2023).

[112] H. von Känel and T. Meyer. "Spectroscopy on MBE-grown interfaces with high spatial resolution". In: *Thin solid films* 306.2 (Sept. 1997), pp. 214–219. ISSN: 00406090. DOI: 10.1016/S0040-6090(97)00184-3. URL: https://linkinghub.elsevier.com/retrieve/pii/S0040609097001843 (visited on 09/08/2023).

[113] WJ Kaiser and LD Bell. "Direct investigation of subsurface interface electronic structure by ballistic-electron-emission microscopy." In: *Physical Review Letters* 60.14 (Apr. 1988), pp. 1406–1409. DOI: 10.1103/{PhysRevLett}.60.1406. URL: http://dx.doi.org/10.1103/%7BPhysRevLett%7D.60.1406 (visited on 09/07/2023).

[114] Simon M Sze, Yiming Li, and Kwok K Ng. *Physics of Semiconductor Devices*. John wiley & sons, 2021.

[115] I. Ohdomari, T. S. Kuan, and K. N. Tu. "Microstructure and Schottky barrier height of iridium silicides formed on silicon". In: *Journal of applied physics* 50.11 (Nov. 1979), pp. 7020–7029. ISSN: 0021-8979. DOI: 10.1063/1.325860. URL: https://pubs.aip.org/jap/article/50/11/7020/291392/Microstructure-and-Schottky-barrier-height-of (visited on 09/26/2023).

[116] Bekari Gabritchidze et al. "Experimental Characterization of Temperature-Dependent Microwave Noise of Discrete HEMTs: Drain Noise and Real-Space Transfer". In: *2022 IEEE/MTT-S International Microwave Symposium - IMS 2022*. 2022, pp. 615–618. DOI: 10.1109/IMS37962.2022.9865505.

[117] Pauli Virtanen et al. "SciPy 1.0: Fundamental Algorithms for Scientific Computing in Python". In: *Nature Methods* 17 (2020), pp. 261–272. DOI: 10.1038/s41592-019-0686-2.

[118] H. Rücker and B. Heinemann. "SiGe HBT Technology". In: *Silicon-Germanium Heterojunction Bipolar Transistors for Mm-wave Systems Technology, Modeling and Circuit Applications*. 1st ed. River Publishers, 2018, pp. 11–54. ISBN: 978-1-00-333951-9. URL: https://doi.org/10.1201/9781003339519-2.

[119] Arnout Beckers, Farzan Jazaeri, and Christian Enz. "Theoretical limit of low temperature subthreshold swing in field-effect transistors". In: *IEEE Electron Device Letters* 41.2 (2019), pp. 276–279.

[120] H Sirringhaus et al. "Spatial variations of hot-carrier transmission across CoSi 2/Si interfaces on a nanometer scale". In: *Physical Review B* 53.23 (1996), p. 15944.

[121] Alexander Olbrich et al. "The origin of the integral barrier height in inhomogeneous Au/Co/GaAs 67 P 33-Schottky contacts: a ballistic electron emission microscopy study". In: *Journal of applied physics* 83.1 (1998), pp. 358–365.

[122] R. A. Kiehl et al. "Electrical and physical properties of high-Ge-content Si/SiGe p-type quantum wells". In: *Physical Review B* 48.16 (Oct. 1993), pp. 11946–11959. ISSN: 01631829. DOI: 10.1103/PhysRevB.48.11946. URL: https://journals.aps.org/prb/abstract/10.1103/PhysRevB.48.11946.

[123] Damon Stuart Russell. "Technology advances for radio astronomy". PhD thesis. California Institute of Technology, 2013.

[124] Hans Hartnagel, Ramunas Katilius, and Arvydas Matulionis. *Microwave noise in semiconductor devices*. John Wiley & Sons, 2001.

[125] G. Niu et al. "A unified approach to RF and microwave noise parameter modeling in bipolar transistors". In: *IEEE Transactions on Electron Devices* 48.11 (2001), pp. 2568–2574. ISSN: 00189383. DOI: 10.1109/16.960384.

[126] P. Sakalas et al. "Compact Modeling of High Frequency Correlated Noise in HBTs". In: *2006 Bipolar/BiCMOS Circuits and Technology Meeting*. 2006, pp. 1–4. DOI: 10.1109/BIPOL.2006.311175.

[127] Bekari Gabritchidze. "Investigation of drain noise in high electron mobility transistors through on-wafer characterization and modelling". en. PhD thesis. Crete, Greece: Department of Physics, University of Crete, 2022. (Visited on 08/08/2023).

[128] Keysight Technologies. *SNS Series Noise Sources - Technical Overview*. URL: https://www.keysight.com/us/en/product/N4002A/sns-series-noise-source-10-mhz-26-5-ghz-enr-15-db.html.

[129] Su-Wei Chang et al. "Noise measurement of cryogenic low noise amplifiers using a tunnel-junction shot-noise source". In: *2016 IEEE MTT-S International Microwave Symposium (IMS)*. IEEE. 2016, pp. 1–4.

[130] Jacob W. Kooi et al. "A Programmable Cryogenic Waveguide Calibration Load With Exceptional Temporal Response and Linearity". In: *IEEE Transactions on Terahertz Science and Technology* 8.4 (2018), pp. 434–445. DOI: 10.1109/TTHZ.2018.2826838.

INDEX